Development of Multi-Purpose Lipid Coated PNIPAM Microgels and Techniques for Characterizing Lateral Diffusion in Bilayers

by

Qasim Saleem

A thesis submitted in conformity with the requirements
for the degree of Doctor of Philosophy

Department of Chemistry
University of Toronto

Development of Multi-Purpose Lipid Coated PNIPAM Microgels and Techniques for Characterizing Lateral Diffusion in Bilayers

Qasim Saleem

Doctor of Philosophy

Department of Chemistry
University of Toronto

2014

Abstract

The pursuit of a greater understanding of the biological membrane has led to the development of a number of mimetics and probing techniques. This thesis contributes to both of these efforts.

Towards the development of mimetics, poly(N-isopropylacrylamide) (pNIPAM) microgels were explored as membrane supports. PNIPAM microgels are “smart” materials that experience a volume phase transition (VPT) at ~32°C, where they undergo a severe loss in volume. The core-shell microgels were synthesized with a low crosslinked pNIPAM core covered by a highly crosslinked pNIPAM shell that was functionalized with exploitable carboxylates.

It was shown that a lipid bilayer could be coated on these microgels using either liposomes or bicelles. Specifically, lipid bilayer enclosed microgels made with liposomes (“Lipogels”) were created by using hydrophobically modified microgels, which possessed the ability to sequester liposomes that could ultimately be fused into a continuous bilayer. It was also found that above the VPT temperature, surface decoupled lipid protrude into highly curved structures. Hence, the VPT property could be used to control the curvature of the Lipogel

bilayer. These particles could be useful platforms for conducting biophysical membrane studies as well as drug delivery vehicles.

Bicelles were also explored as lipid sources for microgel coating, resulting in the creation of “Bicellogels”. Electrostatic attraction between cationic bicelles and unmodified anionic core-shell pNIPAM microgels resulted in the coating of the latter. Astonishingly, the resulting bilayer was made up of only the long chain bicellar lipid. Due to the simplicity of this method, it could be extended to easily coat all types of soft material.

The last development on the pNIPAM front involved the coupling of intact liposomes to microgels to create “VESCOgels”. These complexes offer two distinct cargo holds through which temporally distinct release can be achieved. Hence, they could be very useful for applications in tandem release.

Lastly, the ^{31}P CODEX NMR technique was adapted to study the lateral diffusion of phospholipids in large liposomes. This technique allows for the measurement of lateral diffusion coefficients of multiple phospholipids simultaneously. This could prove useful for the study of such biologically relevant phenomena as domain formations and drug-lipid interactions.

Acknowledgments

“Whoever does not give thanks to the people, does not give thanks to God”.
- Muhammad (صلي الله عليه وسلم)

الحمد لله والصلاة والسلام على رسول الله

To thank or acknowledge everyone who helped me along my graduate journey would require a chapter on its own. So, I would like to apologize to anyone whose mention I had to grudgingly forgo. Even if you are not on the page, you are surely in my heart.

Firstly, I would like to thank my supervisor, Dr. Peter M. Macdonald, for his intellectual support and unwavering commitment to seeing me succeed at my work. Even with heavy obligations as the Chair of the department during my studies, he made the time to guide and advise me, and write letter of recommendations whenever I asked. It’s been a great experience working with you, Sir!

I would also like to thank my committee members, Dr. David McMillen and Dr. Scott Prosser for their input during my committee meetings and for reading my thesis on very short notice. I would also like to thank Dr. Voula Kanelis and Dr. Claudiu Gradinaru for attending my comprehensive exam and defence, respectively. Lastly, I would like to thank Dr. Linda Reven for agreeing to be the external examiner at my defence, and giving me such nice and kind comments on my thesis.

I had a great time collaborating with members of the Gradinaru group. Specifically, I’d like to thank Dr. Baoxu Liu and Zhenfu Zhang, who would operate their highly complex fluorescence microscopes while I stood near the monitors anxiously waiting for the results to appear on the screen. Dr. Liu must also be acknowledged for developing the Monte Carlo simulation that enabled us to extract the diffusion coefficients from our bilayered systems. 谢谢您的帮助，宝旭和振富！

I had three mentors during my time at the lab that I must acknowledge. Firstly, I’d like to thank Dr. Neil MacKinnon for the guidance, support and expertise he provided during my formative “undergrad to grad” transition years. I would have been lost without the practical and intellectual training he provided. Vielen Dank, Neil! My gratitude also extends to Dr. Ronald Soong who has been and continues to be an ocean of good advice. 谢谢你，嘉基！

Lastly, I'd like to thank Dr. Kazuomi Nagashima for helping me explore advanced concepts in NMR spectroscopy and bequeathing some of his amazing polymer/NMR books to the lab. カズ、どうもありがとうございます！

I have had a great time working with all my graduate colleagues over the years, namely Induja Mahanthantila, Christiano (Rohan) Daniel Augustine Alvares, Hannah Hazel A. Morales and Angel Lai. I couldn't have wished for a more helpful, considerate, drama-free, and knowledgeable group of people to work with. I really benefited from all you in one way or another. Special mention must be made of Hannah and Angel for running the PFG diffusion and some of the CODEX experiments, respectively, which are discussed in Chapter 5. धन्यवाद, obrigado, salamat, 谢谢! I was also privileged to work with a number of undergraduates, and extend my thanks to Christian Sawicki, Hawraa Kamar, Qasim Muhammad, Yuvraj Pannu and Amy Petretic. I would especially like to thank Amy for preparing samples for the work described in Chapter 3. Dziękuję, شکریا, شـــکریا, ਥਾਨਕ ਯੋਊ, hvala!

The research in this thesis would not have been possible without access to instruments and expertise available at the Krull, McMillen and Heerklotz groups. I would also like to thank Dr. Peter Mitrakos for maintaining the NMR spectrometers and the instruments at the CABB facility.

Finally, this thesis could not have been written without the absolute loving support of my dear family. My ابو جی and ماماجی are probably the kindest, smartest and selfless people I know, who, I can imagine, could have accomplished the work in my thesis in less than half the time that it took me. They are truly the best parents anyone can ask for. کے لئے صدقہ جار یا بنانے اللہ آپ دونوں کو طویل زندگی دے اور مجھے آپ دونوں. My اپـا has been a sweetheart of an older sister, who has supported me even when she moved away to another continent. You and my cute, little niece have always been in my thoughts. Finally, I have to thank and acknowledge my amazing baby sis who has been a best friend, a worthy interlocutor and occupies a special place in my heart. You have always been in my prayers and will, God Willing, do amazing in your own academic journey. I dedicate my thesis to you all!

Table of Contents

List of Tables

List of Figures

List of Symbols

Δ_{red}	Reduced chemical shift anisotropy
Δ	Chemical shift anisotropy
β	Angle between phospholipid long molecular axis and the principle magnetic field
γ	Magnetogyric ratio
η	Asymmetry factor
$\eta_{sol}, \eta_{LUV}, \eta_o$	Viscosity of solution, LUV sample and water, respectively
$\hat{I}$	Spin angular momentum operator
T_2^{RC}	Relaxation due to rf errors
f^{int}	Signal decays due to intermediate time scale motions during recoupling cycles
f_m	Fraction of mobile sites
f^{slow}	Signal decays due to slow motions during the mixing time
$k_B T$	Boltzmann temperature
θ, ϕ	Polar angles defining orientation of B_0 in the principal axis frame
θ_j	Flip angle about the axis *j*
σ	Shielding tensor
σ^{PAF}	Principal axis frame value
σ_{iso}	Isotropic chemical shift value
τ_n	Fluorescence recovery after photobleaching time constant (n is a number)
τ_x	Correlation time for the molecular motion corresponding to x
υ	Chemical shift frequency in Hz
υ_r	MAS frequency
ω_0	Larmor frequency
ω	Chemical shift frequency in radians
μ	Magnetic moment
A	Diffusing population fraction
a_o	Size of the phospholipid headgroup
b	Non-zero equilibrium intensity at long mixing times
B_0	External magnetic field

B_1	Oscillating radio frequency field
D	Diffusion coefficient
E	Energy level
$\hbar$	Planck constant
I	Fluorescence intensity
l_c	Length of phospholipid acyl chains
M	Ensemble net magnetization
m+1	Number of 180° pulses applied during the recoupling period
M_M	Number of equivalent orientational sites
n	Number of recoupling cycles
N	Number of rotor periods
n_r	Non-radiative decay rate
p	Critical packing parameter
q	Molar ratio of long-chain and short-chain lipid concentrations
Q	Quantum yield
r	Radius of vesicles
S	CODEX peak intensity
SE_n	Singlet excited state
T_1	Spin-lattice relaxation time
T_2	Spin-spin relaxation time
T_M	Phospholipid chain melting temperature
t_m, t_r	Mixing time, rotor period
v	Volume of phospholipid acyl chains
Γ	Emissive rate of the fluorophore
$P(r)$	Probability density for a particular vesicle radius

List of Abbreviations

AA	Acrylic acid
AECHO	3-O (2-aminoethoxyethyloxyethyl)carbamyl cholesterol
CF	Carboxyfluorescein
CHOL	Cholesterol
CMC	Critical micellar concentration
CODEX	Centre-band only detection of exchange
CSA	Chemical shift anisotropy
DHPC	1,2-dihexanoyl-*sn*-glycero-3-phosphocholine
DIPEA	N,N'-diisopropylethylamine
DLS	Dynamic light scattering
DMPC	1,2-dimyristoyl-*sn*-glycero-3-phosphocholine
DMTAP	1,2-dimyristoyl-3-trimethylammonium-propane
EDAC	1-ethyl-3-(3-dimethylaminopropyl)carbodiimide
EDTA	Ethylenediaminetetraacetic acid
EGTA	Ethylene glycol tetraacetic acid
EIS	Exchange induced sidebands
ESI-MS	Electrospray ionization mass spectrometry
EXSY	Exchange spectroscopy
FA	Fluorescein *O*-acrylate
FCS	Fluorescence correlation spectroscopy
FRAP	Fluorescence recovery after photobleaching
FS	Sodium fluorescein
FWHH	Full width at half-height
GUV	Giant unilamellar vesicle
HM	Hydrophobically modified
KPS	Potassium persulfate
LB	Langmuir-Blodgett
LCST	Lower critical solution temperature

LMV	Large multilamellar vesicle
LUV	Large unilamellar vesicle
MAS	Magic angle spinning
MBA	Methylene bis(acrylamide)
NBD	7-nitro-2-1,3-benzoxadiazol-4-yl
NBD-PE	1,2-dioleoyl-*sn*-glycero-3-phosphoethanolamine-N-(7-nitro-2–1,3-benzoxadiazol-4-yl) (ammonium salt)
NHS	N-hydroxysuccinimide
ODESSA	1D exchange spectroscopy by sideband alternation
pNIPAM	Poly(N-isopropylacrylamide)
PA	Phosphatidic acid
PAF	Principal axis frame
PC	Phosphatidylcholine
PCS	Photon correlation spectroscopy
PDI	Polydispersity index
PE	Phosphatidylethanolamine
PEG	Poly(ethylene glycol)
PFG	Pulsed field gradients
PG	Phosphatidylglycerol
PI	Phosphatidylinositol
POPC	1-palmitoyl-2-oleoyl-*sn*-glycero-3-phosphocholine
POPG	1-palmitoyl-2-oleoyl-*sn*-glycero-3-phosphoglycerol
PS	Phosphatidylserine
R6G	Rhodamine 6G
rf	Radio-frequency
RhB-PE	Lissamine rhodamine B 1,2-dihexadecanoyl-*sn*-glycero-3-phosphoethanolamine (triethylammonium salt)
SPB	Supported phospholipid bilayer
SPT	Single particle tracking
SSB	Spinning sidebands

ssNMR	Solid state nuclear magnetic resonance
STE	Stimulated echo
SUV	Small unilamellar vesicle
TCTU	N,N,N’,N’-tetramethyluronium tetrafluoroborate
Triton	Triton X-100
VPT	Volume phase transition

Introduction

Biological membranes are made of lipid bilayers which support a host of macromolecules within their milieu. They are approximately 50 Å thick, and consist of a hydrophobic layer separating two hydrophilic regions on either side which are in direct contact with the cellular interior and exterior. This morphology allows the membrane to function as a barrier to certain ions, effectively allowing the cell to maintain a distinct inner environment. To render the membrane capable of complex functions, a variety of proteins, sterols and carbohydrates occupy a considerable volume of the bilayer. These macromolecules are often asymmetrically distributed in the leaflets but are usually allowed to diffuse laterally along the membrane due to the fluid nature of the lipid bilayers. All of this enables the membranes to participate in important functions such as molecular cargo transport, signal transduction, and motility. Due to the simultaneous occurrence of diverse phenomena taking place in the cell membrane, studying specific properties in isolation is often difficult with even the most sophisticated of techniques. Hence, ideal artificial model membrane systems are often used that mimic the essential features of the cell membrane that are of interest to the experimenter.

As an introduction to the contents of this thesis, essential aspects of lipids will be reviewed and the model membrane mimetics used in the thesis will be discussed. Within this section, supported bilayers will receive special attention, with specific mention of the strategies used to fabricate them. Furthermore, basic theory of fluorescence and solid state nuclear magnetic resonance (ssNMR) will also be presented to provide background for the characterization techniques used in this thesis.

1.1 Basics of Lipids

A lipid is an amphipathic molecule, consisting of both a hydrophilic and hydrophobic region within its structure. Membranes are mostly lipids by number, consisting of phospholipids, sphingolipids, sterols and fatty acids. Phospholipids constitute the majority and structurally consist of a hydrophilic phosphate bearing headgroup bonded to a hydrophobic diglyceride. The headgroup could be zwitterionic or charged depending on the moiety connected to the phosphate group. The diglyceride is composed of two fatty acid chains linked to a glycerol via an ester bond. The fatty acids could be saturated (i.e. have no double bonds) or unsaturated (i.e. possessing double bonds) and can vary in carbon chain length. A list of phospholipid lipid headgroups and chains are illustrated in Figure 1-1.

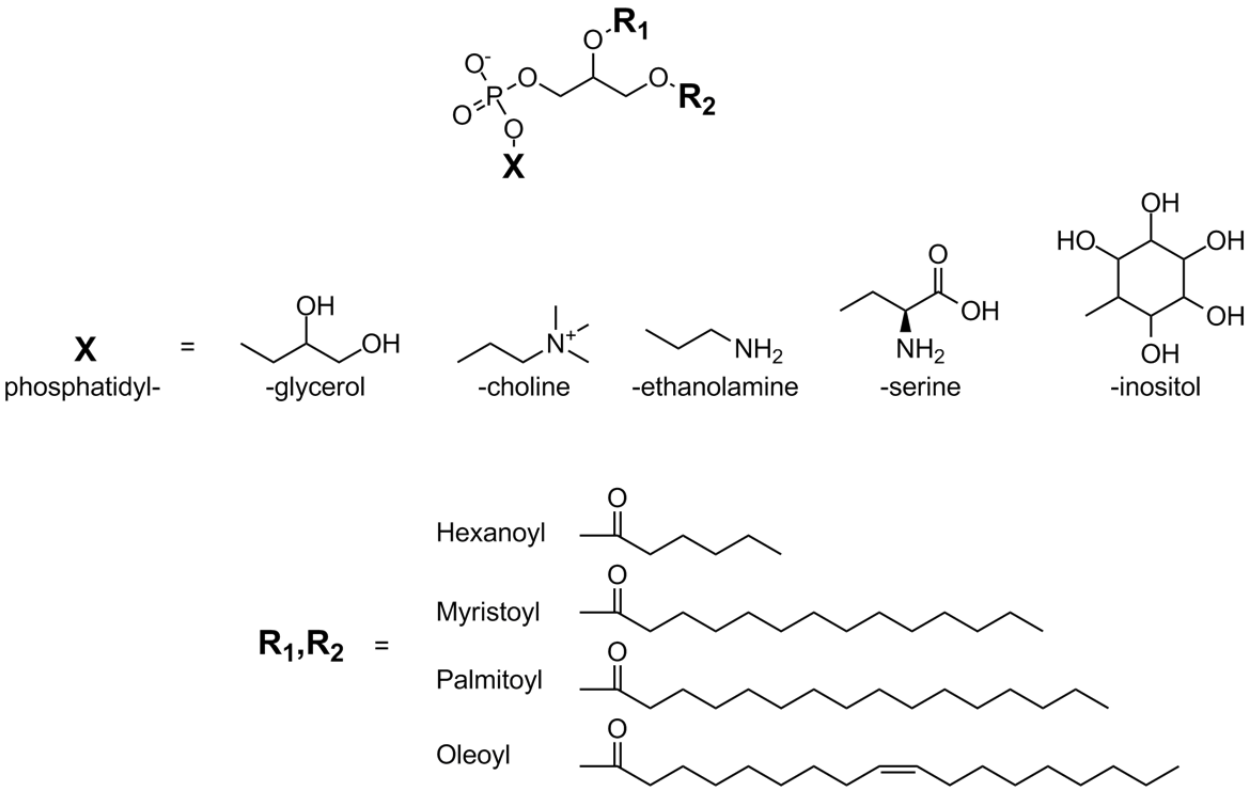

Figure 1-1: Examples of a few phospholipid head groups and fatty acid chains. The X marks where the headgroups are attached while R_n represents where the chains reside.

Phospholipids tend to spontaneously aggregate into various assemblies in aqueous solutions when their concentration exceeds the so-called critical micellar concentration (CMC). This is primarily due to the hydrophobic effect. Water molecules tend to form intermolecular hydrogen bonding networks with lipid headgroups, but not with their non-polar chains. Thus, at concentrations less than the CMC, phospholipids exist as monomers with a cage-like layer of water molecules surrounding the alkyl chains in an entropically unfavourable configuration. When concentrations reach the phospholipid CMC, aggregates with hydrophobic cores spontaneously form. These structures reduce the disruption of the water hydrogen bonding network and thus, minimize the free energy of the system. The morphology of the aggregates that are formed are a function of the size of the phospholipid headgroup (a_o) relative to the volume (v) and length (l_c) of the acyl chains.[1] This is encapsulated in the so-called critical packing parameter (p):

$$p = \frac{v}{a_o l_c} \qquad \text{Equation 1}$$

Table 1-1 summarizes the relationship between the lipid shape, p and the aggregate structure for phospholipids. Short chain phospholipids with a 5-9 carbon units on average, take the form of micelles and pack in structures possessing high surface curvature.[2] However, owing to the large carbon chains and headgroups of most phospholipids, bilayers are the most likely assemblies found above their CMCs.

Table 1-1: Summary of the relationship between chain length of phospholipids, the critical packing parameter (p), the corresponding shape of the lipid and the lipid aggregates that result from those shapes. Figure adapted from Israelachvili et al.[1] and supplemented with data from Ma et al.[2]

Chain Length	p	Shape	Aggregates Formed
5-9	$< \frac{1}{3}$	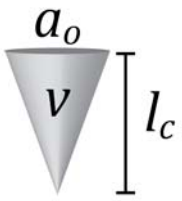	
> 9	$\frac{1}{2} - 1$	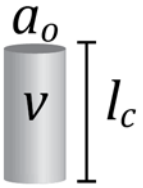	

Phospholipids packed within the lamellae structure of bilayers interact with each other primarily through Van der Waal attractions between the acyl chains. These attractions scale by the length and level of saturation of the chains. Hence, the strongest attractions occur for phospholipids with large saturated chains. Short chains do not allow interactions over a large chain surface area while unsaturated "kinked" chains do not allow close packing of the lipids. Single component phospholipids exist either in the gel state (or solid ordered phase) or the liquid-crystalline state (or liquid disordered phase). The temperature at which the transition from one state to another occurs is known as the melting temperature (T_M). At temperatures below T_M, lipids exist in the gel state, which is characterized by the tight packing of lipids with the acyl chains fully extended in an all *trans* conformation. At temperatures above T_M, lipids adopt the liquid-crystalline state and thus, possess much greater mobility. The thermotropic

state of a phospholipid bilayer has a major influence on its permeability, fusion behaviour and ability to allow molecular docking.

In addition to the intrinsic atomic motions, a phospholipid molecule is also dynamic as a whole within a bilayer. There are three main types of whole body motions that lipids undergo, as illustrated in Figure 1-2, with vastly different timescales. At one extreme, rotation of the lipid molecule about an axis parallel to the bilayer normal is very fast, with correlation times on the order of nanoseconds.[3] At the other end, uncatalyzed flipping of the lipid molecule between leaflets (i.e. "flip-flop" motions) is very slow, occurring over hours. Between those two extremes, lateral diffusion of lipids within the bilayer plane occurs with diffusion coefficients of 10^{-9} to 10^{-8} cm^2/sec.

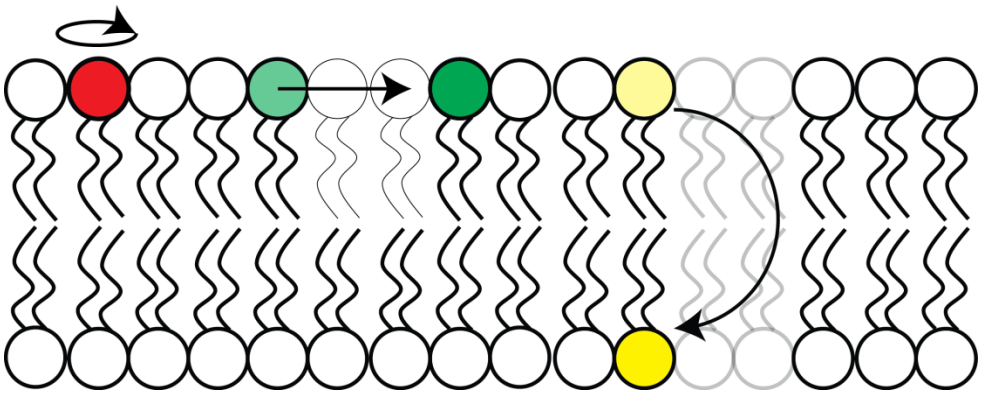

Figure 1-2: Whole body motions typically found in lipid membranes. The red highlighted lipid displays rotational motion around an axis parallel to the bilayer normal. The green highlighted lipid shows lateral diffusion behaviour. The yellow highlighted lipid exhibits "flip-flop" between the two leaflets.

In particular, lateral diffusion of constituents allows the lipid bilayer to accommodate distinct heterogeneous environments within its milieu and also facilitates the performance of a variety of critical functions.[4–9] Lateral diffusion also plays an important role in intramembranous drug trafficking and distribution.[10–15] All of this has provided an impetus to develop increasingly

sophisticated techniques to measure lateral diffusion within bilayers. In Chapter 5, the measurement of the lateral diffusion of phospholipids will be dealt with in detail.

1.2 Model Membrane Mimetics

In this section, three types of membrane mimetics will be discussed: liposomes, bicelles and supported bilayers. For each, a basic definition will be proffered, and their morphology and synthesis will be reviewed with a brief mention of the applications they have enjoyed. In addition, within the discussion of supported bilayers, polymer spheres made of N-isopropylacrylamide will be given special mention as supports due to their importance to this thesis.

1.2.1 Liposomes

Liposomes are spherical lipid bilayers with an aqueous core. Liposomes can be classified into four main categories (as shown in Figure 1-3): large multilamellar vesicles (LMVs), giant unilamellar vesicles (GUVs), large unilamellar vesicles (LUVs) and small unilamellar vesicles (SUVs).

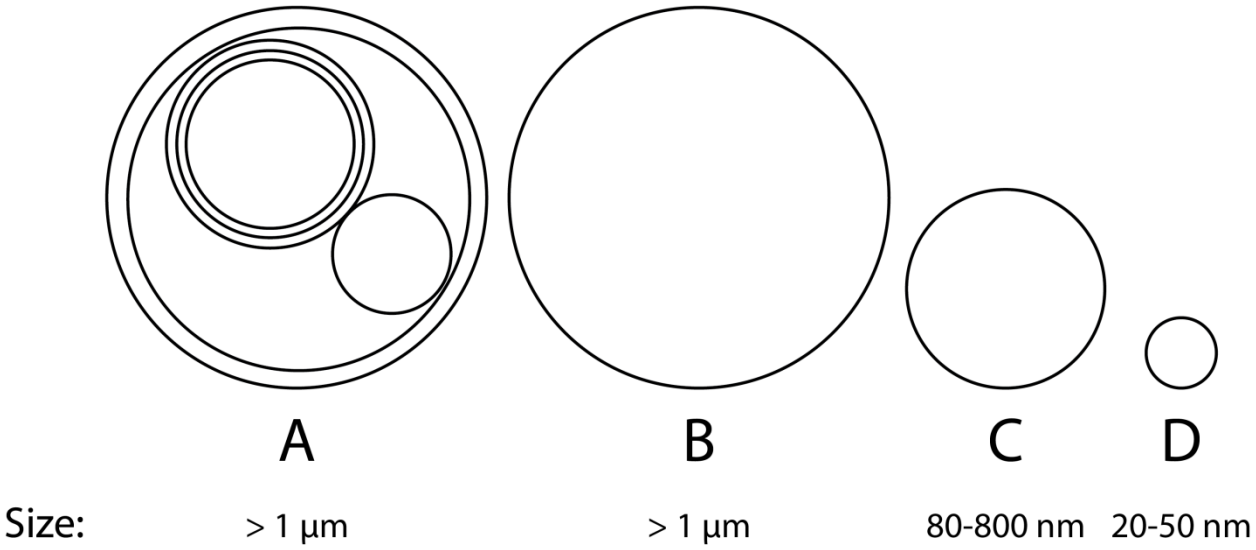

Figure 1-3: Illustration of the four main types of liposomes. A single outline represents a bilayer. (A) A large multilamellar vesicle (LMV). (B) A giant unilamellar vesicle (GUV). (C) A large unilamellar vesicle (LUV). (D) A small unilamellar vesicle (SUV).

LMVs are usually on the order of tens of microns in size and consist of multiple lipid bilayers and smaller entrapped vesicles. By virtue of being the most thermodynamically stable form, they can be easily formed by hydrating a dry lipid film. In fact, the first structures observed by Bangham et al.[16], credited to be the first observation of liposomes, were LMVs resulting from the simple hydration of a lecithin film.

GUVs possess the same size dimensions as LMVs but are unilamellar. Synthesis of a monodisperse batch of GUVs reproducibly has proven to be quite challenging. A popular method to prepare dilute concentration of GUVs in low ionic strength buffers involves applying electrical fields to a lipid film containing chamber that is sandwiched between electrodes made of platinum wire or indium tin oxide. To bring the GUVs up to physiological salt concentrations, a subsequent solvent exchange needs to be performed.[17] Another common method involves the re-hydration of a dehydrated lipid film deposited from unilamellar vesicles. The presumably single lamellae lipid film usually forms a polydisperse suspension of GUVs in buffer, which could be rendered monodisperse by extrusion through membranes with well-defined pores.

LUVs, in contrast to GUVs, are ca. 80-800 nm in diameter. Depending on the size of LUVs that are desired, numerous methods are available for their preparation. A popular method to prepare a concentrated, monodisperse batch involves extruding LMVs through polycarbonate membranes with pore sizes at a maximum of 200 nm. If a concentrated batch of monodisperse LUVs are desired with diameters greater than 200 nm, detergent dialysis is often employed: a detergent solubilized lipid solution is subjected to slow dialysis against non-detergent containing buffer, leading to the formation of LUVs. An easier alternative though, is the dehydration-hydration method described above which can also be used to make LUVs, albeit with extrusion through membranes with an appropriate pore size.

SUVs are liposomes of small dimensions, usually around 20-50 nm in diameter. Due to the high membrane curvature energy inherent in their small structures, SUVs are the least stable liposomes. Sonication of a dispersion of LMVs is the most common method of SUV preparation, in which the size of the aggregates can be controlled via sonication power. Extrusion through < 50 nm pored membranes, as described above, can also be used to form SUVs.

In terms of applications, liposomes have been utilized heavily in both fundamental and applied research. They have been the choice as mimetics of rudimentary cell membranes for biophysical interrogations using a wide variety of microscopic and spectroscopic techniques, since they allow control over lipid composition, size, lamellarity and stability. Also, due to the cargo space available within liposomes and the ability to easily functionalize their surface, they have unsurprisingly been subject to intense research as drug delivery vehicles, with over 20 liposomal drug formulations approved or under development.[18–22]

1.2.2 Bicelles

Bicelles are *B*ilayered m*ICELLES* and consist of at least two lipids with vastly different hydrophobic chain lengths. Purely phospholipid based bicelles are made up of two phospholipid molecules with vastly mismatched acyl chain lengths. Depending on the molar ratio (q) of the long-chain and the short-chain lipid, a variety of bicelle forms can be obtained as shown in Figure 1-4. As discussed before, short-chain lipids tend to form micelles while long-chain lipids form lamellar structures. Mixtures of the two tend to produce either small, disc-like bicelles or large lamellae perforated with holes.

Discoidal bicelles occur when a relatively high concentration of short-chain lipids are used, such that $1 < q < 3$. The disc-like morphology consists of planar, long-chain lipid rich, lamellae rimmed by the short-chain lipids. The size of these bicelles is dependent on the q value at a particular temperature and can range from 16 to 40 nm in diameter.[23] At lower concentrations of short-chain lipid ($q > 3$), Swiss cheese like lamellar structures are obtained. These perforated lamellae consist of bilayers of long-chain lipids pierced with short-chain lipid rich holes.

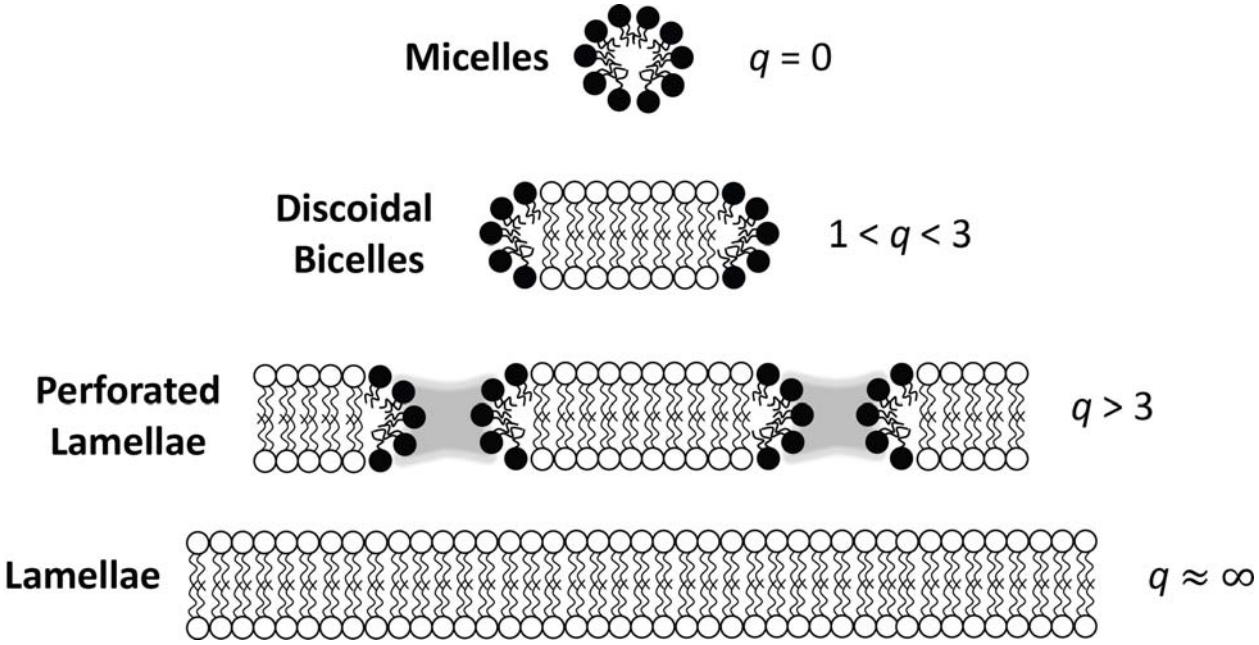

Figure 1-4: Lipid bicellar aggregates that are obtained at different *q* values. The value of *q* is determined by the equation: $\frac{[\boldsymbol{long\ chain\ lipid}]}{[\boldsymbol{short\ chain\ lipid}]}$. Adapted from Macdonald and Soong.[24]

Although idealized representations of bicelles show a neat segregation of the short- and long-chain lipid, mixing of the two lipids has been experimentally shown to occur at temperatures above T_M.[25] What this entails essentially is the migration of the short-chain lipid to the planar, long chain lipid rich region. This mixing results in a morphological change in the bicelle, since the surface area of the bicelle planar region increases due to the addition of lipids from the curvy regions. For discoidal bicelles, this mixing manifests in the elongation of the bicelles. For perforated lamellae, the lipid mixing entails fewer and / or smaller holes due to a loss of the short chain lipid to the bicelle plane.

Reproducible bicelle preparation is quite simple and can be accomplished without special equipment. Typically, a pre-mixed powder or lipid film containing both lipids is hydrated with buffer. An application of a few cycles of cooling, heating and vortexing is then usually employed to homogenize the sample. Another method involves introducing the short-chain lipid as micelles to lipid films or pre-formed liposomes of the long chain lipid. Although less

commonly used, this method is useful for applications in which pre-incorporation of molecules within the micelles aid in their ultimate integration within the bicelle hydrophobic core, as is the case, for example, for incorporation of transmembrane proteins into bicelles.

Bicelles have enjoyed a wide variety of applications. Bicelles have been used to solubilize integral proteins for structure determination, and have also been used to impart orientation order to both integral and globular proteins due to their propensity to align parallel or perpendicular to the magnetic field. Thus, bicelles have enjoyed much fanfare in NMR and electron paramagnetic resonance (EPR) studies, which have been extensively reviewed in the literature. [24,26,27] Bicelles have also been used to crystallize membrane proteins for X-ray structural studies,[28–30] and, to coat solid substrates.[31–33]

Bicelles have also been employed for molecular delivery applications. Even though they do not have an aqueous cargo space like liposomes, the bicelle hydrophobic core can act as a reservoir for hydrophobic drugs or proteins. A concrete example of this is the use of bicelles for dermatological applications.[34,35]

1.2.3 Supported bilayers

Supported phospholipid bilayers (SPBs) have been an intense area of research since their development about three decades ago. SPBs are intact lipid bilayers of various compositions deposited on a surface. The surface could be “hard” or “soft”, and could be planar or spherical.

Historically, the first SPB was developed by Brian and McConnell using a planar, smooth glass surface.[36] It was quickly recognized that though the hard surface provided 1 – 2 nm of hydration, it was not enough to ameliorate deleterious effects on large macromolecules

embedded in the lipid bilayer. As a solution to this problem, it was envisioned that highly hydrated polymeric surfaces would be able to decouple the lipid bilayer from the underlying support. Spinke et al.[37] provided the first example of this when they developed a lipid bilayer supported on a soft surface composed of 2-hydroxyethyl acrylate that was pre-coated to a planar gold surface. Other polymers such as cellulose or polyethylene glycol have also been used as soft supports. [38–40] The hydration offered by these polymers rendered the planar bilayers air-stable, a key development towards their use in biosensors.[41–43]

Though planar supported systems were used extensively as artificial cell membranes, it was recognized that spherical supports offered the requisite curvature for cell membrane shape mimicry. Interestingly, phospholipid coating of a soft surface was accomplished prior to that of a hard surface in the case of spherical supports. Gao and Huang[44] were the first to produce a spherical supported membrane when they coated gold nanoparticle entrapped agarose-gelatin spheres with phospholipids. This was followed by Bayerl and Bloom[45] who used hard polystyrene beads as supports for lipid bilayers. Numerous attempts have followed in their steps using various hard[46–54], mesoporous[55–60] and soft materials[61–67].

A subset of soft material that has not enjoyed much fanfare in the field is “smart” materials. These materials respond to external stimuli, like temperature, pH, light and ligands, to produce profound changes in material properties. Although there are many examples of using smart materials to change the properties of lipid bilayers[68–84], there are only a few examples of coating them with lipid bilayers[85,86]. A pioneering example that illustrates the utility of lipid coated smart material was provided by Kiser et al.[85], in which they demonstrated controlled drug delivery from lipid coated pH sensitive microgels.

Among smart polymers, poly(*N*-isopropylacrylamide) (pNIPAM) is arguably the most popular polymer explored in the literature. Due to its importance to the work presented in this thesis, its characteristics and synthesis will be discussed in much more detail before discussing the strategies that are used to generally create supported bilayers.

1.2.3.1 Basics of pNIPAM microgels

NIPAM is a water soluble monomer (see Figure 1-5 for structure) that can be polymerized into linear or gel forms. PNIPAM is thermo-responsive and hence, is considered a smart polymer. Typically, pNIPAM undergoes a large volume change at a lower critical solution temperature (LCST) of ~32°C. In the context of gels, this property is known as the Volume Phase Transition (VPT), and entails a severe shrinking of the overall gel size. The transition can be explained by invoking the hydrophobic effect that predominates at high temperatures. Basically, at temperatures below the LCST, pNIPAM chains are rendered water soluble due to hydrogen bonding of water molecules to the amide moiety. The water layer extends to the hydrophobic isopropyl group as a clathrate. At high temperatures, the hydrogen bond network is disrupted resulting in the attractive Van der Waal forces between the hydrophobic groups dominating. This results in the expulsion of water from the matrix and a collapse of the chains into a compact conformation.

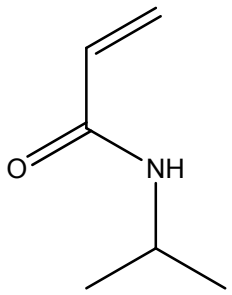

Figure 1-5: Structure of N-isopropylacrylamide.

PNIPAM gels can be formed into slabs, films, and spheres. A subset of pNIPAM gels that have been a subject of intense research is microgels. PNIPAM microgels are sub-micron to micron sized, and are often chemically crosslinked. Pelton and Chibante[87] were first to synthesize pNIPAM microgels via an aqueous free radical precipitation polymerization in 1986 using methylene bis(acrylamide) (MBA) as the chemical crosslinker. The ease, safety, reproducibility and the scalability of this method has made it the most common method that is still utilized to synthesize pNIPAM microgels. The free radicals in this method are usually produced through thermal decomposition of initiators, such as persulfates. At high temperature, the initiators decompose into activated radicals that attack free pNIPAM and MBA monomers, resulting in a growing polymer chain. When a pNIPAM chain reaches a critical length, it collapses and precipitates out of solution. This precursor particle act as a nucleation site for further growth through oligomer deposition and particle aggregation. The final size of the microgel can be tailored to specific size ranges by adjusting the stirring speed, temperature[88], initiator concentration[89], crosslinker concentration[90] or by adding a surfactant[89,91].

Besides size, the microstructure of the microgel can be controlled as well. Usually, this is accomplished by a careful selection of a crosslinker with a favourable reactivity ratio and hydrophilicity. MBA, for example, has a higher reactivity ratio compared to NIPAM resulting in its propensity to occupy the interior of the fully formed microgel.[92] This results in a hairy microgel with a highly crosslinked interior.

PNIPAM microgels have also been functionalized with a host of different chemical groups such as carboxylic acids[93,94], amines[95–97], phenylboronic acids[98], and “clickable” groups[99].

Depending on the reactivity ratio of these groups with pNIPAM, the distribution can be readily controlled albeit, at times, with less than quantitative incorporation. As an elegant example of functional group distribution, Hoare and McLean[100] have shown how the different carboxylic acid containing monomers distribute within the pNIPAM matrix simply as a function of their reactivity ratio.

Another way of fabricating microgels with controlled crosslinking and functional group density involves tweaking the overall microgel architecture. In this regard, microgels with a chemically and physically distinct core and shell provide a convenient morphology to selectively place functional groups either in the interior or the surface. The core-shell pNIPAM synthesis was first introduced by Jones and Lyon[101] using a "seed and feed" approach, where pre-fabricated purified pNIPAM cores were used as seeds on which the shell of a different monomer composition was added in a controlled fashion, presumably to avoid flocculation of the growing microgels. In subsequent attempts, however, addition of bulk monomers to unpurified microgel seeds was found to produce colloidally stable microgel dispersions as well.[102–104]

1.2.4 Lipid immobilization techniques on soft surfaces

Bilayer deposition on soft surfaces has generally been achieved through either the Langmuir-Blodgett (LB) method or lipid vesicle mediated self-assembly. The LB method involves transferring a monolayer already spread at the air-water interface in a Langmuir trough to the target substrate, followed by dipping of the adsorbed monolayer on top of a free lipid leaflet, resulting in a bilayer. This method was first used by Kühner et al.[105] to deposit lipid bilayers to polyacrylamide coated planar supports, a decade after its first utility as a means to coat a glass

surface with phospholipid bilayers. The distinct advantage of this method is that it allows the creation of bilayers with asymmetric compositions, which depending on the application, makes up for its laboriousness.[43] This method, however, cannot be extended to spherical substrates.

With regards to using liposome self-assembly to coat soft surfaces, maximizing the strength of lipid-polymer adhesion is key to a successful deposition of bilayers. Lipid adsorption on soft surfaces is generally inefficient due to the lack of specific interactions between the lipid reservoir and the substrate.[85] There are four main strategies that are employed to increase adhesion between lipids and soft surfaces:

1) Electrostatic binding of charged vesicles to oppositely charged surfaces.
2) Incorporating functional groups to the lipid vesicles which are reactive to those pre-installed on the support surface.
3) Modifying the support with hydrophobic groups that can sequester lipid vesicles.
4) Using unilamellar vesicles as polymerization reactors for entrapped monomers.

Binding of lipids to soft surfaces via electrostatics is achieved by incorporating charged lipids in the lipid vesicle and by co-polymerizing or adsorbing charged polymers on the surface.[2,86,106–108] In Chapter 3, a successful deployment of this method is demonstrated albeit using bicelles, rather than liposomes. This method is fast and convenient, but is often sensitive to the environment ionic strength and pH. Furthermore, subsequent fusion of charged vesicles into bilayers on the surface is usually prohibited, owing to the lack of close inter-bilayer apposition due to Coulombic repulsion between the liposomes. This could be advantageous for applications that require adhesion of liposomes with distinct cargo to a surface[109], and is exploited in Chapter 4 to make liposome coated microgel complexes, but is a bane for lipid bilayer coating applications. Lastly, due to the requirement of incorporating specific charged

groups in the vesicle at non-negligible amounts, pure one component lipid compositions cannot be used with this method.

To couple lipid vesicles to surfaces strongly, mutually reactive moieties are incorporated on the lipid and polymeric surface. An example of this method was demonstrated by MacKinnon et al.[110], in which biotinylated lipid vesicles were bound to avidin modified pNIPAM microgels. DNA-aptamer conjugation has also been employed to couple lipids to a polymer.[111] Chapter 4 describes another example of this strategy where amine incorporated liposomes were adsorbed covalently to activated pNIPAM microgels.

Generally, the main advantage of the mutual reactivity method is the strong coupling that is achieved between the two surfaces in very mild conditions and, essentially, "on-demand". However, the complicated synthesis, high cost or low incorporation of the reactive groups are usually the main issues that are confronted when using this strategy. Also, the final lipid coating that is deposited on the surface still contains unreacted moieties, which may be undesirable especially for *in vivo* applications.

To coat surfaces with unconstrained lipid compositions, hydrophobically modifying the polymeric surfaces with sufficiently long alkyl-chains or phospholipids is employed.[103,104,112–115] These hydrophobic groups intercalate into the lipid bilayers of the vesicles, effectively immobilizing them to the surface. Chapter 2 shows an example of this, in which tetradecyl modified pNIPAM microgels were coated with a bilayer, using LUVs made of one type of phospholipid only. The main disadvantage of this method is that the hydrophobic modification could be potentially laborious, time consuming and incomplete. Furthermore, high surface hydrophobic modification tends to destabilize the adsorbed lipid bilayers.[103] In terms of spherical supports, highly hydrophobic surfaces also lead to severe aggregation of the particles

in aqueous solutions at even moderate concentrations. Hence, scaling up the production of lipid-polymer complexes through this method can become problematic.

Hitherto, the discussion has exclusively focused on polymeric materials as support templates onto which lipids are introduced. Of course this is not the only route available to create lipid-hydrogel complexes. Alternatively, liposomes themselves have also been used as support templates, in the form of reactors. Generally, this entails the entrapment of monomers of a typical polymeric formulation inside liposomes, followed by selective polymerization. LUVs around 100 nm in diameter have been the template of choice for this strategy. Monomers are loaded into LUVs through extrusion[116–119] or microfluidics[120], with subsequent polymerization carried out with care so that only the entrapped contents undergo gel formation. For the case of GUVs, monomers can also be injected into the large vesicle.[121] The advantage of this method is that the size and lamellarity of the bilayer coating can easily be controlled. However, that is only true for LUVs that are about 100 nm in diameter. Monodisperse LUVs approaching the size of a micron, which are useful for optical and NMR biophysical studies, are usually hard to prepare. Hence, since the liposomal template in this strategy is the ultimate determiner of the final lipid-polymer complex, large scale production using this strategy has only been limited to smaller LUVs.

1.3 Fluorescence and NMR Spectroscopic Characterization of Membranes: Basic Theory

Membrane mimetics in this thesis have been studied using both fluorescence and NMR spectroscopic techniques. In this section, the basic theory for both of these techniques will be

concisely presented to provide appreciation for the experiments that were conducted. The details for both haven been adapted from standard texts and articles.[122–128]

1.3.1 Fluorescence

Fluorescence is typically observed from molecules possessing conjugated systems (i.e. fluorophores) and is a type of luminescence. To describe the absorption and emission of light that exhibit the fluorescence phenomenon, a Jablonski diagram is usually employed as shown in Figure 1-6. When a fluorescent molecule is excited using light at an appropriate wavelength, electronic transitions occur that excite molecules from the ground vibrational state (SE_0) to higher singlet states (SE_1 or SE_2). Nuclear coordinates are considered static during this time since electronic transition occurs on timescales much shorter than nuclear vibrational motions, as per the Franck-Condon principle. After excitation, relaxation to the ground state occurs through a number of non-radiative pathways. Within the singlet states, relaxation can occur within the excited states (SE_2->SE_1) in a process known as internal conversion. Relaxation also occurs between the vibrational energy levels within an excited state. Fluorescence emission itself, however, is due to a molecule relaxing back to S_0. Since some of the energy absorbed by the fluorophore is dissipated through non-radiative pathways, fluorescence emission is of a different energy (i.e. wavelength) than excitation. This wavelength difference is known as the Stoke's shift.

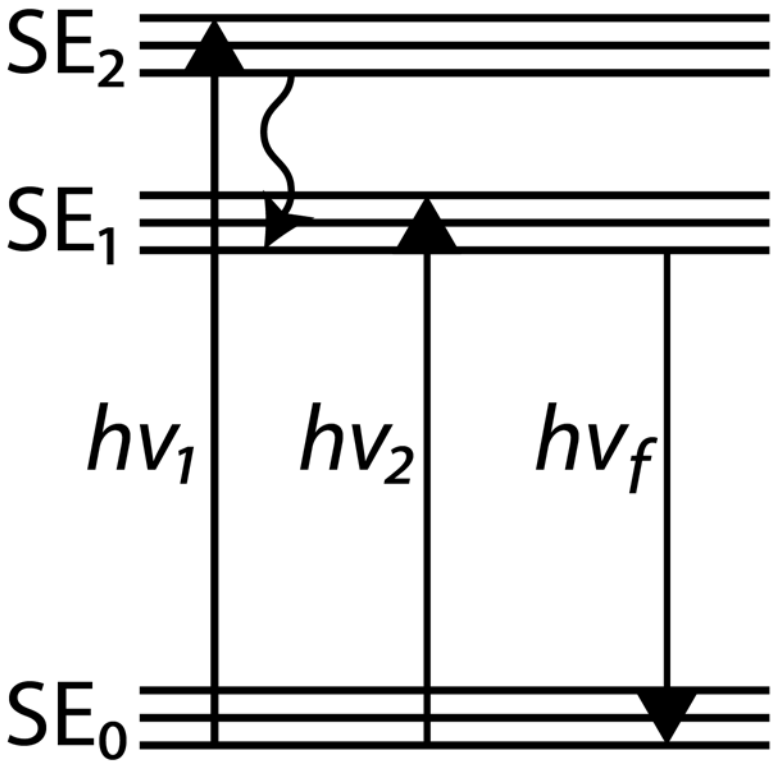

Figure 1-6: A simplified Jablonski diagram. SE_n are electronic states, while the straight parallel lines represent vibrational states. The straight arrows represent transitions from one electronic state to another. The squiggly arrow represents the internal conversion phenomenon.

One of the most important properties of a fluorophore is its quantum yield (*Q*), which can be described as the ratio of photons emitted to those absorbed. It serves as a rudimentary gauge of how brightly a molecule can fluoresce. Another way to think about *Q* is by considering the emissive rate of the fluorophore (Γ) vis à vis the non-radiative decay rate (n_r) via the following equation:

$$Q = \frac{\Gamma}{\Gamma + n_r} \qquad \text{Equation 2}$$

An appreciation that is gained from Equation 2 is that *Q* is near unity if the fluorophore does not experience extensive non-radiative decay. The rhodamine class of fluorophores have

some of the highest *Q* values and hence, enjoy ubiquitous use in fluorescence based experiments.

The loss in *Q* is known as fluorescence quenching, and can occur due to a variety of reasons. It can also be profoundly useful, as will be seen in Chapters 2, 3, and 4. One source of quenching is photobleaching, in which the fluorophore chemically degrades due to prolonged excitation and subsequent emission of photons. Though often regarded as a nuisance for most applications, photobleaching is, however, profoundly useful to study diffusion within lipid bilayers. The other types of quenching stem from the contact of the fluorophores with specific molecules called quenchers. When fluorophores interact with quenchers that render them non-fluorescent either through chemical modification or complexation, it is referred to as static quenching. A good example of this is the quenching of 7-nitro-2-1,3-benzoxadiazol-4-yl (NBD) bearing molecules via dithionite reduction to its non-fluorescent amino form, as shown in Figure 1-7. In contrast to static quenching, dynamic quenching is a result of the energy transfer or collisions between fluorophores and quenchers. This type of quenching is the basis for Förster resonance energy transfer (FRET) based techniques and also, techniques to measure accessibility of molecules to domains. Furthermore, fluorophores also experience self-quenching at high concentrations, due to intermolecular non-fluorescent complex formation.[129] This property is inherent to all fluorophores, but is more pronounced in some. For example, calcein exhibits quenching when increased above 20 mM.[130] While this property destroys the concentration linearity for quantification purposes, it is profoundly useful for studies where content leakage is measured from large macromolecular systems, like liposomes.

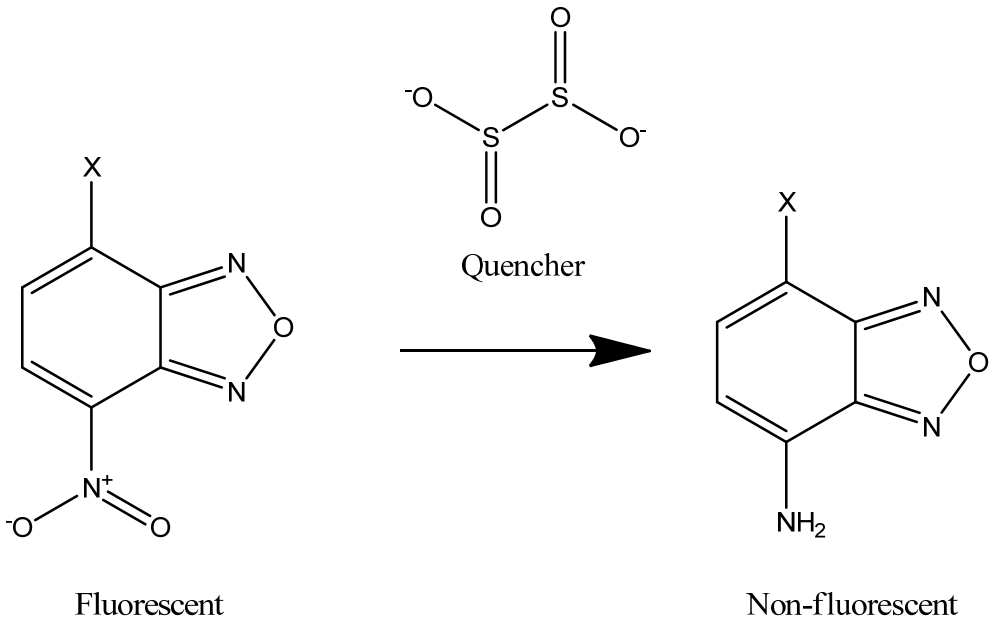

Figure 1-7: Dithionite static quenching of a fluorophore bearing NBD.

1.3.2 Solid State NMR (ssNMR)

ssNMR provides a non-destructive method for interrogating structural and dynamical aspects of the lipid bilayer. NMR techniques have primarily been label-free and used nuclei with favourable NMR properties, like ^{1}H and ^{31}P. The molecular tumbling that is responsible for narrow linewidths in liquid state NMR are absent in the solid state, and hence ssNMR linewidths are quite broad. In the following section, a brief introduction to NMR theory of spin-1/2 nuclei will be presented. This will be followed by an introduction to the ^{31}P chemical shift anisotropy (CSA) due to its usefulness in studying lipid members in general, and its importance towards understanding the ssNMR experiment presented in Chapter 5. Also, the unique ssNMR technique of Magic Angle Spinning (MAS) will then be outlined as it relates to the CSA.

1.3.2.1 Basic Theory

In addition to the intrinsic properties of charge and mass, some nuclei also exhibit a magnetic moment (μ) by the virtue of possessing the property of spin. In terms of a quantum mechanical operator, the magnetic moment for a nucleus can be described by:

$$\hat{\mu} = \gamma \hat{I} \qquad \text{Equation 3}$$

where γ is the magnetogyric ratio and $\hat{I}$ is the spin angular momentum operator. When a nucleus with a magnetic moment is placed in an external field (B_0), the nucleus experiences the so-called Zeeman interaction with the field which can be described by the following Hamiltonian:

$$\hat{H} = -\gamma \hbar B_0 \hat{I} \qquad \text{Equation 4}$$

If the nucleus is spin-1/2, two energy levels are obtained from this Hamiltonian, which are:

$$E_{\pm\frac{1}{2}} = \mp \frac{1}{2} \gamma \hbar B_0 \qquad \text{Equation 5}$$

where $E_{+\frac{1}{2}}$ and $E_{-\frac{1}{2}}$ represent the lower and higher energy level, respectively. To gain an intuitive understanding of the NMR phenomenon, classical mechanics is usually evoked. So, for an ensemble of molecules at thermal equilibrium in an external field B_0 oriented along the z-axis of the Cartesian plane, the two energy levels will be populated according to the Boltzmann distribution with the lower energy level possessing a slightly higher population. This unequal distribution leads to the formation of a net magnetization (M) that is parallel to the magnetic

field for $\gamma > 0$ (common) or anti-parallel to the magnetic field for $\gamma < 0$ (rare). In the B_0 field, M experiences a torque and hence, precesses around the field at a characteristic frequency. This frequency is known as the Larmor frequency (ω_0):

$$\omega_0 = \gamma B_0 \qquad \text{Equation 6}$$

Since ω_0 is a function of the magnetogyric ratio and scales with B_0, it is distinct for each nucleus at a particular external field strength.

To probe these energy levels in NMR, the precessing magnetization is perturbed by the application of an oscillating radio frequency (rf) pulse orthogonal to B_0. When the rf field (B_1) is at or near the Larmor frequency, it interacts with M to move it away from its equilibrium z position. The magnetization is said to be "flipped" by an angle, θ_j, such that:

$$\theta_j = \gamma B_1 \tau_{rf} \qquad \text{Equation 7}$$

where τ_{rf} is the duration of the B_1 field pulse application and j is the axis along which that pulse is applied. This results in the flipping the magnetization onto the xy plane. So, a $\frac{\pi}{2}_{\text{x}}$ pulse would result in M being flipped by 90^0 along the x-axis, and end up on the –y or y axis, depending on the preferred convention. Using a single or composite of these pulses, the magnetization can be manipulated in a variety of different ways to experience a range of complex interactions. The resulting magnetization is ultimately detected when M freely undergoes relaxation back to the z-axis. The two sources of relaxation to the equilibrium position are the spin-lattice (or T_1) relaxation and the spin-spin (or T_2) relaxation. T_1 relaxation is related to the return of the populations back to the Boltzmann distribution while T_2 relaxation

is related to the loss of coherence between the spins constituting M. Both of these are sample and temperature dependent, with T_2 being less than or equal to T_1.

The resulting free induction decay (FID) can be Fourier transformed from the time dependent decay to the frequency domain. Assuming that the magnetic field experienced by the spins is fully homogenous, the resulting Lorentzians have linewidths that are T_2 dependent with their full width at half-height (FWHH) characterized by:

$$FWHH = \frac{1}{\pi T_2} \qquad \text{Equation 8}$$

1.3.2.2 Chemical Shift Anisotropy in ^{31}P NMR of Membranes

The indispensable power of NMR comes from its ability to distinguish different chemical groups in a molecule via the so-called chemical shift. The chemical shift arises from a local magnetic field that the nucleus experiences in addition to B_0. This secondary field is the result of the circulation of electrons, which are induced by B_0 itself. The local field experienced by the nuclei, thus, can be summarized by:

$$B_l = B_0(1 - \sigma) \qquad \text{Equation 9}$$

where B_l is the local magnetic field experienced by a nucleus and σ is the shielding tensor. The shielding tensor is a 2nd rank tensor and is generally anisotropic. Diagonalizing σ by moving to the principal axis frame (PAF) results in the following 3x3 matrix:

$$\sigma^{PAF} = \begin{pmatrix} \sigma_{xx}^{PAF} & 0 & 0 \\ 0 & \sigma_{yy}^{PAF} & 0 \\ 0 & 0 & \sigma_{zz}^{PAF} \end{pmatrix}$$

where σ_{xx}^{PAF}, σ_{yy}^{PAF} and σ_{zz}^{PAF} are principal axis values whose magnitudes, by convention, are ordered as $\sigma_{xx}^{PAF} \leq \sigma_{yy}^{PAF} \leq \sigma_{zz}^{PAF}$. These values can be rendered quite useful for experimental purposes by expressing them as follows:

$$\sigma_{iso} = \frac{1}{3}\left(\sigma_{xx}^{PAF} + \sigma_{yy}^{PAF} + \sigma_{zz}^{PAF}\right) \quad \text{Equation 10}$$

$$\Delta_{red} = \sigma_{zz}^{PAF} - \sigma_{iso} \quad \text{Equation 11}$$

$$\eta = \frac{\sigma_{xx}^{PAF} - \sigma_{yy}^{PAF}}{\sigma_{zz}^{PAF}} \quad \text{Equation 12}$$

where σ_{iso} is the isotropic value, Δ_{red} is the reduced anisotropy[131] and η is the asymmetry factor.

The shielding tensor in the PAF can be moved to the lab frame by orienting B_0 in the PAF via polar angles (θ, ϕ), as shown in Figure 1-8. The chemical shift frequency can then be described by:

$$\omega_{i,j} = \omega_{iso} - \frac{1}{2}\omega_0\Delta_{red}\left(3\cos^2\theta - 1 + \eta\sin^2\theta_i\, cos2\phi_j\right) \quad \text{Equation 13}$$

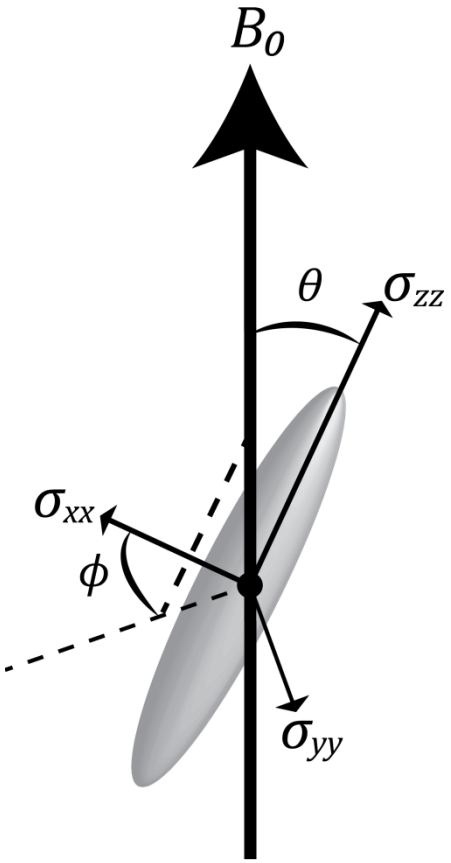

Figure 1-8: Orientation of B_0 in the principal axis frame using the polar coordinates (θ, ϕ). While θ is the angle between B_0 and σ_{zz}^{PAF}, ϕ is the angle between the projection of B_0 on the XY plane and σ_{xx}^{PAF}.

The molecular orientation dependent nature of the chemical shift has huge implications for ssNMR. In liquids, since tumbling allows molecules to sample all the orientations available, the orientation dependence is lost and instead, only an isotropic chemical shift is observed (Figure 1-9). A solid sample, however, contains molecules that are oriented along B_0 in fixed orientations. Hence, the resulting spectrum of such a sample is an amalgamation of the chemical shift frequencies experienced by each molecule and is known as a "powder" pattern. Examples of characteristic powder patterns are shown in Figure 1-9.

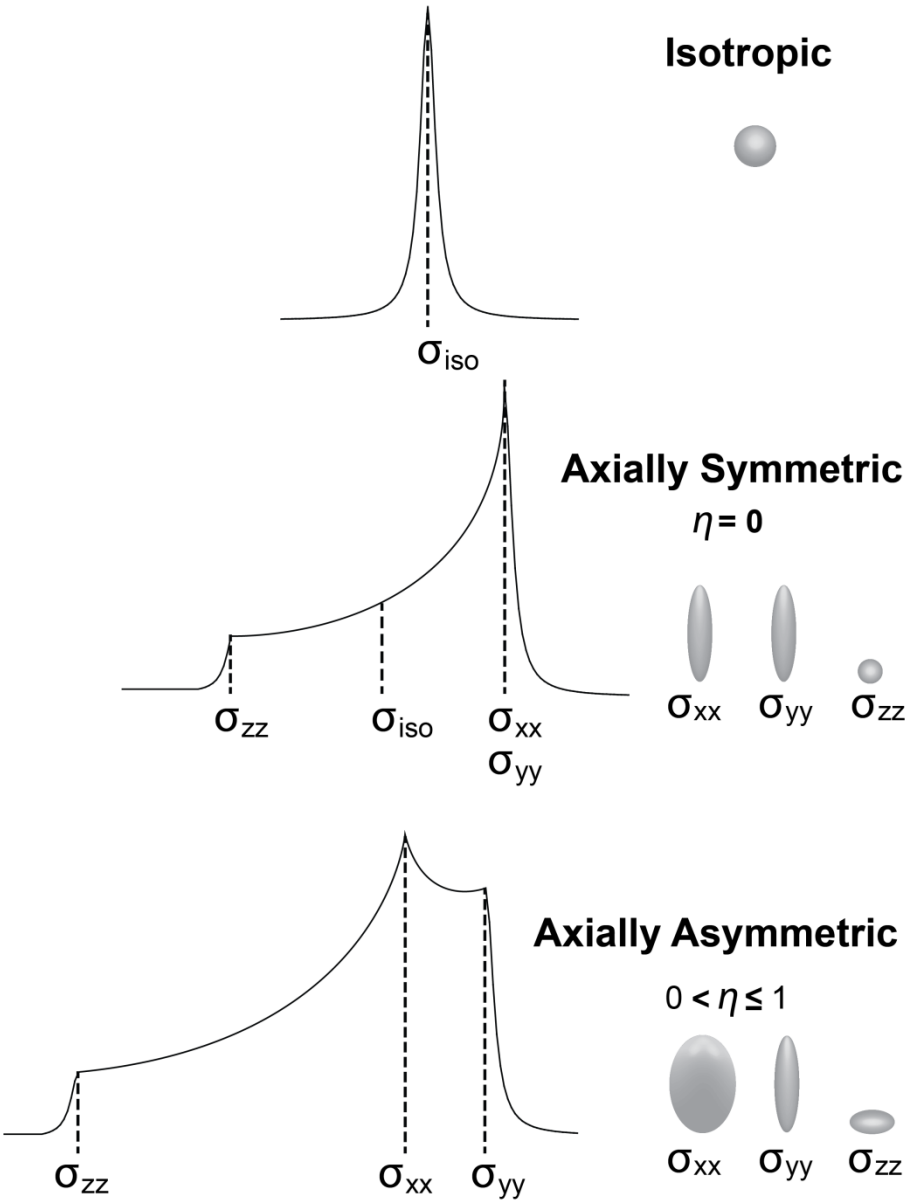

Figure 1-9: Illustration of the characteristic patterns and principal axis "faces" of the isotropic, axially symmetric and axially asymmetric cases. The orientations of the principal axes are hypothetical and are simply meant to exhibit a possible asymmetry that might result in the corresponding power pattern.

Of particular importance to ^{31}P NMR spectra of spherical phospholipid bilayers is the axially symmetric case. As discussed before, whole body rotation of a lamellae embedded phospholipid axially about the bilayer normal occurs at a timescale of nanoseconds. Hence, on the NMR timescale (> milliseconds), the asymmetry of the phospholipid headgroup is lost due

to motion averaging. The chemical shift frequency then only depends on θ. This implies that the chemical shift frequencies will effectively reflect the orientation of the tensors parallel ($\omega_{\parallel} = \omega_{zz}^{PAS}$) and perpendicular ($\omega_{\perp} = \omega_{xx}^{PAS} = \omega_{yy}^{PAS}$) to the magnetic field, B_0. Hence, Equation 13 for an axially symmetric case can be expressed as:

$$\omega_i = \omega_{iso} + \frac{1}{3}\Delta\,(3\cos^2\theta_i - 1) \qquad \text{Equation 14}$$

where ω_i is chemical shift frequency for a particular angle θ_i and $\Delta = \omega_{\parallel} - \omega_{\perp}$ is the magnitude of the residual chemical shift anisotropy (CSA).

The chemical shift frequency dependence on θ of phospholipids in a large vesicle is shown in Figure 1-10, and shows the rich orientation data that the powder pattern can provide. Also, Δ can also be used to approximate the size of the vesicle and the thermotropic state of its phospholipids, due to its sensitivity to both whole body tumbling and molecular motion constrains. Chapter 5 will provide an expanded discussion on these points and will also detail how the CSA can be leveraged to measure the lateral diffusion behaviour of phospholipids in spherical bilayers.

^{31}P powder patterns of phospholipid vesicles are quite broad. For example, a large vesicle made of phosphatidylcholines in the liquid crystalline state typically produce powder patterns with CSAs of 45 ppm. On the other hand, isotropic chemical shift differences between typical phospholipid headgroups are comparatively tiny, as shown in Table 1-2. Hence, the broad linewidths obtained from a sample of phospholipid vesicles are inherently of low resolution, which renders them non-ideal for cases where phospholipid species identification is paramount. The collapse of large CSA to isotropic chemical shifts can be accomplished through magic angle spinning (MAS), which will be discussed in the next section.

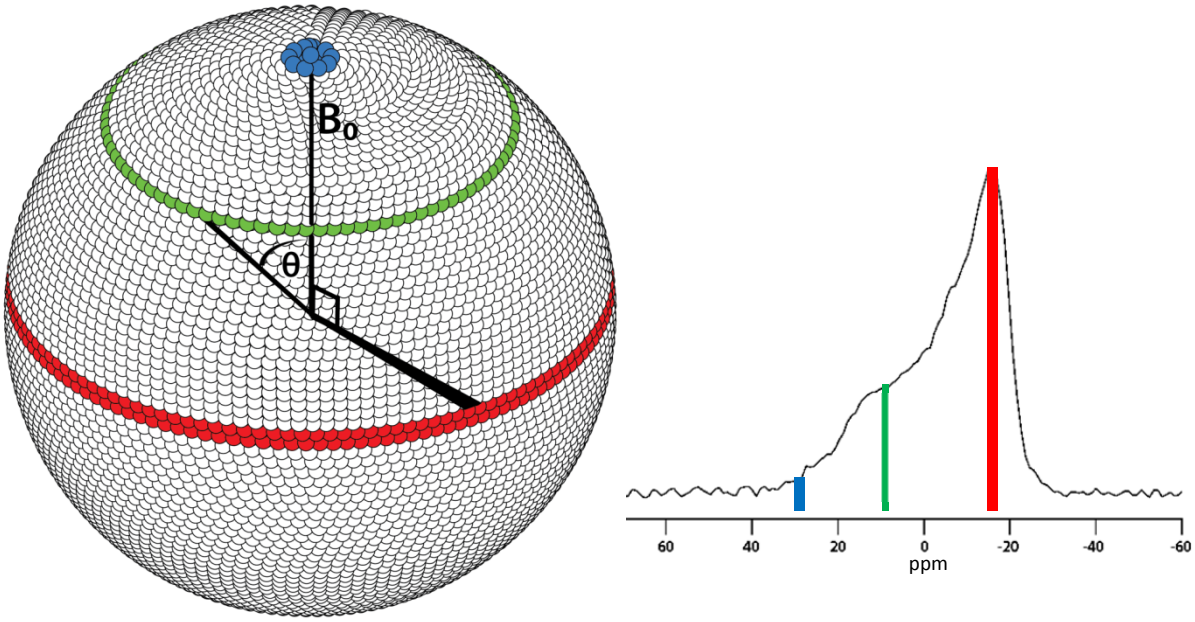

Figure 1-10: Characteristic ^{31}P powder pattern of an LUV. The axially symmetric experimental ^{31}P spectrum of an LUV made of 1-palmitoyl-2-oleoyl-*sn*-glycero-3-phosphocholine (POPC) in 0.2 M sucrose shows a θ dependent chemical shift, as exemplified by the coloured lines pertaining to cases when the lipids are parallel (blue), perpendicular (red) or at an angle in between, relative to B_0 (green) as predicted by Equation 14.

Table 1-2: A list of phospholipid headgroups and their corresponding isotropic chemical shifts (ppm) referenced to a 85% phosphoric acid standard. Data was gleaned from Meneses and Glonek.[132]

Phospholipid headgroup	Isotropic chemical shift (ppm)
Phosphatidylcholine (PC)	-0.84
Phosphatidylinositol (PI)	-0.28
Phosphatidylserine (PS)	-0.21
Phosphatidylethanolamine (PE)	0.00
Phosphatidic acid (PA)	0.34
Phosphatidylglycerol (PG)	0.57

1.3.2.3 Magic Angle Spinning (MAS)

Equation 14 for the axially symmetric case provides a clue about how to collapse the CSA to only the isotropic signal. At θ = 54.74°, the second-order Lengendre polynomial $(3\cos^2\theta - 1)$ is zero. Hence, at this so-called "magic angle", only the isotropic chemical shift remains. For the solid sample to experience the magic angle homogenously, mechanical spinning is employed. This is accomplished by loading the sample in a small (1-5 mm diameter) cylindrical holder called a rotor, that are inserted into modules that are pre-adjusted to the magic angle. Figure 1-11 shows an example of such a setup. With careful application of air or nitrogen to the attached turbine, the rotor can be made to spin stably.

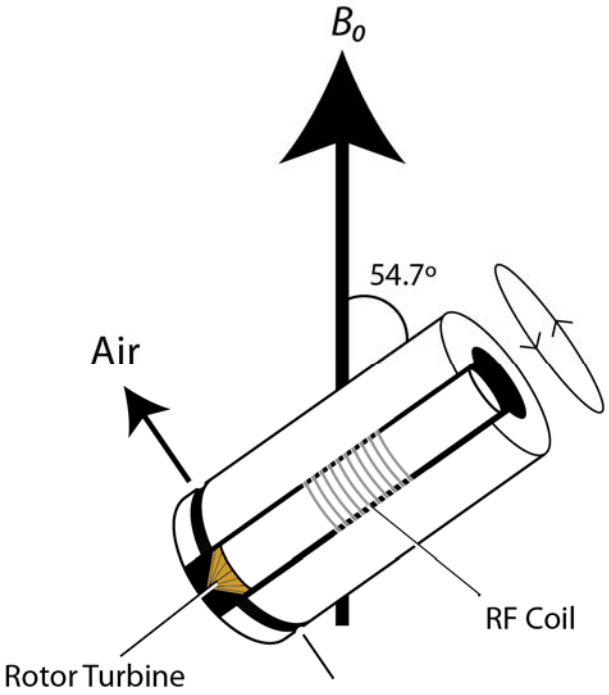

Figure 1-11: A rotor inside an MAS module. The big arrow represents the direction of B_0 while the small arrow shows the direction of the air flow. The air rotates the rotor by blowing against the small attached turbine. The module is set at $\theta = 54.74°$ relative to B_0 and the sample is pulsed via an rf coil inside the module.

To completely average the CSA and produce only the isotropic peaks, spinning speeds must be at least 3 times that of the CSA.[123] Spinning speeds of up to 110 kHz have already been demonstrated.[133] Achievement of even faster speeds is currently under development since MAS aids in mitigating the effects of a few other interactions that are orientation dependent as well.

In the case of wet lipid samples, however, a careful selection of the spinning speed is required. Effectively, the spinning speed must not be too fast or to slow, needing a veritable adaptation of the Goldilocks principle. Though very fast spinning speeds render narrow linewidths, friction from the interaction between the rotor and module walls imparts elevated temperatures to the sample, which can ruin the lipid content through drying and degradation. Also, higher speeds also increase the frequency of the unfortunate (and annoying) phenomenon of "sample liftoff". That is, due to the lubrication of the rotor end caps by the enclosed wet content, samples tend to leak (or more appropriately, shoot) out of the rotor at high speeds. On the other hand, a spinning speed that is slow relative to the CSA, would result in incomplete averaging of the CSA (and other interactions) which would result in spectra with broad low resolution peaks. Hence, the optimal conditions for running lipid samples via MAS, are intermediate (5-7 kHz) speeds in medium sized rotors (3.2 mm – 5mm) that are capable of supporting lightweight O-ring bearing endcaps that prevent sample dehydration and liftoff. An example of an endcap that was used in MAS experiments in this thesis is shown in Figure 1-12.

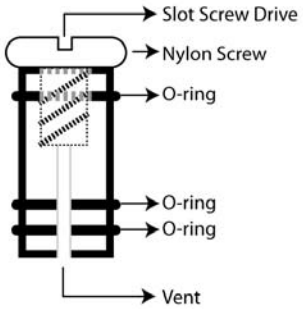

Figure 1-12: A custom made leak-proof rotor end cap.

1.4 Contributions of this Thesis

1.4.1 Lipid coated pNIPAM microgels

Chapters that follow in this thesis will detail the fabrication of a variety of novel lipid coated pNIPAM microgels, with portions reproduced from published papers. Specifically, Chapter 2 will detail the fabrication and characterization of a Lipogel, which is a single lipid bilayer coated hydrophobically modified pNIPAM microgel. We show that when the pNIPAM microgel undergoes the VPT, the lipid bilayer stays intact but protrudes away from the microgel surface, as shown in Figure 1-13. Portions of this chapter and Chapter 6 are reproduced from the paper published in 2011, with permission.[104]

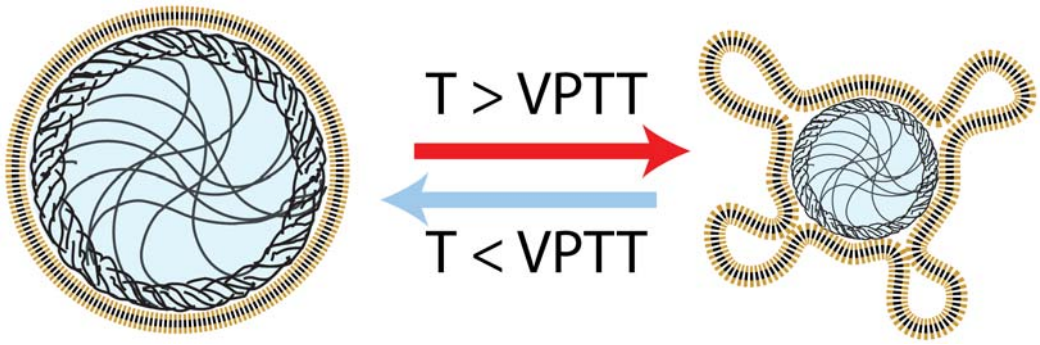

Figure 1-13: Image of a Lipogel undergoing the volume phase transition (VPT). The single lipid bilayer was shown to protrude off the microgel surface above the VPT temperature of 32°C, but remained impermeable. This was reproduced from the TOC image of Saleem et al.[104] with permission.

Chapter 3 will describe the use of bicelles to coat anionic microgels to make Bicellogels, a concept explained in Figure 1-14. This represents a novel way to coat soft surfaces with a single component lipid coating and provides an alternative to liposome fusion. Portions of this chapter and Chapter 6 will be submitted for publication, and the copyright will be transferred to the publisher at that time.

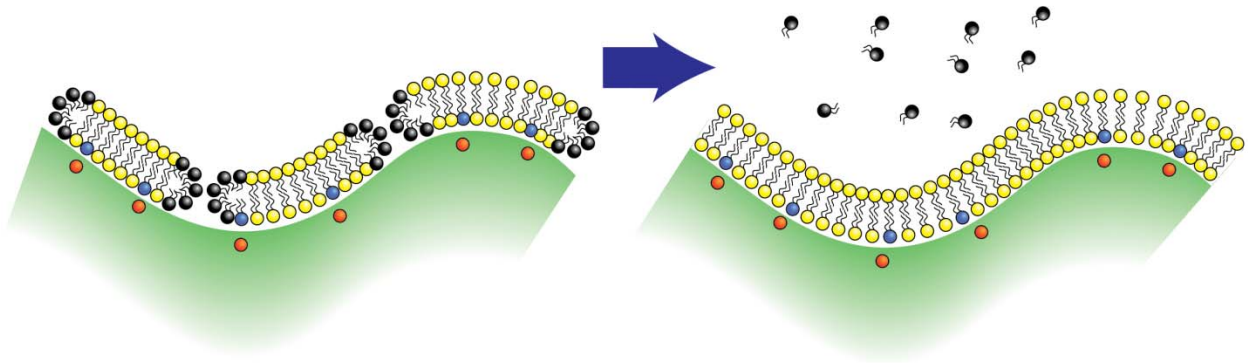

Figure 1-14: Image showing the use of bicelles to coat the surface of a pNIPAM microgel.

Chapter 4 will discuss the development of VESCOgels, which are lipid vesicle coated pNIPAM microgels. As Figure 1-15 illustrates, these liposome coated microgels show temporally tandem release of distinct cargo from both the liposomal and microgel matrix. Portions of this chapter and Chapter 6 are reproduced from a report published in 2013, with permission.[134]

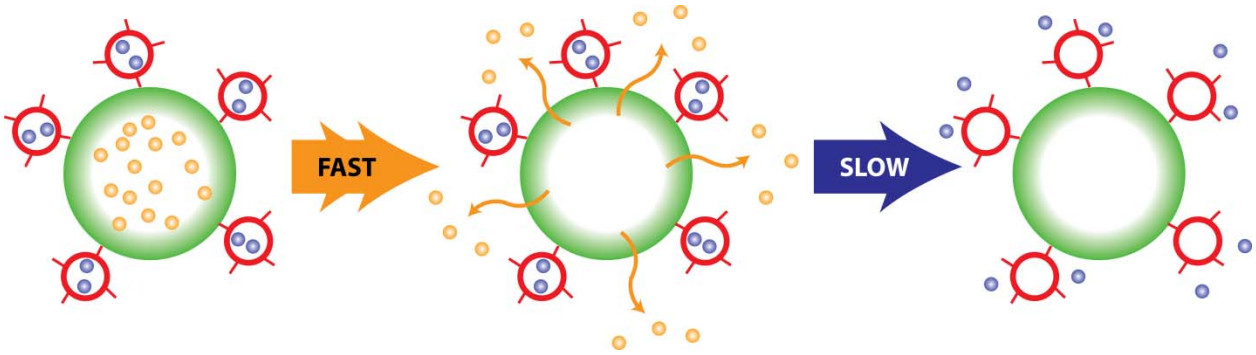

Figure 1-15: Image of a VESCOgel and its release properties. It was shown that intact vesicles (red) could be sequestered to the microgel surface (green) via carbodiimide chemistry. Also, the release profile for the contents trapped within the liposome and microgel was observed to be very different, effectively exhibiting temporally tandem release. This was reproduced from the TOC image of Saleem et al.[134] with permission.

1.4.2 Phospholipid lateral diffusion measurement via ^{31}P CODEX NMR

Chapter 5 will describe the use of the ^{31}P Centre-band Only Detection of EXchange (CODEX) experiment to measure the lateral diffusion coefficients of phospholipids in large

unilamellar vesicles, a concept illustrated in Figure 1-16. Portions of this chapter and Chapter 6 are reproduced from a report published in 2012, with permission.[135]

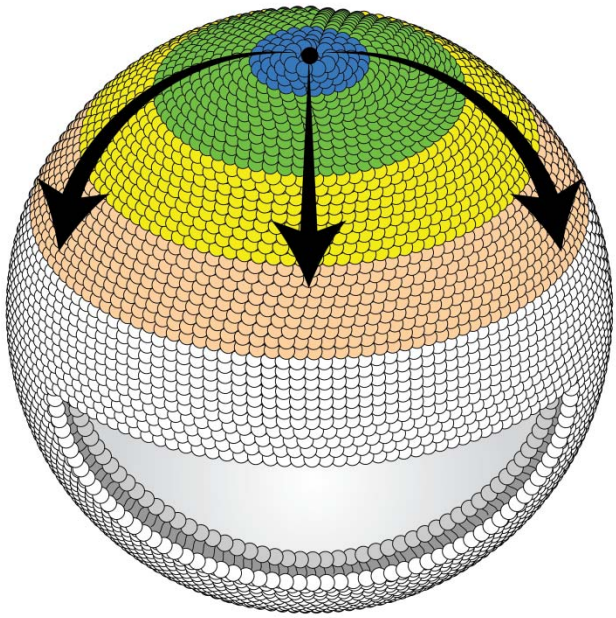

Figure 1-16: Image showing the potential loci available to a single lipid via lateral diffusion. This was reproduced from the TOC image of Saleem et al.[135] with permission.

1.5 References

(1) Israelachvili, J. N. In *Intermolecular and Surface Forces (Third Edition)*; Academic Press: San Diego, 2011; p. iii.

(2) Ma, C.; Srinivasan, M. P.; Waring, A. J.; Lehrer, R. I.; Longo, M. L.; Stroeve, P. *Colloids Surf. B Biointerfaces* **2003**, *28*, 319–329.

(3) Lenaz, G. *Biosci. Rep.* **1987**, *7*, 823–837.

(4) Axelrod, D. *J. Membr. Biol.* **1983**, *75*, 1–10.

(5) Vaz, W.; Goodsaidzalduondo, F.; Jacobson, K. *Febs Lett.* **1984**, *174*, 199–207.

(6) Jacobson, K.; Ishihara, A.; Inman, R. *Annu. Rev. Physiol.* **1987**, *49*, 163–175.

(7) Tocanne, J.; Dupoucezanne, L.; Lopez, A.; Tournier, J. *Febs Lett.* **1989**, *257*, 10–16.

(8) Tocanne, J.; Dupoucezanne, L.; Lopez, A. *Prog. Lipid Res.* **1994**, *33*, 203–237.

(9) Tocanne, J.; Cezanne, L.; Lopez, A.; Piknova, B.; Schram, V.; Tournier, J.; Welby, M. *Chem. Phys. Lipids* **1994**, *73*, 139–158.

(10) Seydel, J. K.; Coats, E. A.; Cordes, H. P.; Wiese, M. *Arch. Pharm. (Weinheim)* **1994**, *327*, 601–610.

(11) Golden, G. A.; Mason, P. E.; Rubin, R. T.; Mason, R. P. *Clin. Neuropharmacol.* **1998**, *21*, 181–189.

(12) Ferté, J. *Eur. J. Biochem.* **2000**, *267*, 277–294.

(13) Mason, R. P.; Jacob, R. F. *Circulation* **2003**, *107*, 2270–2273.

(14) Chew, C. F.; Guy, A.; Biggin, P. C. *Biophys. J.* **2008**, *95*, 5627–5636.

(15) Vauquelin, G.; Packeu, A. *Mol. Cell. Endocrinol.* **2009**, *311*, 1–10.

(16) Bangham, A. D.; Horne, R. W. *J. Mol. Biol.* **1964**, *8*, 660–IN10.

(17) Estes, D. J.; Mayer, M. *Biochim. Biophys. Acta BBA - Biomembr.* **2005**, *1712*, 152–160.

(18) Mayer, L. D.; Bally, M. B.; Hope, M. J.; Cullis, P. R. *Chem. Phys. Lipids* **1986**, *40*, 333–345.

(19) Lasic, D. D.; Papahadjopoulos, D. *Science* **1995**, *267*, 1275–1276.

(20) Ulrich, A. S. *Biosci. Rep.* **2002**, *22*, 129–150.

(21) Immordino, M. L.; Dosio, F.; Cattel, L. *Int. J. Nanomedicine* **2006**, *1*, 297–315.

(22) Liu, X.; Nakamura, C.; Yang, Q.; Kamo, N.; Miyake, J. *J. Chromatogr. A* **2002**, *961*, 113–118.

(23) Vold, R. R.; Prosser, R. S. *J. Magn. Reson. B* **1996**, *113*, 267–271.

(24) Macdonald, P. M.; Soong, R. *Can. J. Chem.* **2011**, *89*, 1021–1035.

(25) Triba, M. N.; Warschawski, D. E.; Devaux, P. F. *Biophys. J.* **2005**, *88*, 1887–1901.

(26) Dürr, U. H. N.; Gildenberg, M.; Ramamoorthy, A. *Chem. Rev.* **2012**, *112*, 6054–6074.

(27) Dürr, U. H. N.; Soong, R.; Ramamoorthy, A. *Prog. Nucl. Magn. Reson. Spectrosc.* **2013**, *69*, 1–22.

(28) Faham, S.; Bowie, J. U. *J. Mol. Biol.* **2002**, *316*, 1–6.

(29) Ujwal, R.; Bowie, J. U. *Methods* **2011**, *55*, 337–341.

(30) Johansson, L. C.; Wöhri, A. B.; Katona, G.; Engström, S.; Neutze, R. *Curr. Opin. Struct. Biol.* **2009**, *19*, 372–378.

(31) Zeineldin, R.; Last, J. A.; Slade, A. L.; Ista, L. K.; Bisong, P.; O'Brien, M. J.; Brueck, S. R. J.; Sasaki, D. Y.; Lopez, G. P. *Langmuir* **2006**, *22*, 8163–8168.

(32) Tabaei, S. R.; Jönsson, P.; Brändén, M.; Höök, F. *J. Struct. Biol.* **2009**, *168*, 200–206.

(33) Morigaki, K.; Kimura, S.; Okada, K.; Kawasaki, T.; Kawasaki, K. *Langmuir* **2012**, *28*, 9649–9655.

(34) Rodriguez, G.; Soria, G.; Coll, E.; Rubio, L.; Barbosa-Barros, L.; Lopez-Iglesias, C.; Planas, A. M.; Estelrich, J.; de la Maza, A.; Lopez, O. *Biophys. J.* **2010**, *99*, 480–488.

(35) Barbosa Barros, L.; Rodriguez, G.; Cócera Núñez, M.; Rubio, L.; Estelrich i Latràs, J.; Maza Ribera, A. de la; López Serrano, O. *Recent Adv. Pharm. Sci. II 2012 Ed. Diego Muñoz-Torrero Diego Haro Joan Vallès Chapter 8 P 135-149* **2012**.

(36) Brian, A. A.; McConnell, H. M. *Proc. Natl. Acad. Sci. U. S. A.* **1984**, *81*, 6159 –6163.

(37) Spinke, J.; Yang, J.; Wolf, H.; Liley, M.; Ringsdorf, H.; Knoll, W. *Biophys. J.* **1992**, *63*, 1667–1671.

(38) Goennenwein, S.; Tanaka, M.; Hu, B.; Moroder, L.; Sackmann, E. *Biophys. J.* **2003**, *85*, 646–655.

(39) Wagner, M. L.; Tamm, L. K. *Biophys. J.* **2000**, *79*, 1400–1414.

(40) Diaz, A. J.; Albertorio, F.; Daniel, S.; Cremer, P. S. *Langmuir* **2008**, *24*, 6820–6826.

(41) Albertorio, F.; Diaz, A. J.; Yang, T.; Chapa, V. A.; Kataoka, S.; Castellana, E. T.; Cremer, P. S. *Langmuir* **2005**, *21*, 7476–7482.

(42) Tanaka, M.; Sackmann, E. *Nature* **2005**, *437*, 656–663.

(43) Castellana, E. T.; Cremer, P. S. *ChemInform* **2007**, *38*, 429–444.

(44) Gao, K.; Huang, L. *Biochim. Biophys. Acta BBA - Biomembr.* **1987**, *897*, 377–383.

(45) Bayerl, T. M.; Bloom, M. *Biophys. J.* **1990**, *58*, 357–362.

(46) Carmona-Ribeiro, A. M.; Midmore, B. R. *Langmuir* **1992**, *8*, 801–806.

(47) Carmona-Ribeiro, A. M.; Herrington, T. M. *J. Colloid Interface Sci.* **1993**, *156*, 19–23.

(48) Troutier, A.; Véron, L.; Delair, T.; Pichot, C.; Ladavière, C. *Langmuir* **2005**, *21*, 9901–9910.

(49) Gopalakrishnan, G.; Rouiller, I.; Colman, D. R.; Lennox, R. B. *Langmuir* **2009**, *25*, 5455–5458.

(50) Osei-Asante, S.; Haratake, M.; Fuchigami, T.; Nakayama, M. *J. Bioact. Compat. Polym.* **2010**, *25*, 455–464.

(51) Gopalakrishnan, G.; Thostrup, P.; Rouiller, I.; Lucido, A. L.; Belkaïd, W.; Colman, D. R.; Lennox, R. B. *ACS Chem. Neurosci.* **2009**, *1*, 86–94.

(52) Lucido, A. L.; Gopalakrishnan, G.; Yam, P. T.; Colman, D. R.; Lennox, R. B. *ACS Chem. Neurosci.* **2010**, *1*, 535–541.

(53) Gopalakrishnan, G.; Yam, P. T.; Madwar, C.; Bostina, M.; Rouiller, I.; Colman, D. R.; Lennox, R. B. *ACS Chem Neurosci* **2011**, *2*, 700–704.

(54) Tanaka, M.; Tutus, M.; Kaufmann, S.; Rossetti, F. F.; Schneck, E.; Weiss, I. M. *J. Struct. Biol.* **2009**, *168*, 137–142.

(55) Liu, J.; Jiang, X.; Ashley, C.; Brinker, C. J. *J. Am. Chem. Soc.* **2009**, *131*, 7567–7569.

(56) Yang, Y.; Song, W.; Wang, A.; Zhu, P.; Fei, J.; Li, J. *Phys. Chem. Chem. Phys.* **2010**, *12*, 4418–4422.

(57) Cauda, V.; Engelke, H.; Sauer, A.; Arcizet, D.; Rädler, J.; Bein, T. *Nano Lett.* **2010**, *10*, 2484–2492.

(58) Veneziano, R.; Derrien, G.; Tan, S.; Brisson, A.; Devoisselle, J.-M.; Chopineau, J.; Charnay, C. *Small* **2012**, *8*, 3674–3682.

(59) Roggers, R. A.; Lin, V. S.-Y.; Trewyn, B. G. *Mol. Pharm.* **2012**, *9*, 2770–2777.

(60) Dengler, E. C.; Liu, J.; Kerwin, A.; Torres, S.; Olcott, C. M.; Bowman, B. N.; Armijo, L.; Gentry, K.; Wilkerson, J.; Wallace, J.; Jiang, X.; Carnes, E. C.; Brinker, C. J.; Milligan, E. D. *J. Controlled Release* **2013**, *168*, 209–224.

(61) Jin, T.; Pennefather, P.; Lee, P. I. *FEBS Lett.* **1996**, *397*, 70–74.

(62) Moya, S.; Donath, E.; Sukhorukov, G. B.; Auch, M.; Bäumler, H.; Lichtenfeld, H.; Möhwald, H. *Macromolecules* **2000**, *33*, 4538–4544.

(63) Moya, S.; Richter, W.; Leporatti, S.; Bäumler, H.; Donath, E. *Biomacromolecules* **2003**, *4*, 808–814.

(64) Campbell, A.; Taylor, P.; Cayre, O. J.; Paunov, V. N. *Chem. Commun.* **2004**, 2378.

(65) Angelatos, A. S.; Katagiri, K.; Caruso, F. *Soft Matter* **2006**, *2*, 18.

(66) Fischlechner, M.; Zaulig, M.; Meyer, S.; Estrela-Lopis, I.; Cuéllar, L.; Irigoyen, J.; Pescador, P.; Brumen, M.; Messner, P.; Moya, S.; Donath, E. *Soft Matter* **2008**, *4*, 2245.

(67) Bunge, A.; Fischlechner, M.; Loew, M.; Arbuzova, A.; Herrmann, A.; Huster, D. *Soft Matter* **2009**, *5*, 3331.

(68) Seki, K.; Tirrell, D. A. *Macromolecules* **1984**, *17*, 1692–1698.

(69) Takigawa, D. Y.; Tirrell, D. A. *Macromolecules* **1985**, *18*, 338–342.

(70) Devlin, B. P.; Tirrell, D. A. *Macromolecules* **1986**, *19*, 2465–2466.

(71) Ringsdorf, H.; Venzmer, J.; Winnik, F. M. *Angew. Chem. Int. Ed. Engl.* **1991**, *30*, 315–318.

(72) Wu, X. S.; Hoffman, A. S.; Yager, P. *Polymer* **1992**, *33*, 4659–4662.

(73) Ringsdorf, H.; Sackmann, E.; Simon, J.; Winnik, F. M. *Biochim. Biophys. Acta BBA - Biomembr.* **1993**, *1153*, 335–344.

(74) Simon, J.; Kühner, M.; Ringsdorf, H.; Sackmanna, E. *Chem. Phys. Lipids* **1995**, *76*, 241–258.

(75) Kim, J.; Bae, S. K.; Kim, J. *J. Biochem. (Tokyo)* **1997**, *121*, 15–19.

(76) Polozova, A.; Winnik, F. M. *Biochim. Biophys. Acta BBA-Biomembr.* **1997**, *1326*, 213–224.

(77) Franzin, C. M.; Macdonald, P. M.; Polozova, A.; Winnik, F. M. *Biochim. Biophys. Acta BBA-Biomembr.* **1998**, *1415*, 219–234.

(78) Tribet, C. *Biochimie* **1998**, *80*, 461–473.

(79) Meyer, O.; Papahadjopoulos, D.; Leroux, J. *FEBS Lett.* **1998**, *421*, 61–64.

(80) Kono, K.; Henmi, A.; Yamashita, H.; Hayashi, H.; Takagishi, T. *J. Controlled Release* **1999**, *59*, 63–75.

(81) Kim, J.; Kim, J. *Colloids Surf. B Biointerfaces* **2002**, *24*, 45–52.

(82) Wang, Y.; Winnik, F. M.; Clarke, R. J. *Biophys. Chem.* **2003**, *104*, 449–458.

(83) Hay, D. N. T.; Rickert, P. G.; Seifert, S.; Firestone, M. A. *J. Am. Chem. Soc.* **2004**, *126*, 2290–2291.

(84) Han, H. D.; Shin, B. C.; Choi, H. S. *Eur. J. Pharm. Biopharm.* **2006**, *62*, 110–116.

(85) Kiser, P. F.; Wilson, G.; Needham, D. *J. Controlled Release* **2000**, *68*, 9–22.

(86) De Geest, B. G.; Stubbe, B. G.; Jonas, A. M.; Van Thienen, T.; Hinrichs, W. L. J.; Demeester, J.; De Smedt, S. C. *Biomacromolecules* **2006**, *7*, 373–379.

(87) Pelton, R. H.; Chibante, P. *Colloids Surf.* **1986**, *20*, 247–256.

(88) Meng, Z.; Smith, M. H.; Lyon, L. A. *Colloid Polym. Sci.* **2009**, *287*, 277–285.

(89) Blackburn, W. H.; Lyon, L. A. *Colloid Polym. Sci.* **2008**, *286*, 563–569.

(90) Varga, I.; Gilanyi, T.; Meszaros, R.; Filipcsei, G.; Zrinyi, M. *J. Phys. Chem. B* **2001**, *105*, 9071–9076.

(91) Mcphee, W.; Tam, K.; Pelton, R. *J. Colloid Interface Sci.* **1993**, *156*, 24–30.

(92) Kang, S. C.; Choi, Y. J.; Kim, H. Z.; Kyong, J. B.; Kim, D. K. *Macromol. Res.* **2004**, *12*, 107–111.

(93) Hoare, T.; Pelton, R. *Curr. Opin. Colloid Interface Sci.* **2008**, *13*, 413–428.

(94) Hoare, T.; Pelton, R. *Macromolecules* **2004**, *37*, 2544–2550.

(95) Meunier, F.; Elaissari, A.; Pichot, C. *Polym. Adv. Technol.* **1995**, *6*, 489–496.

(96) Xu, J.; Timmons, A. B.; Pelton, R. *Colloid Polym. Sci.* **2004**, *282*, 256–263.

(97) Hu, X.; Tong, Z.; Lyon, L. A. *Colloid Polym. Sci.* **2011**, *289*, 333–339.

(98) Hoare, T.; Pelton, R. *Biomacromolecules* **2008**, *9*, 733–740.

(99) Meng, Z.; Hendrickson, G. R.; Lyon, L. A. *Macromolecules* **2009**, *42*, 7664–7669.

(100) Hoare, T.; McLean, D. *J. Phys. Chem. B* **2006**, *110*, 20327–20336.

(101) Jones, C. D.; Lyon, L. A. *Macromolecules* **2000**, *33*, 8301–8306.

(102) Jones, C.; Lyon, A. *Macromolecules* **2003**, *36*, 1988–1993.

(103) MacKinnon, N.; Guérin, G.; Liu, B.; Gradinaru, C. C.; Rubinstein, J. L.; Macdonald, P. M. *Langmuir* **2010**, *26*, 1081–1089.

(104) Saleem, Q.; Liu, B.; Gradinaru, C. C.; Macdonald, P. M. *Biomacromolecules* **2011**, *12*, 2364–2374.

(105) Kühner, M.; Tampé, R.; Sackmann, E. *Biophys. J.* **1994**, *67*, 217.

(106) Cassier, T.; Sinner, A.; Offenhäuser, A.; Möhwald, H. *Colloids Surf. B Biointerfaces* **1999**, *15*, 215–225.

(107) Kügler, R.; Knoll, W. *Bioelectrochemistry* **2002**, *56*, 175–178.

(108) Helwa, Y.; Dave, N.; Liu, J. *Soft Matter* **2013**.

(109) Städler, B.; Chandrawati, R.; Goldie, K.; Caruso, F. *Langmuir* **2009**, *25*, 6725–6732.

(110) MacKinnon, N.; Guérin, G.; Liu, B.; Gradinaru, C. C.; Macdonald, P. M. *Langmuir* **2009**, *25*, 9413–9423.

(111) El-Hamed, F.; Dave, N.; Liu, J. *Nanotechnology* **2011**, *22*, 494011.

(112) Majewski, J.; Wong, J. Y.; Park, C. K.; Seitz, M.; Israelachvili, J. N.; Smith, G. S. *Biophys. J.* **1998**, *75*, 2363–2367.

(113) Ng, C. C.; Cheng, Y.-L.; Pennefather, P. S. *Macromolecules* **2001**, *34*, 5759–5765.

(114) Katagiri, K.; Caruso, F. *Adv. Mater.* **2005**, *17*, 738–743.

(115) Lee, D.-C.; Chang, B.-J.; Yu, L.; Frey, S. L.; Lee, K. Y. C.; Patchipulusu, S.; Hall, C. *Langmuir* **2004**, *20*, 11297–11300.

(116) Kazakov, S.; Kaholek, M.; Teraoka, I.; Levon, K. *Macromolecules* **2002**, *35*, 1911–1920.

(117) Kazakov, S.; Kaholek, M.; Kudasheva, D.; Teraoka, I.; Cowman, M. K.; Levon, K. *Langmuir* **2003**, *19*, 8086–8093.

(118) Schillemans, J. P.; Flesch, F. M.; Hennink, W. E.; van Nostrum, C. F. *Macromolecules* **2006**, *39*, 5885–5890.

(119) An, S. Y.; Bui, M.-P. N.; Nam, Y. J.; Han, K. N.; Li, C. A.; Choo, J.; Lee, E. K.; Katoh, S.; Kumada, Y.; Seong, G. H. *J. Colloid Interface Sci.* **2009**, *331*, 98–103.

(120) Hong, J. S.; Stavis, S. M.; DePaoli Lacerda, S. H.; Locascio, L. E.; Raghavan, S. R.; Gaitan, M. *Langmuir* **2010**, *26*, 11581–11588.

(121) Jesorka, A.; Markström, M.; Karlsson, M.; Orwar, O. *J. Phys. Chem. B* **2005**, *109*, 14759–14763.

(122) Laws, D. D.; Bitter, H.-M. L.; Jerschow, A. *Angew. Chem. Int. Ed.* **2002**, *41*, 3096–3129.

(123) Duer, M. J. *Solid-state NMR spectroscopy principles and applications*; Blackwell Science: Oxford, 2002.

(124) Saitô, H.; Ando, I.; Naito, A. *Solid State NMR Spectroscopy for Biopolymers*; Springer Netherlands, 2006.

(125) Levitt, M. H. *Spin dynamics: basics of nuclear magnetic resonance*; John Wiley & Sons: Chichester, England; Hoboken, NJ, 2008.

(126) Keeler, J. *Understanding NMR spectroscopy*; Wiley: Chichester, 2010.

(127) Lakowicz, J. R. *Principles of fluorescence spectroscopy*; 3rd ed.; Springer: New York, N.Y., 2006.

(128) Sauer, M.; Hofkens, J.; Enderlein, J. *Handbook of fluorescence spectroscopy and imaging: from single molecules to ensembles*; 1st ed.; Wiley-VCH: Weinheim, Germany, 2011.

(129) Penzkofer, A.; Lu, Y. *Chem. Phys.* **1986**, *103*, 399–405.

(130) Andersson, A.; Danielsson, J.; Gräslund, A.; Mäler, L. *Eur. Biophys. J.* **2007**, *36*, 621–635.

(131) This nomenclature was first coined by Dr. Klaus Eichele and presented on his webpage: Chemical Shift Tensor Conventions http://anorganik.uni-tuebingen.de/klaus/nmr/index.php?p=conventions/csa/csa#6.

(132) Meneses, P.; Glonek, T. *J. Lipid Res.* **1988**, *29*, 679–689.

(133) Nishiyama, Y.; Endo, Y.; Nemoto, T. In *110 kHz MAS*; Miami. FL.

(134) Saleem, Q.; Zhang, Z.; Gradinaru, C. C.; Macdonald, P. M. *Langmuir* **2013**.

(135) Saleem, Q.; Lai, A.; Morales, H. H.; Macdonald, P. M. *Chem. Phys. Lipids* **2012**, *165*, 721–730.

Lipogels: Single-Lipid-Bilayer-Enclosed Hydrogel Spheres

2.1 Introduction

An enduring challenge in the field of spherically supported membrane fabrication has been to produce, efficiently and in high yield, monodisperse polymer microgels enclosed by a single continuous lipid bilayer. In the particular case of pNIPAM, although interactions between lipid vesicles and linear pNIPAM have been investigated relatively thoroughly,[1–13] pNIPAM microgels as potential spherical polymer supports for lipid bilayers have received less attention.[14–16] In particular, the goal of obtaining a single, continuous, non-leaky lipid bilayer enclosure has proved to be elusive.[14,15]

In this chapter, a simple, efficient method for fabricating monodisperse, thermoresponsive pNIPAM microgels enclosed by a single, continuous, impermeable lipid bilayer is reported. Chujo et al.[17] coined the term Lipogel to describe bulk non-ionic gels with copolymerized long alkyl groups. However, Lipogel used here is in the sense employed by Bures et al., that is, "a hydrogel anchored lipid vesicle system".[18] The polymer microgel consists of a core of lightly cross-linked pNIPAM wrapped in a shell of more highly cross-linked p(NIPAM-co-acrylic acid (AA)). The higher cross-linking density of the shell provides a smooth surface onto which lipids may assemble into a bilayer structure, whereas the AA units of the shell provide surface sites for hydrophobic modifications that encourage lipid association. The lipid bilayer is composed of 1-palmitoyl-2-oleoyl-phosphatidylcholine (POPC), a phospholipid representative of naturally occurring membrane lipids and which remains liquid crystalline, that is, fluid, over a wide temperature range thus facilitating assembly of the lipid bilayer. Lipogels were fabricated by a simple freeze–thaw cycling of an aqueous mixture of preformed POPC liposomes and hydrophobically modified (HM) microgels. Using a combination of NMR and fluorescence

spectroscopies and fluorescence imaging techniques, we demonstrate that the Lipogels so formed are enclosed by a lipid bilayer that is unilamellar, impermeable, and surrounds continuously the entire microgel, whereas the microgel itself retains the essential thermoresponsive behavior of pNIPAM.

2.2 Materials and Methods

2.2.1 Materials

N-Isopropylacrylamide (NIPAM), methylene bis(acrylamide) (MBA), acrylic acid (AA), potassium persulfate (KPS), tetradecylamine (hydrophobe), O-(6-Chlorobenzotriazol-1-yl)-N,N,N',N'-tetramethyluronium tetrafluoroborate (TCTU), N,N'-diisopropylethylamine (DIPEA), Triton X-100 (Triton), ethylenediaminetetraacetic acid (EDTA), sodium hydrosulfite (sodium dithionite), calcein, carboxyfluorescein (CF), fluorescein O-acrylate (FA), and rhodamine 6G (R6G) were obtained from Sigma Aldrich Canada (Oakville, ON). 1-Palmitoyl-2-oleoyl-*sn*-glycero-3-phosphocholine (POPC) and 1,2-dioleoyl-*sn*-glycero-3-phosphoethanolamine-N-(7-nitro-2–1,3-benzoxadiazol-4-yl) (ammonium salt) (NBD-PE) were purchased from Avanti Polar Lipids (Alabaster, AL). Lissamine rhodamine B 1,2-dihexadecanoyl-*sn*-glycero-3-phosphoethanolamine (triethylammonium salt) (RhB-PE) was purchased from Invitrogen (Carlsbad, CA). Cellulose dialysis tubing with a cutoff of 12 000–14 000 MW was obtained from VWR Scientific (Mississauga, ON). All NMR spectra were recorded in deuterated methanol (MeOD) from Sigma Aldrich Canada (Oakville, ON) and referenced to the methyl peak. NIPAM was recrystallized from hexanes prior to use. All other chemicals were used as received. Milli-Q water was used in all instances.

2.2.2 Synthesis of pNIPAM/p(NIPAM-co-AA) Core–Shell Microgels

pNIPAM/p(NIPAM-co-AA) core–shell microgels were synthesized by a temperature-programmed one-pot, two-step procedure, amalgamating the methods of Meng et al.[19] and MacKinnon et al.[14] In brief, in the first step, NIPAM (16 mmol, 1.8 g) and BA (0.4 mmol, 0.06 g) were dissolved in 125 mL of boiled water and added to a 500 mL, three-necked round-bottomed flask equipped with a condenser, a thermometer, a N_2 gas line, and an overhead stirrer. The temperature was controlled by a heating mantle mounted on a height-adjustable platform. The solution was bubbled with N_2 for 40 min while being stirred at 200 rpm at a temperature of 45 °C. KPS (0.12 g (0.4 mmol) dissolved in 4 mL of cold water) was added to initiate polymerization. Once opalescence appeared, the N_2 purge was removed, the temperature was ramped up to 65 °C over the course of 40 min, the stirring speed was reduced to 100 rpm, and polymerization was allowed to proceed for a further 6 h.

In the second step, the core microgels were passed through glass wool while hot and returned back to the cleaned round-bottomed flask. NIPAM (7 mmol, 0.8 g), MBA (1.8 mmol, 0.28 g), and AA (2 mmol, 0.15 mL) were dissolved in 80 mL of boiling water and added to the core microgel suspension at 50 °C while stirring at 200 rpm. After 1 min, the stirring speed was decreased to 100 rpm, and the mixture was allowed to reach 60 °C, at which point a further increment of KPS (0.03 g [0.1 mmol] dissolved in 1 mL of cold water) was added. Step-two polymerization was allowed to continue for 12 h at a temperature of 65 °C.

Once polymerization was complete, the hot microgel suspension was passed through glass wool to remove coagulum, cooled to room temperature, poured in dialysis tubing, and dialyzed against water for at least 1 week with daily changes of water. The dialyzed microgel suspension was stored at 4 °C.

2.2.3 Quantitation of AA incorporation

The level of AA incorporation was determined via potentiometric titration of a known weight of microgel. Typically, 60 mg of dialyzed microgel was suspended in 50 mL of 100 mM KCl, and the solution was bubbled with N_2 and stirred until the pH was constant, at which point the titration commenced with addition of aliquots of 0.1 M NaOH under conditions of constant stirring.

2.2.4 Microgel Size Measurement

The size and polydispersity index (PDI) of the microgels was determined via dynamic light scattering (DLS) using a Zetasizer 3000HS (Malvern) in photon correlation spectroscopy (PCS) mode with a 90° detector angle. A sample containing 0.5 mg of microgel in 2 mL of 100 mM KCl, 10 mM TRIS, and filtered buffer (pH 7.2) was used. Each sample was subjected to 10 measurements at 25 °C, and the volume-weighted peak average was determined.

2.2.5 Synthesis of p(NIPAM-co-FA)/p(NIPAM-co-AA) Core–Shell Microgels

In the instance that it was desired to fluorescently label the microgel core, fluorescein *O*-acrylate (FA) was added in step one at level of 0.02 mol % of FA relative to NIPAM (3 μmol, 1.2 mg) to create p(NIPAM-co-FA)/p(NIPAM-co-AA) core–shell microgels. Otherwise, the microgel synthesis was unchanged.

2.2.6 R6G Modification of p(NIPAM-co-FA)/p(NIPAM-co-AA) Microgels

To label fluorescently the microgel shell region specifically, we targeted the AA carboxyl groups for modification with the fluorophore R6G. About 20 mg of dialyzed p(NIPAM-co-

FA)/p(NIPAM-co-AA) microgel was centrifuged and re-suspended in 1 mL of DMF three times. About 0.1 mg of TCTU was added, along with 20 µL of DIPEA, and the mixture was stirred for 8 min. We then added 50 µL of a 3 µM solution of R6G in DMF, and the suspension was stirred for 18 h at room temperature. The R6G-modified microgels were washed at least six times with DMF, a process involving cycles of centrifugation at 8000 rpm for 5 min, re-suspension, and sonication. The resulting suspension was washed a further five times with water by a similar process of centrifugation at 4000 rpm for 5 min and re-suspension. Finally, the R6G-modified microgels were suspended in 100 mM KCl and 10 mM TRIS (pH 7.2) buffer (hereafter referred to as “tris buffer”).

2.2.7 Hydrophobic Modification of Shell in pNIPAM/p(NIPAM-co-AA) Microgels

AA residues in the shell of the core–shell microgels were modified with hydrophobes as outlined in Figure 2-1. Typically, 60 mg of dialyzed microgels was centrifuged and re-suspended in 3 mL of ethanol three times, then sonicated for 10 min in a bath sonicator. TCTU (20 mg) was added to the microgel solution, and the mixture was stirred for 20 min. We next dissolved 40 mg of tetradecylamine in 1.0 mL of ethanol, and the mixture was allowed to react for 18 h at room temperature. The resulting hydrophobically modified (HM) microgels were separated from excess reactant materials and side products by washing at least three times with methanol (via centrifugation at 8000 rpm for 5 min and re-suspension), then sonicating for 10 min in a bath sonicator and, finally, washing two more times with methanol as before. The methanol was exchanged for water by first centrifuging the HM microgels and adding back water, drop-by-drop, while sonicating. The resulting suspension was further washed with water

at least three times via centrifugation, followed by re-suspension. The hydrophobically modified microgels (HM microgels) were then stored at 4 °C for future use.

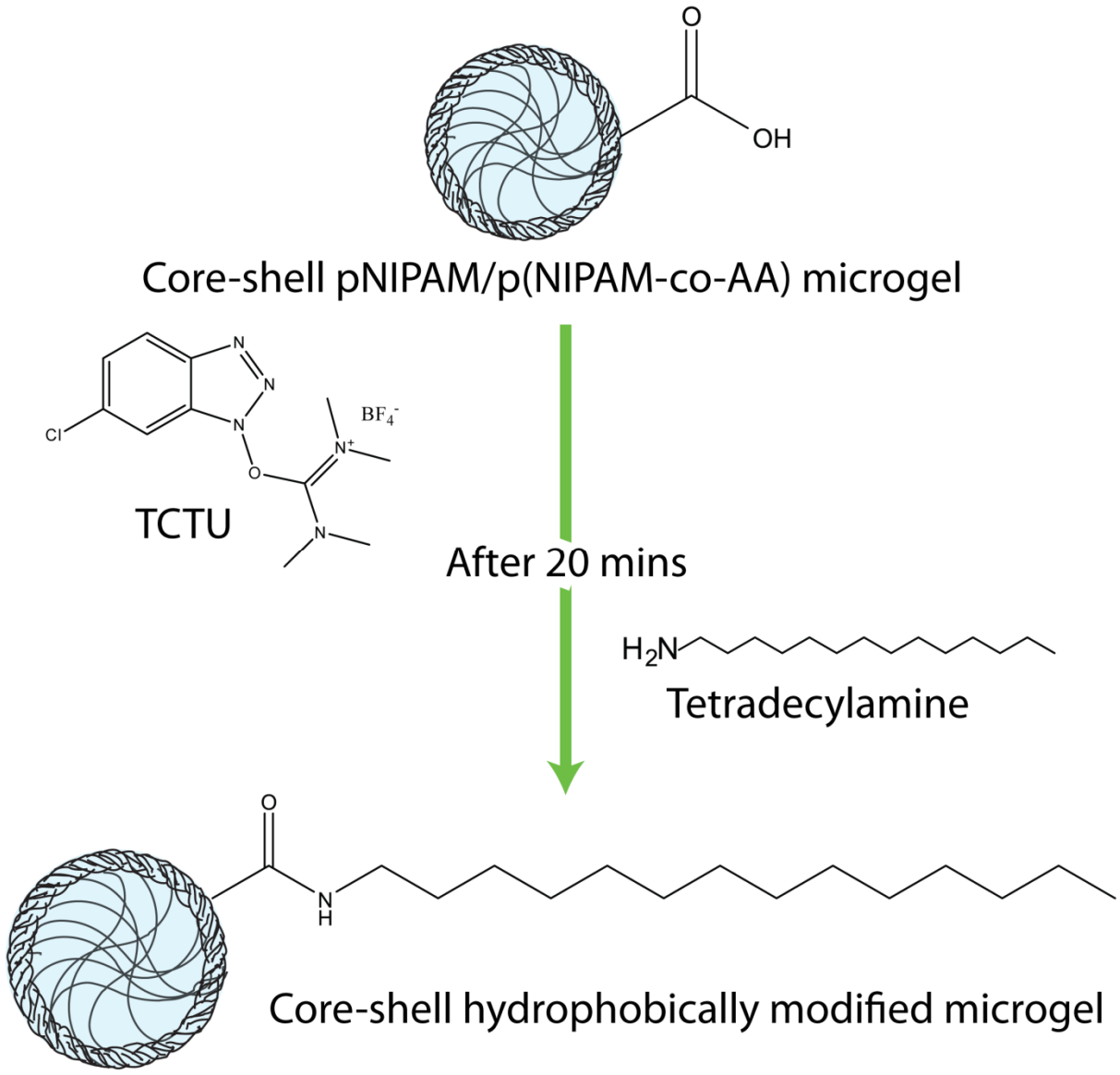

Figure 2-1: Hydrophobic Modification of Microgels.

Hydrophobe incorporation was determined using ^{13}C NMR, as described below. The concentration of the HM microgels in aqueous suspension was determined gravimetrically.

Aliquots of this stock solution were re-suspended in appropriate buffer solutions prior to their use.

2.2.8 Lipid Bilayer Coating of HM pNIPAM/p(NIPAM-co-AA) Core–Shell Microgels

Lipid-bilayer-coated HM pNIPAM/p(NIPAM-co-AA) core–shell microgels, hereafter referred to as Lipogels, were prepared as per Figure 2-2. In brief, 20 mg of POPC was dissolved in 244 uL of 108 µM NBD-PE (0.1 mol %) or 176 uL of 0.075 µM RhB-PE (0.05 mol %) stock chloroform solutions. The chloroform was removed under a stream of N_2 gas to create a lipid film. After 24 h under vacuum to eliminate final traces of solvent, the dry lipid film was hydrated with the appropriate buffer to a total lipid concentration of 20 mg mL^{-1}. After three cycles of freeze–thaw–vortex, the resulting LMVs were converted to LUVs via extrusion involving 25 passages through a 0.1 µm polycarbonate membrane installed in a mini-extruder from Avanti Polar Lipids (Alabaster, AL).

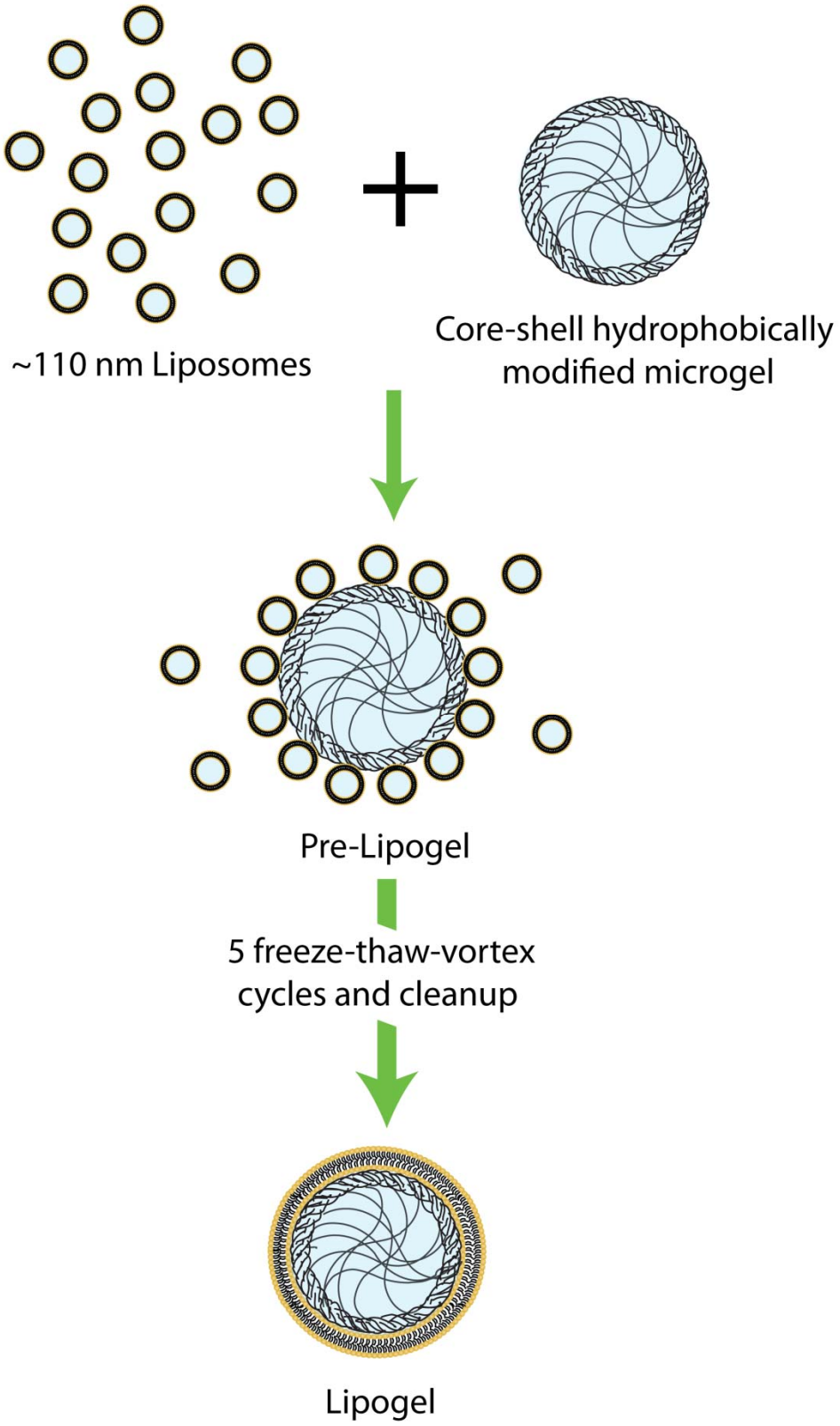

Figure 2-2: Fabrication of Lipogels from Hydrophobically Modified Microgels and Liposomes

LUV binding to HM microgels was achieved by simply mixing 2 mg of HM microgels with 4 mg of LUV dispersed together in 1 mL of tris buffer in a 1.5 mL vial. The LUV–HM microgel suspension was then stirred gently for 2 h. To convert the bound LUVs into a single bilayer coating the HM microgels, the suspension was subjected to five freeze–thaw–vortex cycles using liquid N_2 and a room-temperature water bath. Unbound LUVs were removed by repeatedly centrifuging the microgels at 4000 rpm for 5 min and re-suspending the microgel pellet in the same buffer.

2.2.9 Lamellarity of Lipogels

To determine the number of lipid bilayers coating individual Lipogels, we employed the sodium dithionite fluorescence quenching assay described by McIntyre and Sleight.[20] Dithionite ion quenches the fluorescence of NBD-PE but does not permeate the lipid bilayer at room temperature. Therefore, 50% quenching indicates a single lipid bilayer coating. In a typical assay, 0.1 mg of Lipogels, fabricated using liposomes containing 0.1 mol % NBD-PE, was suspended in 2 mL of tris buffer and placed in a 4 mL quartz cuvette. The NBD-PE fluorescence of this sample was excited at 470 nm, and the resulting emission at 530 nm was monitored every second in a QuantaMaster PTI spectrofluorimeter (Photon Technology International, Lawrenceville, NJ). After an initial baseline was established, the measurement was paused, and 20 µL of freshly made 1 M sodium dithionite in 1 M Tris (pH 10) was added and mixed before the measurement was resumed. After a new baseline was established, the measurement was paused again and 20 µL of 5% Triton solution was added to disrupt completely the lipid bilayer integrity before measurement was resumed.

2.2.10 Volume Phase Transition Temperature Determination

The VPT temperature (VPTT) was determined via fluorescence spectroscopy of various FA-containing microgels. Typically, 1 mg/mL of microgels suspended in tris buffer was transferred to a 1 mL quartz cuvette and placed in a Fluoromax 4 spectrofluorometer (Horiba Scientific) fitted with a Peltier temperature controller. Fluorescence was excited at 490 nm, and emission was recorded at 520 nm over a temperature range from 25 to 40 °C at increments of 1 °C with 2 min of equilibration time at each temperature prior to acquisition. At each temperature, we corrected the emission spectrum by subtracting the contribution of the tris buffer. The intensity recorded at a given temperature, *I(T)*, was normalized according to the following equation:

$$F(T) = \frac{I(T) - I_{min}}{I_{max} - I_{min}} \qquad \text{Equation 15}$$

where I_{min} and I_{max} are the extremes of intensity across the range of temperatures.

2.2.11 Bilayer Integrity of Lipogels at T > VPTT

Control experiments on LUVs demonstrated that dithionite permeation of lipid bilayers became significant at temperatures greatly elevated above room temperature. Thus, the dithionite quenching assay could not be used to investigate the integrity of the Lipogel lipid bilayer at temperatures above that of the VPTT. Instead, an assay was developed based on de-quenching by EDTA of a quenched cobalt–calcein complex, the latter consisting of 50 mM calcein plus 50 mM $CoCl_2$ in 25 mM KCl, 10 mM Tris buffer (pH 7.2). The cobalt–calcein complex was trapped inside Lipogels by the addition of an aliquot of the complex solution to a

suspension of LUV-HM microgel complexes, which were then subjected to the freeze–thaw–vortex cycles that fuse the LUVs into a single lipid bilayer. Unbound LUVs and free dye were removed by five cycles of centrifugation/cleaning with 100 mM KCl and 10 mM Tris buffer (pH 8.0).

Calcein fluorescence was excited at 490 nm, and its emission was monitored at 515 nm using the same QuantaMaster PTI spectrofluorimeter as that in the lamellarity assay. A 2 µL aliquot of a 1 M EDTA, 500 mM Tris (pH 8.35) solution was added to a sample of Lipogels containing entrapped cobalt–calcein complex, and the calcein fluorescence was measured after allowing for several minutes of equilibration. The sample was then warmed to 40 °C in a water bath for 20 min and allowed to re-equilibrate to room temperature, and the calcein fluorescence was re-measured. Finally, 20 µL of 5% Triton solution was added to destroy the lipid bilayers, and the fluorescence was measured again.

2.2.12 Fluorescence Microscopy

We prepared samples for microscopy by adding an aliquot of suspension onto plasma-cleaned coverslips. These were incubated for 10 min at room temperature and then washed with buffer to remove all non-absorbed material.

Fluorescence images were obtained using a custom-built, inverted wide-field microscope, technical details of which have been described in full elsewhere.[21] In brief, two diode-pumped solid-state lasers were used to excite coverslip-mounted samples at 532 nm (NT56-485, Edmund Optics, USA) and at 473 nm (Cobolt Blues, Cobolt, Sweden) through a high NA objective (plan-apochromat 1.45 NA/60×, Olympus, USA). Emitted fluorescence light was collected by the same objective and passed through bandpass optical filters to remove

scattering and cross-talk contributions. Fluorescence images were captured with a highly sensitive, cooled electron-multiplied charge-coupled device (EMCCD, DU-897BV, Andor, USA). Typical frames were obtained from an area of 65 × 65 μm^2 of the sample upon exposure to continuous laser illumination for 100 ms.

All fluorescence images were prepared in ImageJ.[22] Raw images were first de-convoluted using a 2D iterative algorithm. We obtained the point spread function used by imaging a single 24 nm diameter fluorescent latex bead (Invitrogen) under similar experimental conditions. The "Align Stacks" plugin (J. Parker, Align3_TP) was used to overlap images that were then merged into a single composite with controllable artificial red and green channels, if needed. The color balance was adjusted so that both entities of interest in both channels were clear. The final images were cropped and resized to the desired image size.

To image the effects of the VPTT on Lipogel morphology, we fabricated Lipogels using either RhB-PE-containing LUVs to label the lipid bilayer or LUV-encapsulated CF to label the core region of the microgel. The latter liposomes were prepared in the presence of 50 mM CF and 10 mM Tris (pH 7.0) with free CF being removed subsequent to extrusion by passage through Sephadex G-50.

2.2.13 FRAP Study of Lipogel Lipid Bilayers

Lipogels for fluorescence recovery after photobleaching (FRAP) experiments were fabricated using liposomes containing 0.1 mol % NBD-PE and prepared for imaging, as described above. FRAP experiments were carried out on a custom-built confocal microscope, the technical details of which are described in full elsewhere.[21] In brief, a 480 nm excitation was achieved by frequency doubling the output of a femtosecond laser (Tsunami HP, Spectra

Physics, Santa Clara, CA). The laser excited the sample at intensities of 1–100 W/cm^2 upon focusing by a high NA objective (1.4/100× plan-apochromat, Carl Zeiss, Canada) to a diffraction-limited spot. The emitted light was collected by the same objective and passed through a 50 µm pinhole and long-pass optical filters to remove out-of-focus fluorescence and scattering contributions. The fluorescence was focused onto a photon-counting detector (PD5CTC, Optoelectronic Components, Kirkland, Canada), which was read and digitized by a multichannel time-correlated counting module (PicoHarp300, PicoQuant, Germany).

Upon scanning a large area with several surface-immobilized Lipogels using low excitation intensity (ca. 1 W/cm^2), a single Lipogel was selected and imaged at high resolution. A spot on the edge of the Lipogel was then instantly illuminated at high laser intensity (ca. 100 W/cm^2) for 1 s. Using low excitation intensity (1.05 W/cm^2) again, the bleached spot was then probed for up to 15 min to obtain the fluorescence recovery curve, or, alternatively, fast area scanning was employed to obtain a series of recovery images of the entire Lipogel. Typically, a minimum of five individual Lipogels were interrogated in either fashion.

FRAP numerical simulations are described in detail in Appendix A. In brief, 50,000 fluorophores are uniformly distributed on the surface of a 1.3 µm diameter sphere and allowed to undergo 2-D random walks. As a result of the photobleaching pulse, some fluorophores are selectively photobleached (discarded) based on the illumination intensity at their respective positions. The simulation parameters were chosen to match closely the simulated confocal image immediately after the photobleaching pulse to its experimental counterpart. The contribution of each fluorophore to the total signal depends on the detection efficiency profile CEF(x,y,z) of the confocal setup approximated to a 3-D Gaussian.[23,24] Each time step, after all active fluorophores move to new positions, the fluorescence signal is obtained by summing up

all CEF(x,y,z) values. The simulated recovery curves were normalized to the calculated signal before photobleaching and fitted to a bi-exponential model function. (See Appendix A.)

2.2.14 NMR Spectroscopy

^{13}C NMR spectra were acquired on a Varian Inova 500 MHz switchable broadband liquids probe at 20 °C using a single pulse excitation of 12.5 μs duration with SPINAL-64 ^{1}H decoupling (decoupler field strength of 6 kHz) during acquisition at a sweep width of 50 kHz and 40k data size. Typically, 12,000 transients were collected, and line broadening of 20 Hz was applied prior to Fourier transformation. (See Appendix A.)

2.3 Results and Discussion

2.3.1 Synthesis and Characterization of HM pNIPAM/p(NIPAM-co-AA) Microgels

Our ultimate goal being to produce a spherical polymer supported lipid bilayer, the spherical polymer support needs to possess certain specific properties. First, a diameter on the order of 1 μm would be optimal because anything smaller would approach the diffraction limit for optical imaging, whereas anything larger would compromise the surface filling factor for NMR spectroscopic studies of the membrane components. Second, the surface of the spherical polymer support would need to be amenable to being functionalized with moieties that encourage lipid adsorption. Third, the surface would need to be sufficiently smooth that a defect-free lipid bilayer could assemble.

For such purposes, conventional one-step procedures for pNIPAM microgel synthesis are problematic. Specifically, a one-step synthesis produces microgels having a radial cross-

linking density gradient, with the number of cross-links decreasing from the center to the periphery,[25] yielding "hairy" microgels with dangling polymer chains at the surface. The consequently rough surface interferes with the formation of a continuous, impermeable lipid bilayer enclosing the entire microgel. Furthermore, functional group distribution is difficult to control in a one-step synthesis because it depends heavily on the particular properties of a given functional group.[26]

Consequently, we adopted a two-step synthetic protocol in which, during the first step, a lightly cross-linked pNIPAM core is formed, whereas during the second step, a more highly cross-linked pNIPAM-co-AA shell is added. The result, therefore, should be a relatively smooth outer surface or shell, with AA functional groups isolated at or near the periphery, overlaying a pNIPAM core that undergoes a normal VPT characteristic of pNIPAM.

DLS showed that the core–shell pNIPAM/p(NIPAM-co-AA) microgels synthesized with the two-step protocol described in the Materials and Methods section were 1.33 μm in diameter at pH 7.0 and slightly smaller in diameter (1.28 μm) at pH 2.5, presumably due to protonation of AA carboxyls and a corresponding decrease in Coulombic repulsion. PDIs measured via DLS were < 0.15, indicative of a highly monodisperse microgel size distribution. It is interesting to note that Meng et al.[19] reported p(NIPAM-co-AA) microgels with diameters upward of 2.5 μm at pH 3 using a one-step temperature-programmed synthesis. With our two-step protocol, despite experimenting with multiple formulations and reaction conditions, only core–shell spheres of maximum 1.33 μm diameter could be produced. It is known that the shell compresses the core in seeded polymerizations of pNIPAM-based microgels.[27] It is also known that when loosely cross-linked core particles are used, the core and core–shell particle sizes are

essentially identical.[28] However, in our formulations, where the shell is far more heavily cross-linked that the core, compression of the shell by the core may be more pronounced.

To confirm the presence of a core–shell morphology, we produced R6G-modified p(NIPAM-co-FA)/p(NIPAM-co-AA) core–shell microgels in which FA is confined to the core region, whereas R6G is segregated to the AA-containing regions. This permits independent excitation of the FA-containing core at 473 nm versus excitation of the R6G-containing region at 532 nm for fluorescence microscopy purposes. Figure 2-3A shows overlain images of the identical microgels, obtained separately and in quick succession, using 473 and 532 nm excitation, to map the distribution of FA and R6G, respectively. The core–shell morphology is clearly evident. Figure 2-3B shows the fluorescence intensity at the two excitation wavelengths along a line segment directed through the center of a single microgel. The microgel exhibits a distinct core (green) region that is enveloped by a shell (red). The separation between the maxima in the shell (red) if taken to correspond to the diameter of the microgel, being on the order of 1.3 μm, is in agreement with DLS measurements. However, the core diameter determined from such images might not be correct because the dimensions fall at or below the diffraction limit. Furthermore, potential issues of FA radial distribution gradients, depletion before the completion of the core synthesis step, or both further complicate determination of the core size from such images.

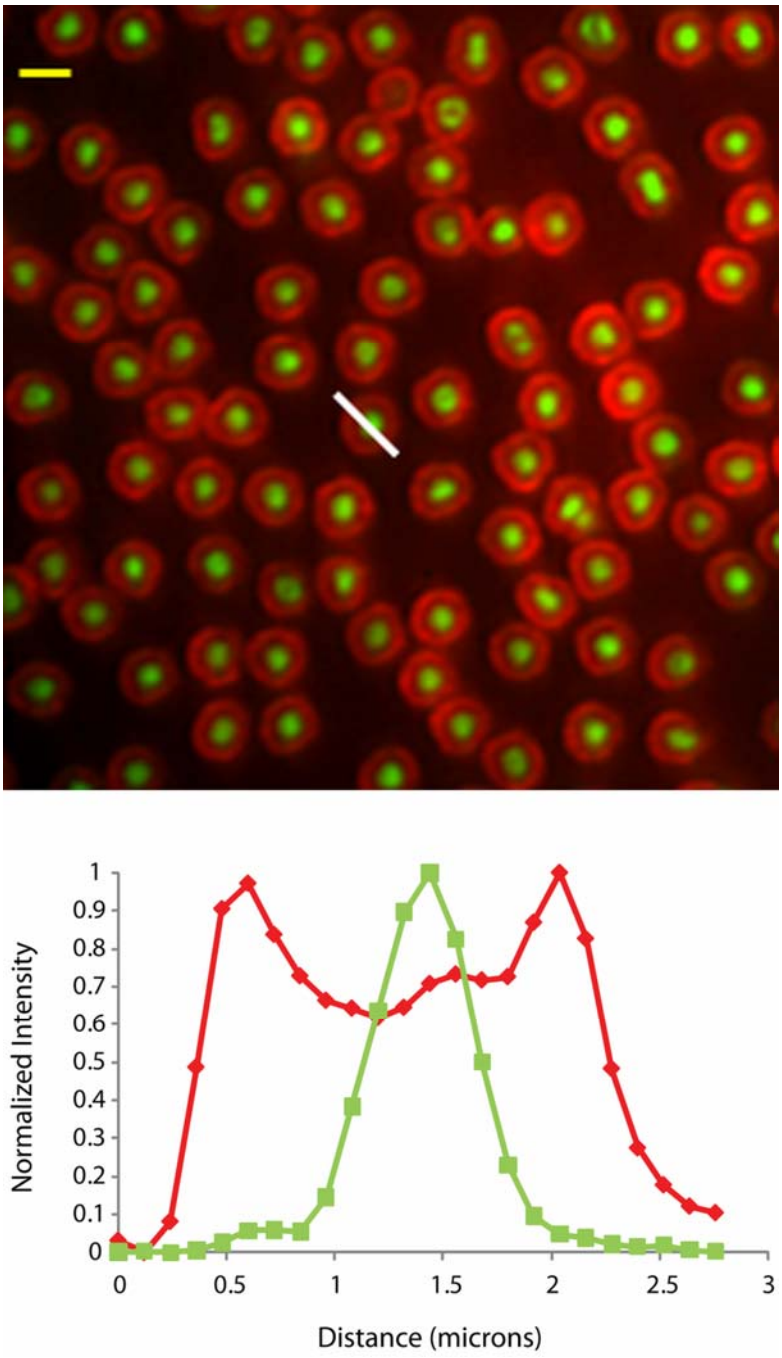

Figure 2-3: R6G-modified p(NIPAM-co-FA)/p(NIPAM-co-AA) core–shell microgels. (A) Merged fluorescence images of core–shell microgels. The green image originates from fluorescence of copolymerized FA (473 nm excitation) present in the core region. The red image originates from R6G (532 nm excitation) covalently attached to the AA in the shell region. The yellow bar represents 1 µm. (B) Normalized fluorescence intensity of R6G (red) and FA (green) as the microgel was scanned along the white line drawn in (A).

Importantly, the images in Figure 2-3A and the intensity map in Figure 2-3B confirm that the AA-carboxyls are located nearly exclusively in the shell region of the core–shell microgel. AA groups are known to distribute evenly throughout the microgel when synthesized via a one-step protocol.[26] The two-step synthesis protocol was shown previously by Jones and Lyon[28] to segregate AA groups to the periphery. Potentiometric titration of these core–shell microgels showed a global AA content of 8.0 mol % relative to NIPAM, which compares favorably with the 8.7 mol % expected for quantitative incorporation assuming identical reactivity ratios of AA and NIPAM. If distributed evenly throughout the volume of a spherical shell of average radius 1.3 ± 0.25 μm, where the thickness of the shell was derived from the inspection of Figure 2-3B, then the average separation between adjacent AA groups would be on the order of 50 Å.

To verify that these core–shell microgels undergo a VPT, fluorescence microscopy was employed to visualize R6G-modified p(NIPAM-co-FA)/p(NIPAM-co-AA) microgels at a temperature well below (20 °C) and well above (40 °C) the expected VPT temperature. As shown in Figure 2-4A, B, there is a drastic reduction in diameter at 40 °C, demonstrating the presence of a VPT akin to that expected for pNIPAM. From Figure 2-4A and B, an estimate of the size of the microgels by measuring their end-to-end fluorescence profiles reveal a 50% decrease in diameter above the VPT, corresponding to a nearly 90% volume decrease. These images were acquired at pH 7, where the AA carboxyls in the shell are deprotonated. The presence of such negative charges in the shell does not appear to hinder the de-swelling behavior of the microgels.

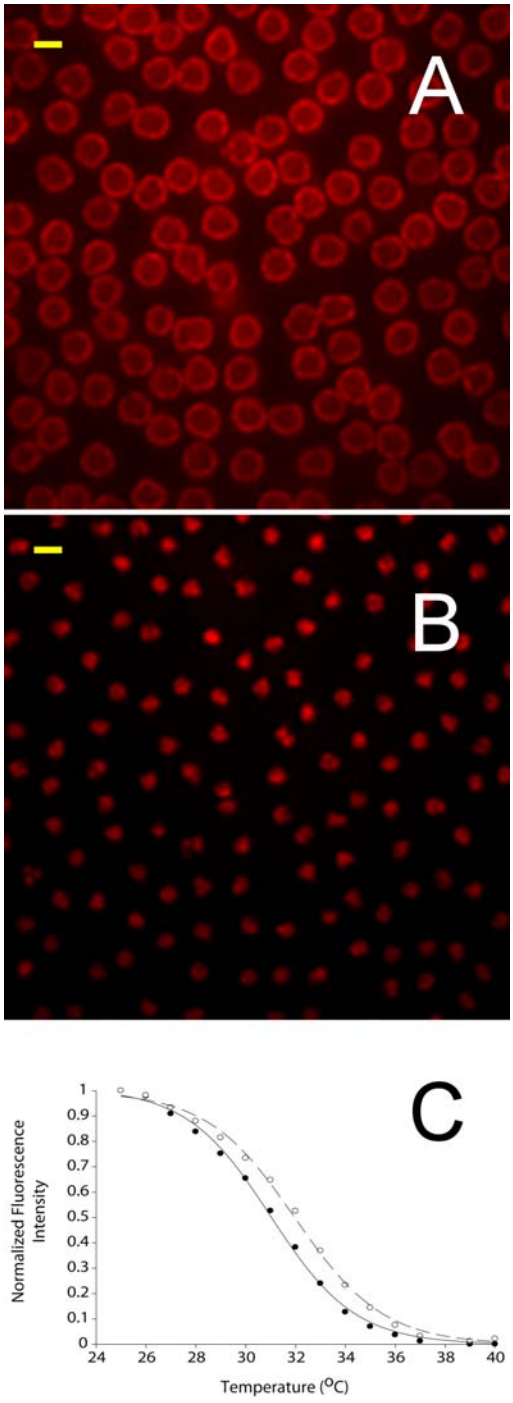

Figure 2-4: VPT behaviour of microgels. Fluorescence image of R6G-modified non-HM microgels in tris buffer at (A) 20 °C, that is, below the VPT temperature, and (B) at 40 °C, that is, above the VPT temperature. The diameters decrease by roughly 50% at the higher temperature, corresponding to a volume decrease of nearly 90%. The yellow bar in both represents 1 µm. (C) Normalized 520 nm emission intensity of non-HM microgels (○) and HM microgels (●) as a function of temperature. The line-of-best-fit for each data set corresponds to a three-parameter sigmoidal model. The temperature at which the fluorescence is quenched to 50% of its maximum value was taken to be the VPT temperature and equaled 32.0 °C for non-HM microgels and 31.0 °C for HM microgels.

To determine the temperature of the VPT more precisely, we examined p(NIPAM-co-FA)/p(NIPAM-co-AA) core–shell microgels spectroscopically for FA fluorescence intensity as a function of temperature. Kobayashi et al.[29] showed that polymerized FA could be used to determine accurately the temperature of the VPT of pNIPAM-based microgels. The fluorescein dianion is the most fluorescent species at a pH in excess of 6.3.[30] It is known to be an indicator of the degree of hydrogen bonding because its absorption and emission maxima change in response to a change in the hydrogen bonding environment.[31] As the microgel undergoes a VPT, the number of hydrogen bonds present in its matrix decreases because of the expulsion of water,[32] which shifts the fluorescence maximum away from 520 nm, the maximum emission wavelength at low temperatures. Indeed, a new peak around 537 nm was seen to emerge at higher temperatures (data not shown). Furthermore, fluorescein self-quenching could also occur at temperatures above that of the VPT as the intermolecular distance between the fluorophores decreases. Regardless, as shown in Figure 2-4C, the FA fluorescence quantum yield decreased drastically with increasing temperature. From such a curve, one obtains the VPT temperature, defined as that at which the fluorescence intensity drops to 50% of its maximum RT level. The p(NIPAM-co-FA)/p(NIPAM-co-AA) core–shell microgels exhibited a VPTT of 32.0 °C, a typical value for pNIPAM-based microgels.[33]

Tetradecylamine hydrophobes were introduced covalently and specifically into the shell region of the core–shell microgels by post-polymerization modification of the AA carboxyl groups as described in Figure 2-1. The hydrophobes are intended to act as anchoring groups around which the lipids of the lipid bilayer component of the Lipogel can assemble. The degree of hydrophobic modification was assessed via ^{13}C NMR, which permitted ready resolution of the tetradecylamine methylene and pNIPAM methyl groups. (See Appendix A.) Under spectroscopic

conditions leading to full relaxation and no NOE effects, a simple integration of these two resonances provided the desired degree of hydrophobic modification for a given AA content.

Quantitative modification of the AA carboxyls was achieved after an optimal combination of solvent, reactant stoichiometries, and reaction conditions was determined. Specifically, ethanol was found to serve as a good solvent for the microgel, the hydrophobe, and the coupling reagent TCTU pre-dissolved in DMF, whereas a five-fold molar excess of hydrophobe relative to the AA carboxyl was necessary, with sonication to separate the microgels prior to activation. Under such optimal reaction conditions, essentially 100% of the AA carboxyls were hydrophobically modified.

DLS showed that such hydrophobic modification resulted in a modest 10% decrease in the size of the microgels to a diameter of 1.19 μm, whereas, as shown in Figure 2-4C, the VPT temperature decreased marginally to 31.0 °C. Both of these results underscore the minimal effect imparted to the microgel by this degree of hydrophobic modification of the shell with tetradecyl alkanes.

2.3.2 Lipogel Fabrication

As shown in Figure 2-2, the first step in the strategy devised for Lipogel fabrication involves binding of unilamellar liposomes to HM core–shell pNIPAM/p(NIPAM-co-AA) microgels to localize and concentrate lipids at the microgel surface. Liposome binding to both linear[1,2] and microgel[14] forms of HM pNIPAM has been previously demonstrated. The hydrophobes are thought to intercalate into the lipid bilayer of the liposomes, thereby stitching the pNIPAM to the lipid bilayer. In the case of linear HM pNIPAM, the polymer wraps itself around the

liposome surface. In the case of microgel HM pNIPAM, the liposomes cluster at the microgel surface.

Liposomes can be formed in a number of ways, but a simple means is to first hydrate a lipid film by adding water/buffer, then impose a series of freeze–thaw–vortex cycles which creates LMVs, and finally extrude the LMVs through a polycarbonate filter having a particular pore size. Initial fabrication trials in which HM microgels were added during the first lipid hydration step prior to the freeze–thaw–vortex cycles were abandoned because it proved to be virtually impossible to separate nonbound from microgel-bound MLVs because of their similar sizes and densities. Instead, extruded LUVs (diameter 110 nm) were first produced, which were then incubated together with HM microgels. The far smaller non-bound LUVs were then easily separated from the far larger LUV–HM microgel complexes by a simple low-speed centrifugation step. The continuous breakage and reformation of the lipid bilayers imposed by successive freeze–thaw cycles[34] will, in the presence of excess lipid, encourage the formation of a continuous lipid bilayer both by fusion of adjacent bound liposomes and by "filling in" of local defects.[35] Without such freeze–thaw cycles, the microgel core is not sequestered from the exterior solution; that is, the lipid coating is leaky and likely to consist of individual non-fused LUVs bound at the microgel shell surface, similar to the materials studied by Mackinnon et al.[14]

Figure 2-5 shows a fluorescence microscopy image of the results of such a Lipogel fabrication wherein the LUVs contained 0.05 mol % RhB-PE and were bound to HM-p(NIPAM-co-FA)/p(NIPAM-co-AA) core–shell microgels. This permits separate and independent excitation of the RhB-PE in the lipid-binding region and that of FA in the core region of the microgel. As is obvious from the image in Figure 2-5, there is virtually complete co-localization of the respective fluorescence signals in that each and every microgel sphere is completely

surrounded by a coating of lipid. There is a small population of liposomes lacking a microgel sphere at their center. Therefore, the described Lipogel fabrication method efficiently coats the core–shell microgels with a layer of lipid without requiring an enormous excess of lipid to achieve full coverage while permitting ready removal of that excess afterward.

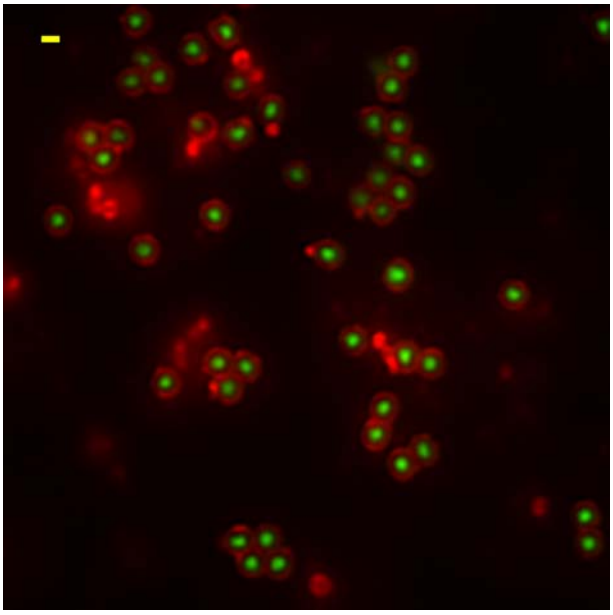

Figure 2-5: Dual-color fluorescence images of Lipogels fabricated from HM-p(NIPAM-co-FA)/p(NIPAM-co-AA) microgels plus liposomes containing 0.05 mol % RhB-PE. The green signal indicates the presence of a microgel (FA fluorescence), whereas the red signal corresponds to the lipid coat (RhB-PE fluorescence). It is evident that all microgels are coated with a layer of lipid. The yellow bar represents 1 µm.

2.3.3 Continuity of the Lipogel Lipid Bilayer

Whereas the fluorescence image in Figure 2-5 clearly indicates complete coverage of the microgel spheres with a coating of lipid, it does not permit one to determine if that coating consists simply of individual LUVs densely bound at the microgel surface, or whether, instead, individual LUVs have fused into a continuous lipid bilayer, either single or multilamellar. Previous experience with liposome binding to pNIPAM-based “hairy” microgels formed using a

one-step synthesis protocol, whether liposome binding was mediated via biotin–avidin conjugation[16] or hydrophobic modifications, showed that fusion of microgel-bound LUVs tended not to occur under such circumstances. Our adoption here of the core–shell microgel morphology was with the intention of providing a smoother outer surface upon which to assemble LUVs and thus circumvent the possible intrusion of polymer strands between bound liposomes, that being the most likely barrier to liposome fusion.

To differentiate these two possibilities, FRAP measurements were performed. In the typical FRAP experiment, as applied to lipid bilayers, a well-defined small area of a planar bilayer is photobleached, after which lateral diffusion of non-photobleached lipids from the far larger outside area produces an eventual near 100% recovery of fluorescence in the photobleached region. For our purposes, if the lipid coating of the microgel spheres consists of individual liposomes, then recovery will not occur, whereas, a continuous lipid bilayer surrounding the microgel sphere will facilitate signal recovery after a certain time delay. Figure 2-6 shows a series of fluorescence microscopy images of lipid-coated microgels where the lipids contained 0.1 mol % NBD-PE as the fluorophore lipid marker. Figure 2-6A is a control image acquired prior to photobleaching, whereas Figure 2-6B was acquired immediately after photobleaching. The photobleached area, while as small as technically possible with our equipment, is significantly larger than the size of the LUVs originally bound and, indeed, constitutes a significant fraction of the total surface. Figure 2-6C was obtained 5 min later and shows considerable recovery of fluorescence intensity in the previously photobleached region. Qualitatively, this is consistent with the presence of a continuous lipid bilayer surrounding the microgel sphere; otherwise, no such recovery would have been observed.

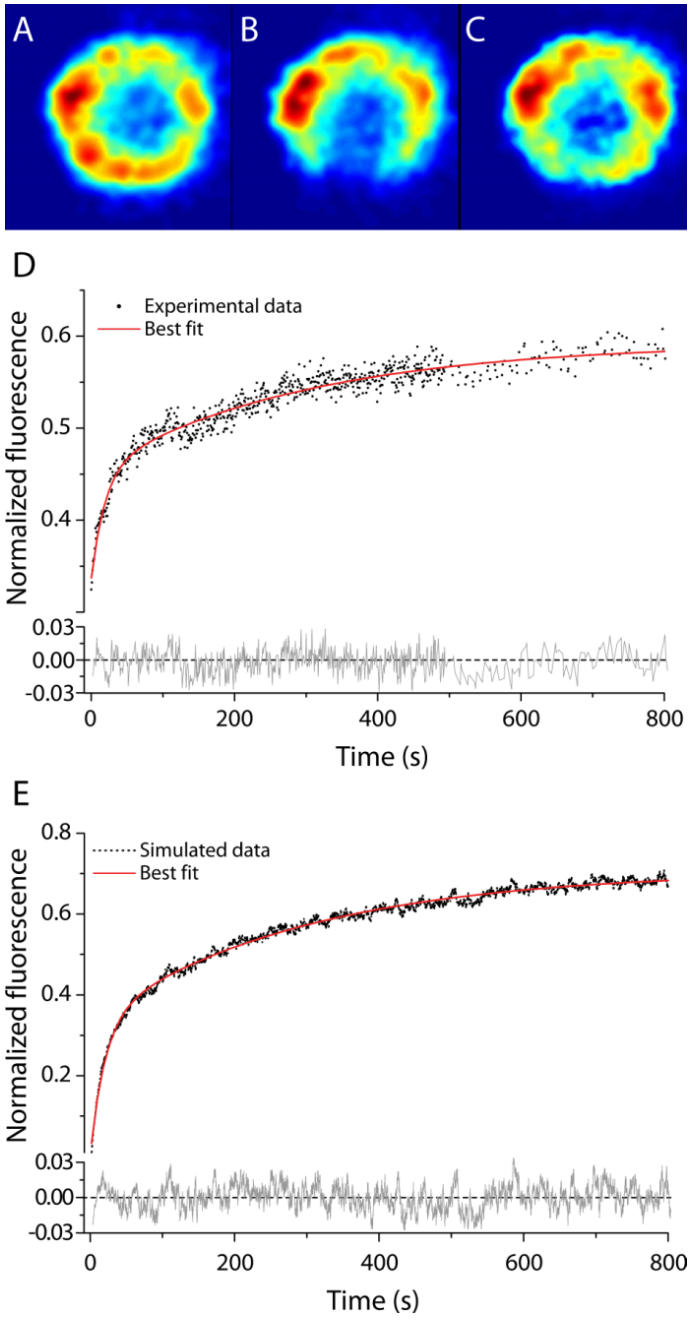

Figure 2-6: Confocal fluorescence images of a Lipogel fabricated from HM microgels and 0.1 mol % NBD-PE-containing liposomes in tris buffer subjected to a FRAP experiment: (A) before photobleaching, (B) immediately after a short photobleaching pulse, and (C) ca. 5 min after the photobleaching pulse. For quantitative analysis, a FRAP curve was obtained (D). The FRAP recovery curve was fit to a bi-exponential function (see the text) with fitting parameters, as listed in Table 2-1. (E) Monte Carlo simulation of fluorophores diffusing on a sphere and subjected to a FRAP experiment with dimensions and parameters approximating those employed experimentally. Two different diffusion coefficients were assumed: 1.1×10^{-9} (47% population) and 4.4×10^{-11} cm^2 s^{-1} (53%). The Monte Carlo recovery curve was likewise fit to a bi-exponential expression with parameters listed in Table 2-1. The fitting residuals are also shown for their respective curves.

A typical experimental fluorescence recovery curve is shown in Figure 2-6D, normalized to the intensity prior to photobleaching. The FRAP kinetics appear to be biphasic. To extract quantitative information, the recovery curves were fit to a bi-exponential function:

$$y = B - A_1 e^{-t/\tau_1} - A_2 e^{-t/\tau_2} \qquad \text{Equation 16}$$

where τ_1 and $\tau_2$are time constants describing the intensity recovery, A_1 and A_2 are their corresponding amplitudes, and B is the steady-state recovery level. The values of these parameters for the best fit results of this particular FRAP curve are listed in Table 2-1. The fittings confirm that the FRAP recovery is biphasic with time constants of 19 and 296 s. As previously noted, the size of the photobleached region is a significant fraction of the total Lipogel surface so that, consequently, a significant fraction of fluorophores are photobleached and the fluorescence recovers to only 60% of its initial level.

Table 2-1: FRAP Curve Fit Data for a Bi-Exponential Model

Data source	A_1	τ_1(s)	A_2	τ_2(s)	B
Experimental	0.12	19.0 ± 0.1	0.16	296.0 ± 2.3	0.59
Monte Carlo	0.30	20.3 ± 0.1	0.37	293.4 ± 1.6	0.71

In the absence of an analytical expression for extracting the diffusion coefficient(s) from the FRAP recovery curve for a micrometer-sized spherical lipid bilayer photobleached in this fashion, we resorted to numerical simulations. Monte Carlo simulations of a FRAP experiment for a model system consisting of fluorophores randomly distributed on a sphere were

conducted as described in detail in Appendix A. The size and the depth of the bleaching area, the observation time, and the step size were chosen to match closely the experimental conditions. The simulations produced a mono-exponential recovery curve for the case of a single diffusion coefficient on the sphere. (See Appendix A). In contrast, a combination of nearly equally abundant "fast" and "slow" diffusive components was required to reproduce satisfactorily the main features of the experimental FRAP curve (Figure 2-6E, Table 2-1). The fast diffusion constant used in simulations was $(1.1 \pm 0.2) \times 10^{-9}$ cm^2/s, corresponding to an exponential recovery time of 19.6 ± 4.1 s. Similarly, to simulate a characteristic recovery time of 290–300 s, we had to set the slow diffusion constant at $(4.4 \pm 0.8) \times 10^{-11}$ cm^2/s. The relative contribution of the fast/slow component was roughly 45/55. From such numerical simulations, it is determined that for the five Lipogels FRAP curves measured experimentally the fitted time constants correspond to a fast diffusion constant of $(1.3 \pm 0.7) \times 10^{-9}$ cm^2/s and a slow diffusion constant of $(4.7 \pm 1.0) \times 10^{-11}$ cm^2/s.

The presence of two differently diffusing lipid populations might originate with differences in the local environment experienced by lipids within the inner versus the outer leaflet of the Lipogels, assuming a unilamellar lipid bilayer coating: an assumption supported by the lamellarity tests described below. We note that the faster lateral diffusion coefficient is still an order of magnitude slower than that expected for POPC in liposomes of comparable composition. In many SPBs, however, slower lateral diffusion is typically observed.[36] In our Lipogels, the lipid bilayer coating may well not be smooth but rather may be corrugated because of imperfections in, and the finite thickness of, the shell region, which produces, in turn, a non-planar distribution of hydrophobic anchor positions. Such corrugations would yield a slower apparent lateral diffusion coefficient overall. The second, even slower diffusing

component may be the result of obstruction by immobile hydrophobic anchors attached to the immobile polymer support and specific, therefore, to lipids on the inner leaflet. A calculation of their density in these Lipogels indicates that one tetradecyl hydrophobic anchor is separated from another by 50 Å, constituting, therefore, a considerable obstruction effect to diffusion for the inner monolayer nearest the polymer support.

2.3.4 Lamellarity of the Lipogel Lipid Bilayer

Having established the continuity of the lipid bilayer coating the hydrogel support, a test of whether this consisted of a single lipid bilayer or multiple such bilayers was instituted. The so-called lamellarity of lipid coatings may be tested in a number of ways.[37–39] A simple, direct method is to expose Lipogels containing the fluorescent lipid NBD-PE to sodium dithionite, which reduces NBD to its non-fluorescent amine form but will not permeate an intact lipid bilayer. As shown in Figure 2-7, exposing Lipogels to sodium dithionite reduces the NBD-PE fluorescence by roughly 55%, which is essentially the value expected for a single lipid bilayer coating the Lipogels. Disrupting the lipid coating with detergent reduces the NBD-PE fluorescence to zero. These results definitively preclude the possibility, however remote, that a lipid monolayer was coating the hydrophobically modified hydrogel surface. Another interpretation consistent with the quenching results is that in addition to a contiguous lipid bilayer coating the shell there are adherent LUVs. These adherent LUVs would diffuse only very slowly, potentially explaining the biphasic FRAP kinetics. The fluorescence images shown in Figure 2-5, however, indicate that any such population of adherent LUVs must be quite small. Thus, we favor the interpretation that Lipogels fabricated under these conditions bear a lipid coating consisting of a single contiguous impermeable lipid bilayer.

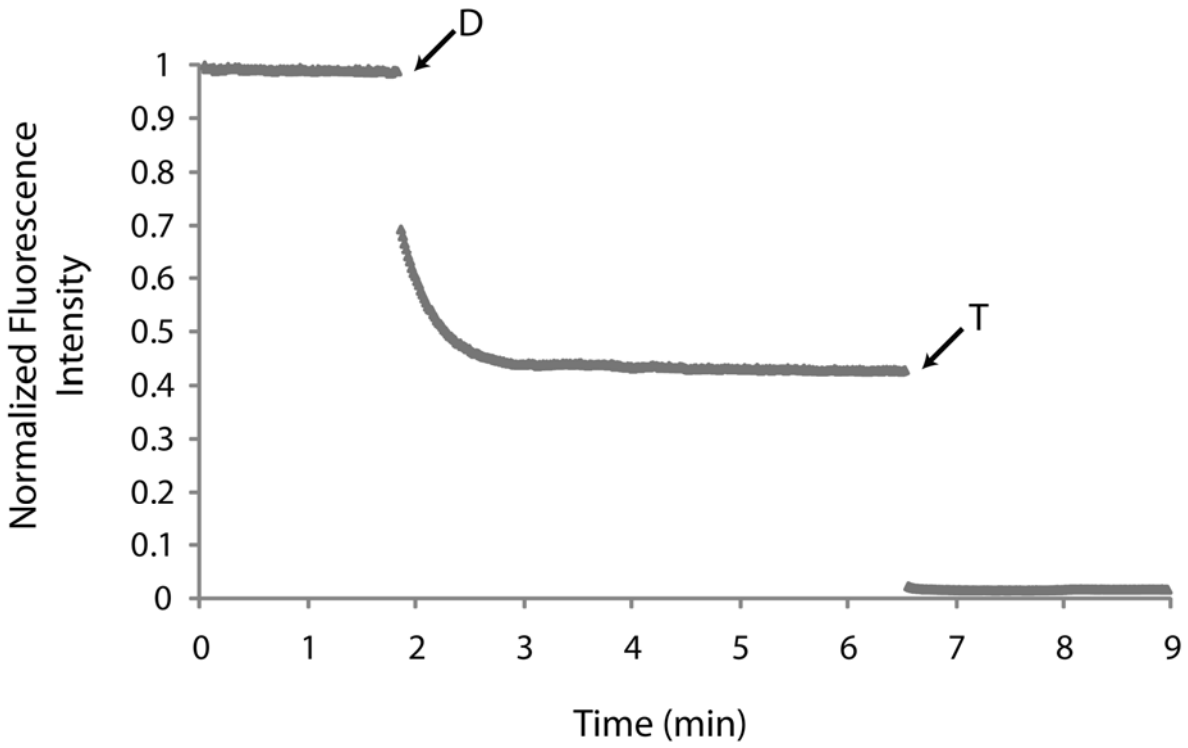

Figure 2-7: Lamellarity test via sodium dithionite quenching of NBD-PE fluorescence. Lipogels (0.1 mg in 2 mL tris buffer) containing 0.1 mol % NBD-PE were exposed to the fluorescence quencher (20 µL of 1 M sodium dithionite) at time D while continuously monitoring fluorescence. The lipid coating was disassembled with detergent (20 µL of 5% Triton) at time T.

2.3.5 VPT and the Lipogel Lipid Bilayer

Having established that the hydrogel sphere is enclosed by a single continuous impermeable lipid bilayer, it was of interest to examine the lipid bilayer's response to temperatures above the microgel VPT temperature. Figure 2-8 shows fluorescence images of Lipogel-encapsulated CF below (A) and above (B) the VPT temperature. It is clear that the presence of the lipid bilayer coating does not prevent the hydrogel from undergoing the normal VPT at elevated temperatures. To probe the response of the lipid bilayer coating to the microgel VPT, we incorporated the fluorescent lipid RhB-PE, and the Lipogels were imaged as a function of temperature. Below the VPT temperature, the "donut" profile expected for a lipid bilayer coating the microgel surface is obtained, as shown in Figure 2-8C. Above the VPT

temperature, as shown in Figure 2-8D, the lipid bilayer appears to have collapsed onto a small central core but with regions of high curvature protruding into the surroundings. We postulate that these protrusions consist of excess lipid bilayer no longer in contact with the collapsed hydrogel, but still contiguous with regions of lipid bilayer remaining bound to the hydrogel via hydrophobic anchors. When the temperature is returned to a value below the VPT, as shown in Figure 2-8E, the lipid bilayer regains its former shape.

To probe the degree to which the lipid bilayer's permeability barrier properties were compromised by the extreme size and shape changes undergone in response to the microgel VPT, we developed a fluorescence assay to measure molecular permeation between the external bulk solution and the Lipogel's interior aqueous compartment. The fluorescence of calcein is quenched when complexed with cobalt, but EDTA separates the cobalt from the calcein and de-quenches the calcein fluorescence. When Lipogels were loaded with a cobalt–calcein complex, at a temperature below that of the VPT temperature, disrupting the lipid bilayer with Triton did not result in fluorescence enhancement (Figure 2-9A). The fluorescence remained quenched until EDTA addition, after which a significant fluorescence enhancement was seen. Figure 2-9B shows that even after 20 min of being heated above the VPT temperature in the presence of EDTA, the calcein fluorescence remains quenched, indicating that EDTA does not permeate the lipid bilayer under these conditions. Even multiple heating cycles failed to produce any significant fluorescence enhancement. Only when Triton was added to disrupt the bilayer did the calcein fluorescence increase to that of the control

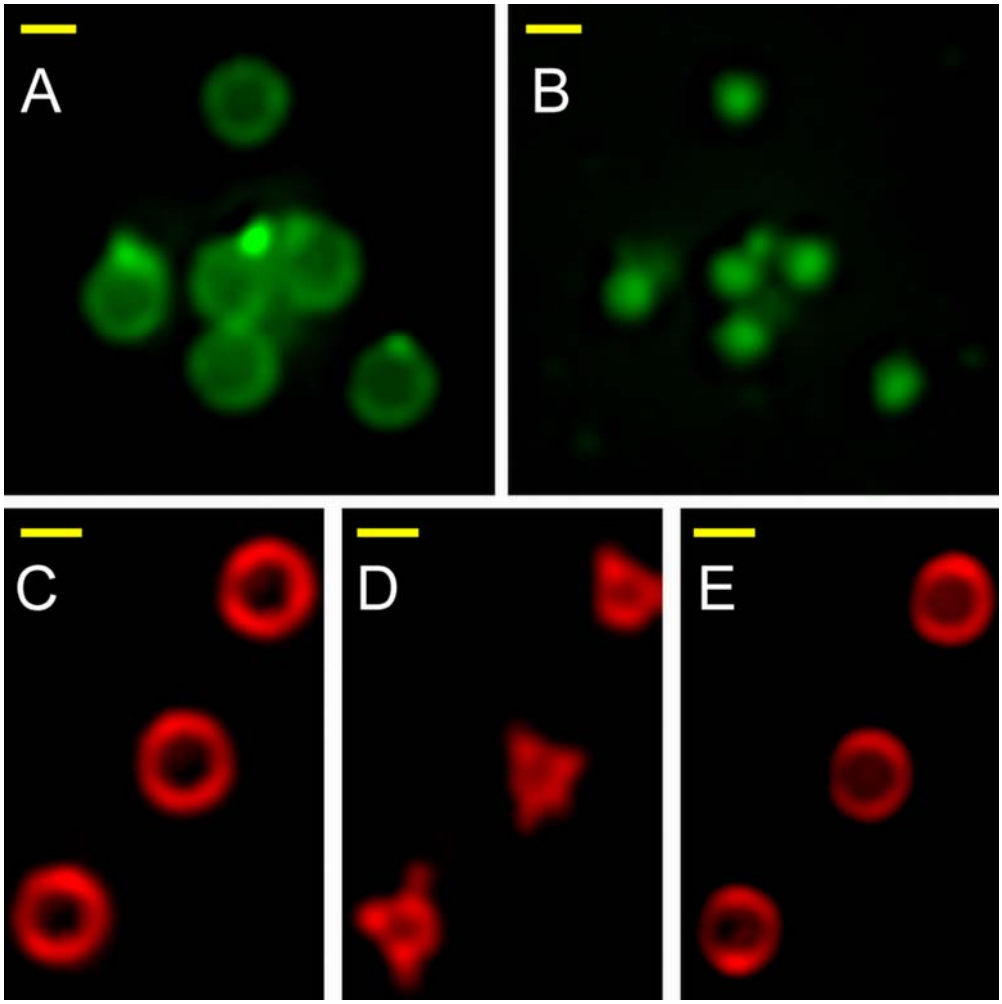

Figure 2-8: Fluorescence images of Lipogel-encapsulated CF in tris buffer at a temperature (A) below the VPT temperature and (B) above the VPT temperature, showing the 50% decrease in diameter undergone by the hydrogel component of the Lipogel due to the VPT. In addition, fluorescence images of Lipogels containing 0.05 mol % RhB-PE in the lipid bilayer component are shown for temperatures (C) below the VPT temperature, (D) above the VPT temperature, and (E) upon reverting to a temperature below the VPT.

value. We conclude that the elasticity of the POPC lipid bilayer permits it to remain intact as a permeability barrier even upon being subject to the VPT-induced shape changes evident in Figure 2-8D. Not all lipid bilayer compositions would be expected to be so forgiving.

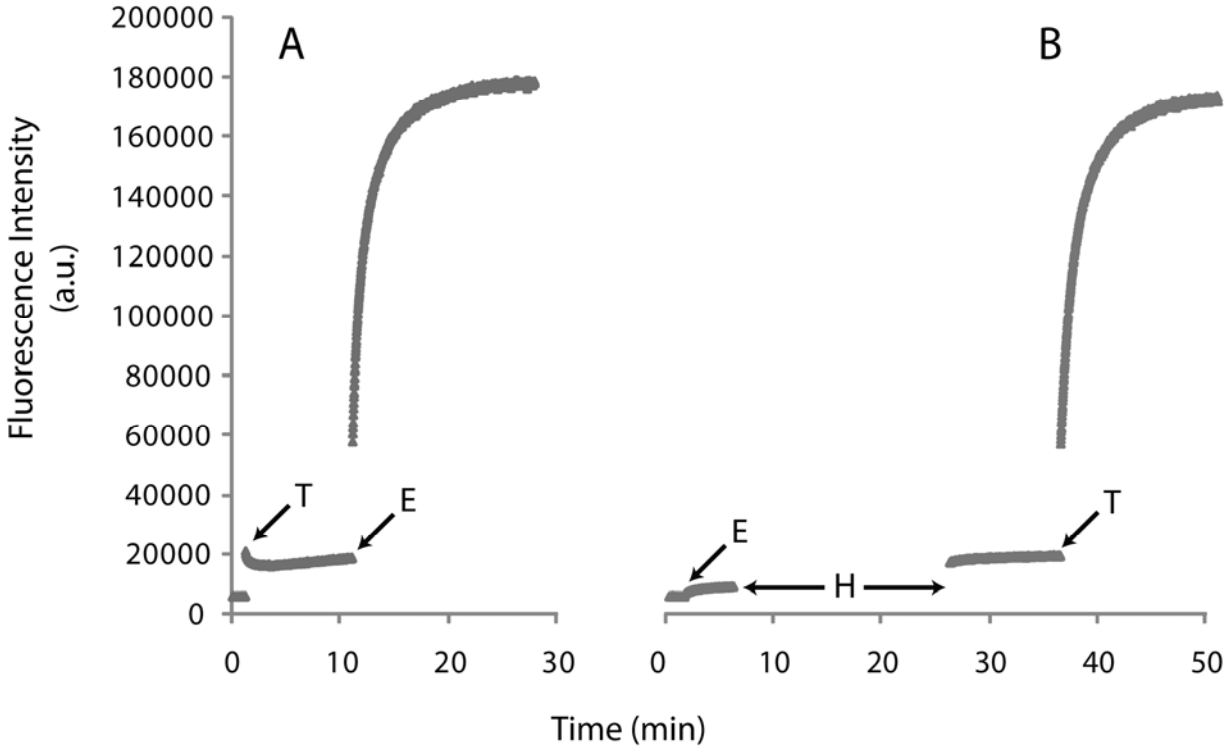

Figure 2-9: EDTA-dependent cobalt–calcein fluorescence enhancement assay to characterize the permeability of the Lipogel lipid bilayer above the VPT. Cobalt–calcein complexes were encapsulated in Lipogels and 0.1 mg of Lipogels were suspended in 2.0 mL of tris buffer initially at room temperature. (A) Control showing room-temperature effects of detergent disruption of Lipogel lipid bilayer on calcein fluorescence with subsequent exposure to EDTA and consequent release of calcein from complexation with cobalt. (B) Effects of heating above the temperature of the VPT. Point T indicates the addition of 20 µL of 5% Triton, whereas point E indicates the addition of 2 µL of 1 M EDTA. Point E indicates the addition of 2 µL of 1 M EDTA. H indicates the duration of exposure to a temperature of 40 °C, whereas point T indicates the addition of 20 µL of 5% Triton.

2.4 Conclusions

We have described the fabrication and characterization of Lipogels: micrometer-sized, single-lipid-bilayer-enclosed, thermoresponsive, hydrophobically modified, pNIPAM/p(NIPAM-co-AA) core–shell hydrogel spheres. The normal pNIPAM VPT was shown to occur regardless of the presence of either hydrophobic surface modifications or a lipid coating. The lipid coating was shown to consist of a continuous, impermeable, single lipid bilayer enclosing, encapsulating, and sequestering the hydrogel sphere. The volume collapse of the microgel

above its VPT was mirrored by the lipid bilayer coating but with the formation of highly curved bilayer regions reflecting the excess bilayer surface relative to the reduced microgel surface. These changes were completely reversible, and the permeability barrier properties of the lipid bilayer coating were not compromised by the VPT.

2.5 References

(1) Franzin, C. M.; Macdonald, P. M.; Polozova, A.; Winnik, F. M. *Biochim. Biophys. Acta BBA-Biomembr.* **1998**, *1415*, 219–234.

(2) Polozova, A.; Winnik, F. M. *Biochim. Biophys. Acta BBA-Biomembr.* **1997**, *1326*, 213–224.

(3) Wu, X. S.; Hoffman, A. S.; Yager, P. *Polymer* **1992**, *33*, 4659–4662.

(4) Meyer, O.; Papahadjopoulos, D.; Leroux, J. *FEBS Lett.* **1998**, *421*, 61–64.

(5) Han, H. D.; Shin, B. C.; Choi, H. S. *Eur. J. Pharm. Biopharm.* **2006**, *62*, 110–116.

(6) Kono, K.; Henmi, A.; Yamashita, H.; Hayashi, H.; Takagishi, T. *J. Controlled Release* **1999**, *59*, 63–75.

(7) Wang, Y.; Winnik, F. M.; Clarke, R. J. *Biophys. Chem.* **2003**, *104*, 449–458.

(8) Ringsdorf, H.; Venzmer, J.; Winnik, F. M. *Angew. Chem. Int. Ed. Engl.* **1991**, *30*, 315–318.

(9) Ringsdorf, H.; Sackmann, E.; Simon, J.; Winnik, F. M. *Biochim. Biophys. Acta BBA - Biomembr.* **1993**, *1153*, 335–344.

(10) Simon, J.; Kühner, M.; Ringsdorf, H.; Sackmanna, E. *Chem. Phys. Lipids* **1995**, *76*, 241–258.

(11) Kim, J.; Kim, J. *Colloids Surf. B Biointerfaces* **2002**, *24*, 45–52.

(12) Kim, J.; Bae, S. K.; Kim, J. *J. Biochem. (Tokyo)* **1997**, *121*, 15–19.

(13) Hay, D. N. T.; Rickert, P. G.; Seifert, S.; Firestone, M. A. *J. Am. Chem. Soc.* **2004**, *126*, 2290–2291.

(14) MacKinnon, N.; Guérin, G.; Liu, B.; Gradinaru, C. C.; Rubinstein, J. L.; Macdonald, P. M. *Langmuir* **2010**, *26*, 1081–1089.

(15) Kazakov, S.; Kaholek, M.; Teraoka, I.; Levon, K. *Macromolecules* **2002**, *35*, 1911–1920.

(16) MacKinnon, N.; Guérin, G.; Liu, B.; Gradinaru, C. C.; Macdonald, P. M. *Langmuir* **2009**, *25*, 9413–9423.

(17) Chujo, Y.; Sada, K.; Matsumoto, K.; Saegusa, T. *Macromolecules* **1990**, *23*, 1234–1237.

(18) Bures, P.; Huang, Y.; Oral, E.; Peppas, N. A. *J. Controlled Release* **2001**, *72*, 25–33.

(19) Meng, Z.; Smith, M. H.; Lyon, L. A. *Colloid Polym. Sci.* **2009**, *287*, 277–285.

(20) McIntyre, J. C.; Sleight, R. G. *Biochemistry (Mosc.)* **1991**, *30*, 11819–11827.

(21) Liu, B.; Mazouchi, A.; Gradinaru, C. C. *J. Phys. Chem. B* **2010**, *114*, 15191–15198.

(22) Abramoff, M.; Magelhaes, P.; Ram, S. *Biophotonics Int.* **2004**, *11*, 36–42.

(23) Mazouchi, A.; Liu, B.; Bahram, A.; Gradinaru, C. C. *Anal. Chim. Acta* **2011**, *688*, 61–69.

(24) Wohland, T. *Biophys. J.* **2001**, *80*, 2987–2999.

(25) Varga, I.; Gilanyi, T.; Meszaros, R.; Filipcsei, G.; Zrinyi, M. *J. Phys. Chem. B* **2001**, *105*, 9071–9076.

(26) Hoare, T.; Pelton, R. *Curr. Opin. Colloid Interface Sci.* **2008**, *13*, 413–428.

(27) Hendrickson, G. R.; Smith, M. H.; South, A. B.; Lyon, L. A. *Adv. Funct. Mater.* **2010**, 1697–1712.

(28) Jones, C. D.; Lyon, L. A. *Macromolecules* **2000**, *33*, 8301–8306.

(29) Kobayashi, H.; Nishikawa, M.; Sakamoto, C.; Nishio, T.; Kanazawa, H.; Okano, T. *Anal. Sci.* **2009**, *25*, 1043–1047.

(30) Klonis, N.; Sawyer, W. H. *J. Fluoresc.* **1996**, *6*, 147–157.

(31) Klonis, N.; Clayton, A. H. A.; Voss, E. W.; Sawyer, W. H. *Photochem. Photobiol.* **1998**, *67*, 500–510.

(32) Ahmed, Z.; Gooding, E. A.; Pimenov, K. V.; Wang, L.; Asher, S. A. *J. Phys. Chem. B* **2009**, *113*, 4248–4256.

(33) Schild, H. G. *Prog. Polym. Sci.* **1992**, *17*, 163–249.

(34) Llu, L.; Yonetani, T. *J. Microencapsul.* **1994**, *11*, 409–421.

(35) MacDonald, R. I.; MacDonald, R. C. *Biochim. Biophys. Acta BBA - Biomembr.* **1983**, *735*, 243–251.

(36) Ng, C. C.; Cheng, Y.; Pennefather, P. S. *Biophys. J.* **2004**, *87*, 323–331.

(37) Kiser, P. F.; Wilson, G.; Needham, D. *J. Controlled Release* **2000**, *68*, 9–22.

(38) Jin, T.; Pennefather, P.; Lee, P. I. *FEBS Lett.* **1996**, *397*, 70–74.

(39) Troutier, A.; Véron, L.; Delair, T.; Pichot, C.; Ladavière, C. *Langmuir* **2005**, *21*, 9901–9910.

Bicellogels: Lipid Bilayer Deposition on Soft Polymer Surfaces using Bicelles

3.1 Introduction

A new method of lipid bilayer deposition at surfaces has been recently reported involving the use of bicelles.[1–3] Relative to liposomes, bicelles enjoy two important advantages as precursors for lipid bilayer coatings. First, bicelle self-assembly is spontaneous, versus the sonication or extrusion procedures necessary to produce unilamellar liposomes. Second, bicelles adopt a discoidal morphology, provided the long-chain / short-chain molar ratio, q, falls in the range $1 < q < 3$, which permits deposition of individual planar bicelle discs. As was demonstrated in Chapter 2, spherical liposomes when deposited must generally be induced to fuse into a planar bilayer, using various triggers such as addition of Ca^{2+},[4–6] freeze-thaw,[7,8] or dehydration-rehydration cycling,[9] any of which can leave intact liposomes adsorbed alongside or atop patches of fused lipid bilayer.[10,11]

Here, we demonstrate the use of bicelles to deposit a continuous, unilamellar lipid bilayer at the surface of, and completely encapsulating, a pNIPAM microgel. The core-shell morphology of the microgel allowed AA groups to be isolated in the shell region to create a negatively-charged surface. The bicelles were composed of the zwitterionic phospholipids 1,2-dimyristoyl-*sn*-glycero-3-phosphocholine (DMPC) and 1,2-dihexanoyl-*sn*-glycero-3-phosphocholine (DHPC), plus the cationic amphiphile 1,2-dimyristoyl-3-trimethylammonium-propane (DMTAP) in the molar ratios q = (DMPC+DMTAP)/DHPC = 2 and DMPC/DMTAP = 95/5. Using a combination of ^{31}P NMR, fluorescence recovery after photobleaching (FRAP), fluorescence quenching, and mass spectrometry techniques, we show that simple mixing of anionic hydrogel beads with cationic bicelles at a temperature above the gel-to-liquid-

crystalline phase transition (T_M) of DMPC sufficed to produce fusion of individual electrostatically-adherent bicellar discs into a continuous, unilamellar lipid bilayer completely surrounding the hydrogel bead and from which the short-chain species DHPC was entirely absent. While such "Bicellogels" are intrinsically useful in their own right, the approach of using bicelles to create SLBs would appear to be broadly applicable, whether the support is planar or spherical, soft or hard, and can be fabricated independent of the means of attachment, whether mediated by electrostatic, or hydrophobic, or bioconjugation interactions.

3.2 Materials and Methods

3.2.1 Materials

DMPC, DMTAP, DHPC, and NBD-PE were purchased from Avanti Polar Lipids (Alabaster, AL). RhB-PE was purchased from Invitrogen (Carlsbad, CA). All other reagents were purchased from Sigma Aldrich (Oakville, ON).

3.2.2 Fabrication of pNIPAM/p(NIPAM-co-AA) Core-shell Microgels

The pNIPAM/p(NIPAM-co-AA) core-shell microgels were prepared and characterized as described in Chapter 2.

3.2.3 Preparation of Discoidal Bicelles

The *q* = 2 bicelle samples with 5 mol % DMTAP were prepared by dissolving DHPC (7.42 µmol, 3.4 mg), DMPC (14.1 µmol, 9.6 mg), and DMTAP (0.742 µmol, 0.4 mg) in chloroform, plus either 0.10 mol % NBD-PE (0.022 µmol) or 0.05 mol % RhB-PE (0.011 µmol), depending on the

assay to be performed. The dissolved lipids were dried under a stream of N_2 to produce a lipid film and left in a desiccator under vacuum for 12 hours to remove residual solvent. The lipid film was hydrated with 1 mL of 10 mM Tris buffer (pH=7.4) and the resulting lipid suspension was subjected to several freeze-thaw cycles wherein the hydrated lipids were frozen in liquid N_2, thawed in a 40 °C water bath, and vortexed. The bicelle preparation was then stored at 4 °C until use.

3.2.4 Fabrication of Bicellogels

Typically, 0.25 mg of microgels were added to 2.0 mg of bicelles in 1 mL of 10 mM Tris buffer (pH 7.4). This mixture was gently swirled for 4 hours at room temperature, followed by standing incubation at 30 ^{o}C for a further 12 hours. Excess lipid was removed by repeatedly (3 – 5 x) centrifuging the resulting Bicellogels at 4k RPM for 5 minutes to form a pellet, removing the supernatant, and re-suspending the pellet in 1 mL of 10 mM Tris buffer (pH 7.4).

3.2.5 Preparation of Unilamellar Liposomes

Cationic unilamellar DMPC/DMTAP (95/5 mol/mol) liposomes were prepared by first co-dissolving DMPC (7.08 µmol, 4.8 mg) and DMTAP (0.339 µmol, 0.2 mg) in chloroform, along with 0.10 mol % NBD-PE. The chloroform was removed under a stream of N_2 to produce a lipid film, which was placed in a vacuum desiccator for 12 hours to eliminate traces of solvent. The lipid film was hydrated with 0.5 mL of 10 mM Tris buffer (pH 7.4) and subjected to several cycles of freeze-thaw, as above. The resulting multilamellar vesicles were then extruded through a 100 nm pore-size polycarbonate membrane to produce unilamellar vesicles.

3.2.6 Bicellogel Binding Assay

Increasing amounts of RhB-PE-labelled, q = 2, 5 mol % DMTAP bicelles were added to a constant weight of pNIPAM/p(NIPAM-*co*-AA) core-shell microgels and the mixtures were allowed to incubate as described above. The resulting bicelle – microgel complexes were isolated by centrifugation and the pellet was washed with 10 mM Tris buffer (pH 7.4).

Fluorescence measurements on the wash were conducted on a Tecan Infinite M1000 PRO microplate reader (Männedorf, Switzerland). In each microplate well, 20 µL of sample was combined with 80 µL of 0.2 M sodium cholate. The wells were excited at 530 nm and a scan was performed from 570 to 620 nm with the same gain level used for all samples. 50 flashes were used at a frequency of 400 Hz, with an integration time of 20 µs. A settle time of 50 ms was used and the temperature was kept at 24 °C. A calibration curve was established from measurements on 20 µL samples of RhB-PE-labelled bicelles at increasing concentration with 80 µL of 0.2 M sodium cholate added as above. Control measurements on samples comprised of 100 µL 0.2 M sodium cholate, and 20 µL 10 mM Tris buffer (pH 7.4) plus 80 µL 0.2 M sodium cholate were used to correct the emission spectra.

3.2.7 Fluorescence Imaging and FRAP Measurements

Fluorescence images and FRAP measurements were obtained using a custom-built confocal laser scanning microscope using the method described in Chapter 2 FRAP measurements were repeated on at least 4 individual Bicellogels. All experiments were conducted at a temperature of 20 °C.

The measured FRAP curves were fit with several exponential models, and the Akaike information criterion (AIC) was used to select a biphasic exponential function (Equation 16) as the most likely model. Also, to extract diffusion coefficients from FRAP curves, a Monte Carlo simulation of the random Brownian motion of fluorophores on the surface of a sphere to produce was used as previously described in Chapter 2.

3.2.8 Fluorescence Quenching Assay using Sodium Dithionite

A sodium dithionite NBD-PE quenching assay was performed on bicelles, Bicellogels and unilamellar liposomes incorporating 0.1 mol % of NBD-PE. A 1 M sodium dithionite, 1 M Tris solution was prepared immediately prior to use. Using a QuantaMaster PTI spectrofluorimeter (Photon Technology International, Lawrenceville, NJ) equipped with a Quantum Northwest TC 125 temperature controller (Liberty Lake, WA), the excitation was set to 470 nm and the emission was monitored at 532 nm using a time based scan via the FelixGX software. An aliquot of sample was diluted to 2 ml using 10 mM Tris buffer (pH 7.4) in a 4 mL quartz cuvette and allowed to thermally equilibrate to a set temperature for at least 10 minutes. The emission was then monitored for several minutes at the rate of 1 point/sec. After obtaining a stable fluorescence reading for 1 minute, 20 µL of the sodium dithionite solution was added. The fluorescence emission intensity was monitored until a new baseline was achieved, following which 20 µL of 5 wt % Triton solution was added to disrupt the bilayer and quench the fluorescence entirely.

3.2.9 Solid State ^{31}P NMR Spectroscopy

Solid state ^{31}P NMR spectra were obtained with a Varian Inova 500 MHz NMR spectrometer using a T3 triple-resonance MAS probe. 20 mg of Bicellogels were packed in a 5 mm rotor and capped with a custom built leak-proof plug. The sample was allowed to thermally equilibrate to a particular temperature for at least 10 minutes. ^{31}P NMR spectra were recorded at 202 MHz using a spin echo pulse sequence under TPPM proton decoupling. The acquisition parameters were as follows: a 90° pulse length of 6.7 μs, an echo delay of 22.8 μs, a recycle delay of 4.0 s, and a spectral width of 100 kHz. Typically, 1,000–2,000 transients were collected for each spectrum and processed with an exponential multiplication equivalent to 100 Hz line broadening prior to Fourier transformation.

3.2.10 Electrospray Ionization Mass Spectrometry (ESI-MS)

Both Bicellogel-bound lipids and free bicelle lipids were analyzed via ESI-MS. Bicellogels were first stripped of bound lipids by immersion in acetone and the free microgels were removed by centrifugation. Methanol was added to the supernatant to obtain a 5 μM lipid solution. Free bicelle lipids were simply diluted to 5 μM using methanol. Using a syringe pump, the samples were introduced into the Micromass ZQ single quadruple electrospray ionization mass spectrometer (Waters Corporation, MA) operating in the positive ion mode at a flow rate of 30 μL/min with a capillary charge of +3.1 kV, cone voltage of 20 V and a source temperature of 100 °C. The samples were scanned over the range of 400–700 m/z with a scan acquired every second over a duration of 1 minute.

3.3 Results and Discussion

3.3.1 Charge Balance Regulates Cationic Bicelle Binding to Anionic Microgels

With the objective of depositing a lipid bilayer onto a spherical soft polymer surface starting from discoidal bicelles, it is critically important that the polymer support interact strongly and specifically with the bicelles. One means of doing so is through Coulombic attraction. To this end, pNIPAM/p(NIPAM-co-AA) core-shell microgels were fabricated such that the acrylic acid carboxyl functionalities are localized to the shell region, thus imparting to the microgel surface a high negative charge density at physiological pH. Cationic bicelles will be electrostatically attracted to, and bind with, the microgel anionic surface, as shown in Figure 3-1. Cationic bicelles in discoidal form were prepared using a long chain / short chain molar ratio q = 2, known to yield discoidal bicelles with diameters in the region of 200 Å.[12] Cationic charge was conferred by incorporating the cationic amphiphile DMTAP (5 mol % relative to DMPC).

In designing the Bicellogel formulation strategy outlined in Figure 3-1, careful consideration was given to the properties of the aqueous buffer and the temperature of deposition, with the goal of achieving saturation of the microgel surface with bound bicelles. By analogy with liposome fusion at surfaces to form a continuous lipid bilayer, it was anticipated that a critical density of bound bicelles would need to be achieved before bicelle fusion into a continuous lipid bilayer could occur. Since electrostatic attraction decreases with increasing ionic strength, a salt-free buffer was chosen in order to minimize charge screening and, hence, maximize the bicelle-microgel attraction. Note that, had some other mode of binding interaction been chosen, such as hydrophobic attraction or bioconjugation, such a

stricture would not have been necessary. The temperature at which the bicelle deposition is undertaken was also expected to profoundly influence the outcome. First, bicelle morphology changes in a complex manner with temperature,[60] but a key temperature is that of the gel-to-liquid-crystalline phase transition of DMPC (T_M = 23 ^oC), below which fusion is unlikely to occur. Second, pNIPAM microgels undergo a volume phase transition (VPT) at 32 ^oC wherein the water-swollen state at a lower temperature collapses, losing as much as 90% of its volume, at a temperature exceeding that of the VPT. Thus, temperature was carefully controlled to remain intermediate to the T_M of DMPC and the VPT of pNIPAM.

To determine the saturation level of bicelle binding, a constant amount of anionic microgel was titrated with increasing amounts of cationic bicelles containing RhB-PE. The amount of lipid bound was measured from the RhB-PE fluorescence with results as shown in Figure 3-2. When these binding data are expressed in terms of the number of bicelle cationic charges from DMTAP bound per microgel anionic charge from AA it is evident that binding is quantitative until charge balance is achieved, at which point little or no further binding occurs.

The results in Figure 3-2 indicate that all DMTAP molecules on a given bicelle are accessible to microgel carboxyls. If it is assumed that all DMTAP remain confined to a given face of a bicellar disc, then this result implies that the microgel matrix is able to wrap around a bound bicelle. This would likely prohibit fusion of adjacent bicelles but, as will be shown below, such bicelle fusion in fact appears to occur. An alternate explanation is that DMTAP is able to migrate from one bicelle face to the other, driven by electrostatic attraction to the relatively immobile microgel carboxyls. Since flip-flop of large, charged amphiphiles like DMTAP through a bilayer is very slow, we suggest that, instead, DMTAP diffuses around the bicelle rim such that its population rapidly re-equilibrates according to local electrostatics. Some simple geometric

considerations bolster this argument. Previously, we estimated that the average distance between adjacent AA groups in identical microgels would be on the order of 50 Å.[7] For a bicelle composed of 95/5 DMPC/DMTAP the centre-to-centre separation between individual DMTAP molecules would be on the order of 120 Å, assuming an area per DMTAP similar to that of DMPC (60 $Å^2$). If, however, all DMTAP migrate to one face of the bicelle, the effective composition at the interface would be 90/10 DMPC/DMTAP and the centre-to-centre separation between individual DMTAP molecules would be on the order of 60 Å, i.e., better matching the AA separation on the microgel surface. Further to this point, for a 200 Å diameter bicelle with globally 95/5 DMPC/DMTAP, if all DMTAP migrate to one face and bind electrostatically to surface carboxyls, each bicelle will have approximately 50 such points of electrostatic interaction, consistent with the strong, quantitative binding evident in Figure 3-2.

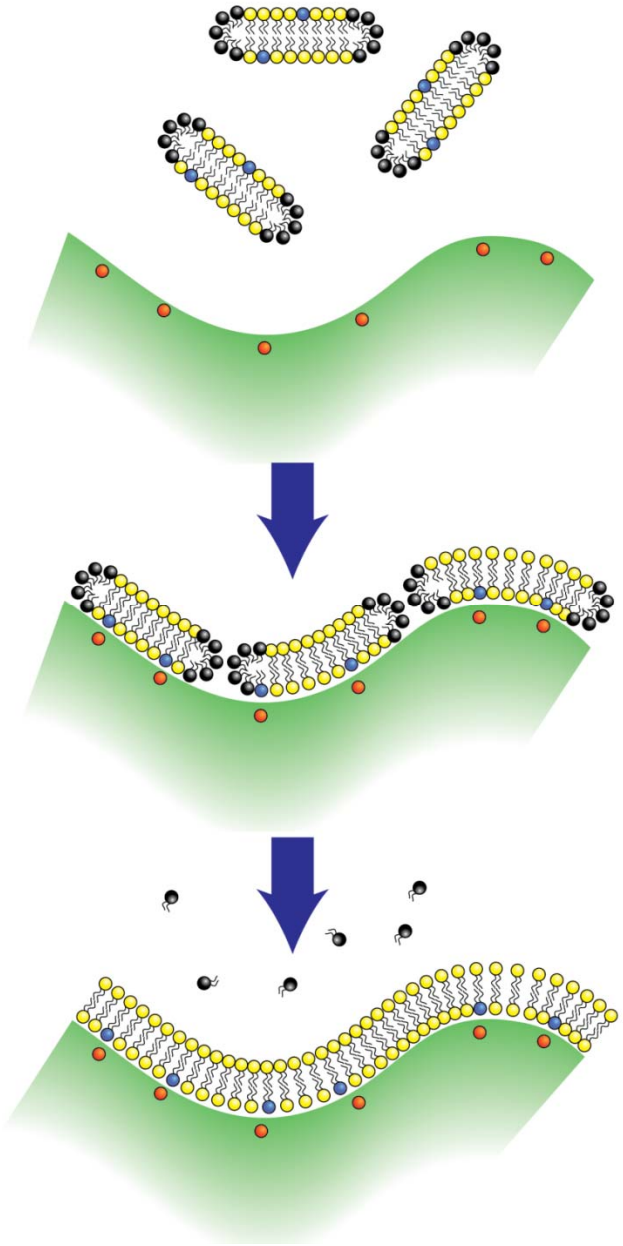

Figure 3-1: Mechanism of formation of Bicellogels from cationic discoidal bicelles binding to anionic core-shell microgels. Top: Cationic bicelles (DMPC-yellow, DHPC-black, DMTAP-blue) are electrostatically attracted to the acrylic acid carboxyls (red) at the surface of the *p*NIPAM microgel (green). Middle: DMTAP migrates from the outer to the inner leaflet of adherent bicelles in order to match cationic-anionic charge densities. Bottom: DHPC exits to the aqueous phase due to its high solubility, forcing fusion of the remaining DMPC/DMTAP lipids into a continuous lipid bilayer, with a shape conforming to the uneven surface of the underlying microgel support.

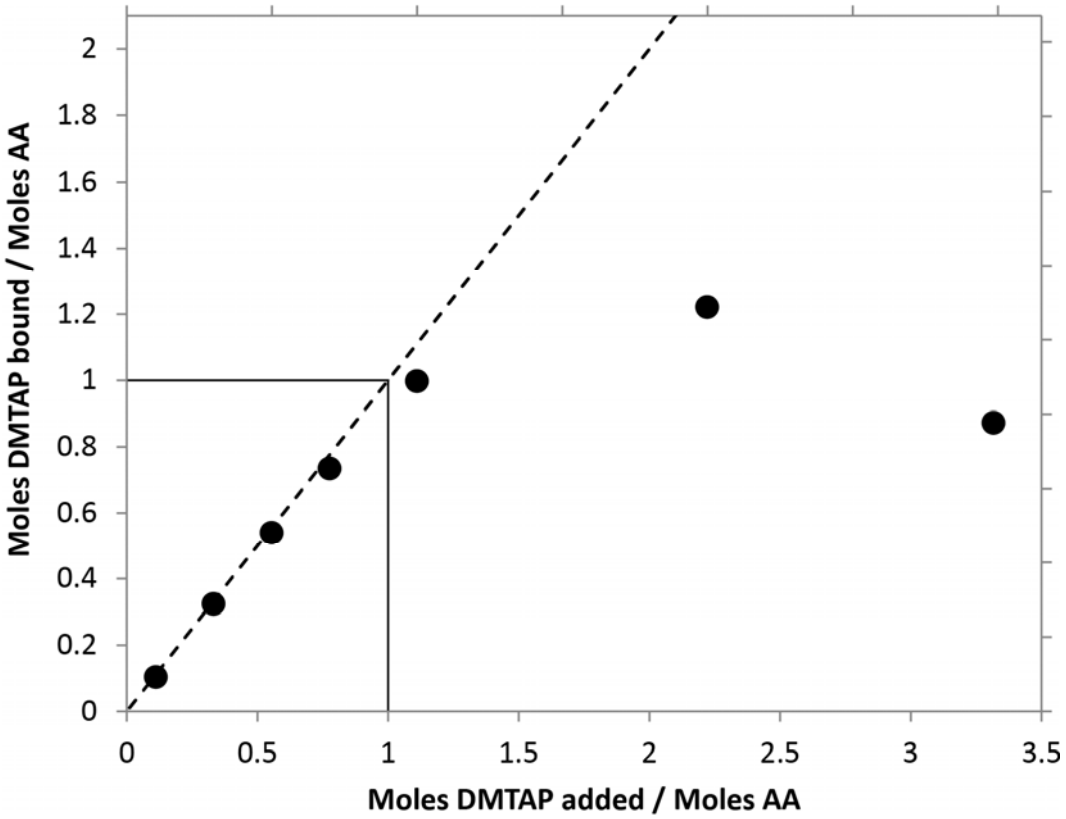

Figure 3-2: Titration of anionic microgels with cationic bicelles. Binding of increasing amounts of q = 2, DMPC/DMTAP 95/5 bicelles to a fixed weight of anionic pNIPAM/p(NIPAM-co-AA) core-shell microgels was quantified via the fluorescence intensity of RhB-PE incorporated into the bicelles. The dotted line indicates quantitative (1:1 charge balance) binding.

3.3.2 DHPC is Absent from the Bicellogel Lipid Bilayer Coating

Static ^{31}P NMR spectroscopy was undertaken to examine in greater detail the properties of the microgel-bound lipids, as shown in Figure 3-3 for Bicellogels at temperatures between 10 °C and 45 °C. At both 10 °C and 20 °C ($T<T_M$ of DMPC), where the Bicellogel lipids presumably exist in a gel phase, broad, axially symmetric powder patterns were observed with a residual chemical shift anisotropy (CSA) of approximately 60 ppm. This is the behaviour expected for phospholipids in a lipid bilayer arrangement where they undergo more-or-less rapid rotations about their long axes, but only slow overall isotropic tumbling due to the size of the self-assembled aggregate, i.e., in this case a micron-sized Bicellogel. At 30 °C ($T>T_M$ of DMPC) an

axially symmetric powder pattern is likewise observed, but with a reduced residual CSA of ~45 ppm characteristic of phosphatidylcholines in a liquid crystalline state. At 45 °C, the residual CSA is reduced yet further. At this temperature, the microgel supporting the lipid bilayer has undergone a VPT and collapsed in size. This can force the lipid bilayer coating to develop protrusions having high curvature.[7] The residual CSA of phospholipids within such regions would be reduced accordingly.

Significantly, there was no evidence of a narrow resonance at the isotropic frequency, indicating that no free bicelles remained present in the sample and, more importantly, suggesting that no DHPC was present either. DHPC generally yields an isotropic resonance due to its tendency to phase separate from DMPC, particularly at temperatures below the DMPC T_M, and its preference for regions of high curvature. For example, the ^{31}P NMR spectrum of DMPC/DHPC bicelles at a temperature just below T_M is a superposition of a DMPC powder pattern and a DHPC isotropic resonance.[13]

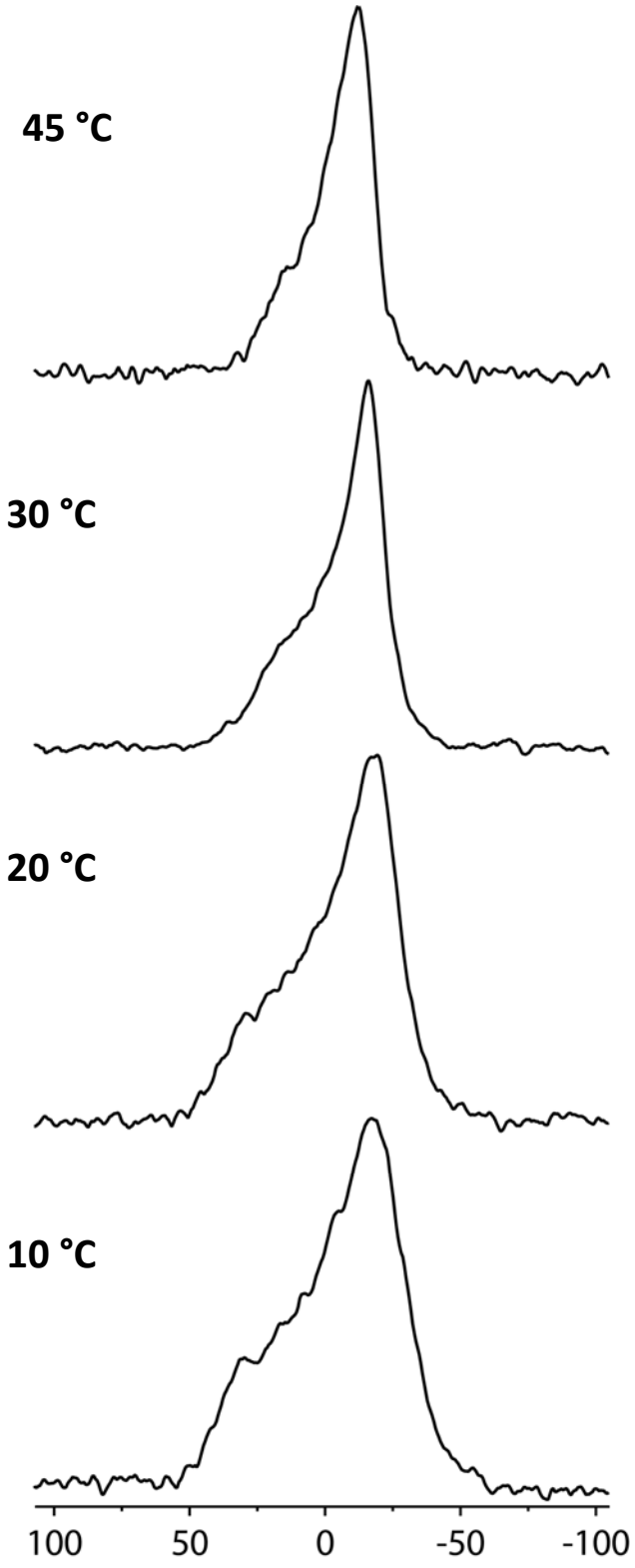

Figure 3-3: Static ^{31}P NMR spectra of Bicellogels at the indicated temperatures. The powder pattern spectral line shapes and residual CSAs are consistent with the presence of a DMPC-rich lipid bilayer coating the microgel surface. The absence of any narrow isotropic resonance suggests the absence of DHPC from the bound lipid fraction.

To more closely examine whether DHPC was present within the Bicellogel lipid bilayer coating, qualitative ESI-MS analysis was undertaken. Since ESI-MS instrumental response increases with decreasing phospholipid acyl chain length,[14] DHPC would be much more sensitively detected than DMPC or DMTAP. Control measurements on equimolar DMPC/DHPC mixtures confirmed that DHPC was more readily detected by ESI-MS than either DMPC or DMTAP. Increased DHPC sensitivity was also confirmed for the case of bicelles of the same composition as employed here, as shown in Figure 3-4A. With regards to the Bicellogels, Figure 3-4B shows the mass spectrum of the Bicellogel lipid bilayer. Although DMTAP (554.49 m/z) and DMPC (678.46 m/z [$M_{DMPC} + H^+$], 700.43 m/z [$M_{DMPC} + Na^+$]) signals were observed, peak(s) related to DHPC were conspicuously absent. Thus, Figure 3-4B indicates that DHPC was entirely absent from the Bicellogel lipid bilayer coating post-fabrication, confirming the interpretation of the ^{31}P NMR spectra in Figure 3-3. Figure 3-4C shows an ESI-MS spectrum of the unbound lipid wash where peaks at 454.26 m/z [$M_{DHPC} + H^+$] and 476.23 m/z [$M_{DHPC} + Na^+$] confirm the presence of DHPC. Evidently, DHPC is removed preferentially during the various washing stages to which the Bicellogels are subjected during fabrication. (Since DHPC is much more sensitively detected in ESI-MS than DMPC, the absence of any DMPC peak in Figure 3-4C does not necessarily mean that no DMPC was present in the wash.) Morigaki et al.[3] in their studies employing POPC/DHPC bicelles to coat glass surfaces also suggested that DHPC was absent from the deposited bilayer since washing the adsorbed bilayer with buffer did not lead to any loss in mass. These authors speculated that this occurred because, at the concentration of bicelles they used, DHPC was below its CMC. However, a chemical analysis of the adsorbed layer was not conducted. The results of our ESI-MS measurements demonstrate unequivocally that DHPC is indeed absent from lipid bilayers deposited from bicelles.

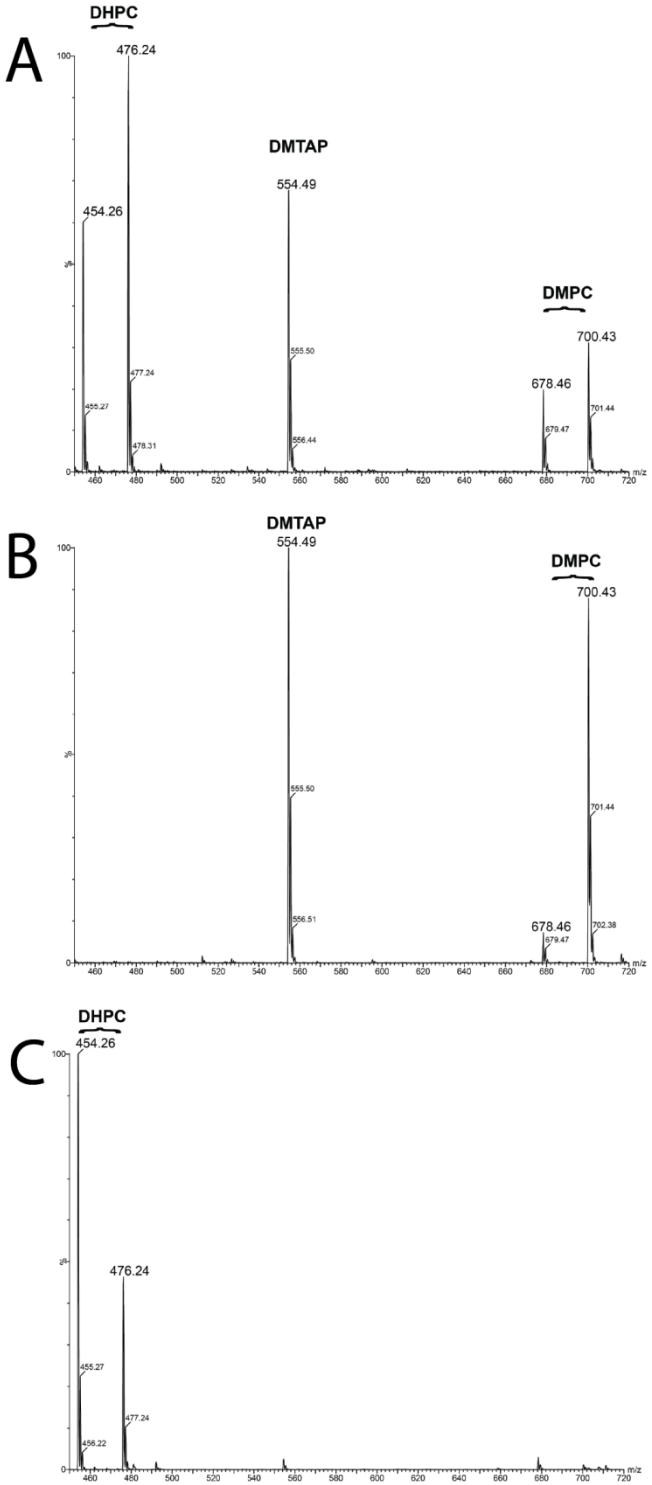

Figure 3-4: ESI-MS spectra for bicelles, Bicellogel bound and unbound lipid fractions. (A) ESI-MS spectrum of bicelles used in this study. DHPC ($M+H^+$=454.26 m/z and $M+Na^+$=476.24 m/z adducts), DMPC ($M+H^+$=678.46 m/z and $M+Na^+$=700.43 m/z adducts) and DMTAP ($M+H^+$=554.49 m/z) were all observed. (B) ESI-MS spectrum of the Bicellogel lipid bilayer. Only DMPC ($M+H^+$=678.46 m/z and $M+Na^+$=700.43 m/z adducts) and DMTAP ($M+H^+$=554.49 m/z) were observed in the bound lipid fraction, while no DHPC was evident. (B) ESI-MS spectrum of the unbound lipid fraction. DHPC ($M+H^+$=454.26 m/z and $M+Na^+$=476.23 m/z adducts) was virtually the sole lipid observed, in contrast to its absence from the bound lipid fraction in (B).

3.3.3 Bicelles Bound at the Microgel Surface Fuse into a Continuous Lipid Bilayer

Using fluorescence imaging, one may demonstrate that cationic bicelle deposition occurs exclusively at or near the surface of the anionic microgels, i.e., at the periphery of the core-shell microgels where the anionic carboxyls are localized. Figure 3-5A shows one such image wherein fluorescence intensity from RhB-PE incorporated into the bicelles remains confined to the periphery of the microgel and is absent from the interior. The near homogenous density of fluorescence intensity around the periphery suggests that defects larger than the diffraction limit do not exist in the deposited layer. In a lightly cross-linked pNIPAM hydrogel matrix, like the core region of our core-shell microgels, pore sizes upwards of 40 Å have been shown to be present.[15] In the more highly cross-linked shell region, one anticipates even smaller pore sizes. Hence, bicelles of diameter 200 Å should be too large to penetrate into the microgel interior, regardless of electrostatic considerations.

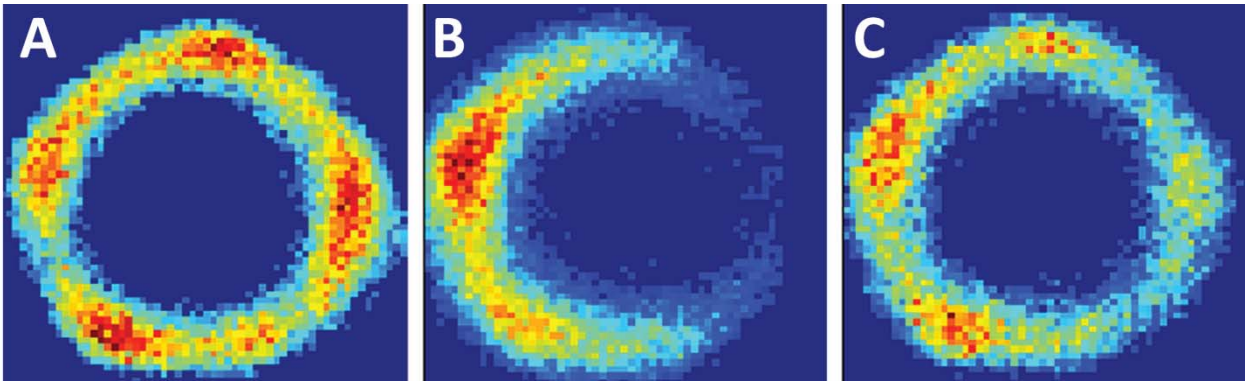

Figure 3-5: FRAP images of RhB-PE-containing Bicellogels measured at 20 °C. Confocal fluorescence microscope images of a 0.05 mol % RhB-E labelled Bicellogel: (A) before photobleaching, (B) immediately after photobleaching, and (C) 5 minutes after photobleaching. The yellow bar represents a size of 1 µm.

To examine whether the bicelles have bound with sufficient density to fuse into a continuous lipid bilayer, FRAP experiments were performed on Bicellogels. Figure 3-5A shows a single Bicellogel imaged prior to photobleaching. In Figure 3-5B, the same Bicellogel is shown

immediately after having been photobleached over a diffraction limited region using a high intensity laser. Figure 3-5C shows that, within a few minutes, fluorescence intensity has returned to the photobleached region. This demonstrates unequivocally that individual bicelles have fused at the microgel surface into a continuous lipid bilayer. Importantly, fluorescence recovery was not observed in FRAP experiments when bicelles and microgels were incubated overnight at a temperature below the T_M of DMPC. Thus bicelle fusion, i.e., transformation from individual discs to continuous lamellae, occurs exclusively above the T_M of the major lipid. In lipid vesicles in general, fusion is more readily induced when the lipids are in the liquid-crystalline phase.[16] However, spontaneous fusion of small DMPC vesicles proceeds maximally in the range 19-24 °C; that is, near or just below the T_M of DMPC.[17] Bicelle fusion, on the other hand, all other factors being equal, is reported to occur only above the T_M of DMPC,[18] in accord with our observations.

To quantify the lateral diffusion of lipids constituting Bicellogels, FRAP curves were measured and analyzed using a bi-exponential model function described by Eq. (1). Figure 3-6A shows the experimental FRAP curve measured for a single Bicellogel prepared at 30 ^{o}C and the corresponding fit to Eq. (1). The two recovery lifetimes determined from the fit were 21.6 ± 1.8 sec (fast fraction) and 200.0 ± 1.6 sec (slow fraction), with the slow fraction contributing 87% of the recovery. A steady state fluorescence recovery of only ~50% was achieved, reflecting the significant fraction of fluorophores initially present within the Bicellogel lipid bilayer that had been photobleached.

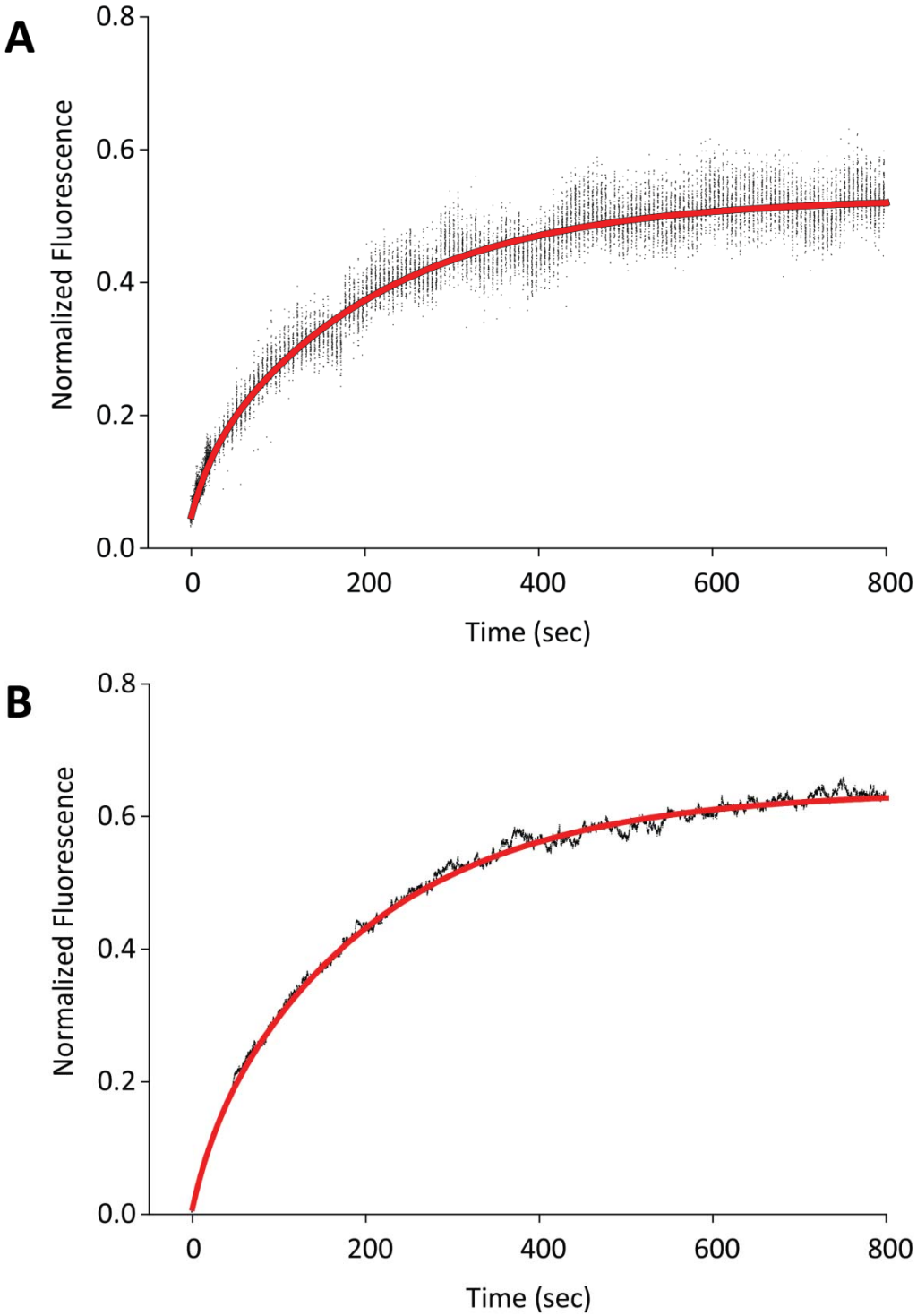

Figure 3-6: Analysis of FRAP curves to extract the lateral diffusion coefficient. (A) Experimental FRAP data (black dots) were fit with a bi-exponential function (red line) as per Eq. (1), with values of the two recovery lifetimes and pre-exponential weighting terms as per the text. (B) Monte Carlo simulations of Bicellogel FRAP data assuming two different lateral diffusion coefficients, weighted as per (A) above. The solid red line shows the fit of Eq. (1) to the simulated recovery curves using populations identical to those obtained from experimental data in (A).

In the absence of an analytical expression describing lateral diffusion around a sphere possessing the properties of a Bicellogel, we resorted to Monte Carlo simulations to extract lateral diffusion coefficients from the FRAP curves. For example, the Monte-Carlo simulated FRAP curve shown in Figure 3-6B was obtained assuming two populations of lipids with lateral diffusion coefficients of 5 x 10^{-10} cm^2s^{-1} (13%) and 3 x 10^{-11} cm^2s^{-1} (87%), with percent contributions as indicated in parentheses. The best fit of Eq. (1) to the Monte-Carlo simulated FRAP curve, likewise shown in Figure 3-6B, yielded recovery lifetimes of 23.5 ± 0.8 sec and 200.0 ± 0.8 sec, i.e., close to the recovery lifetimes observed experimentally. The lateral diffusion coefficients extracted in this fashion, averaged over four separate Bicellogels, were (4.3 ± 2.2) x 10^{-10} cm^2s^{-1} and (2.9 ± 0.6) x 10^{-11} cm^2s^{-1} with the slower fraction contributing 77.7 ± 8.7 % of the recovery.

DMPC lipid bilayers exhibit lateral diffusion coefficients on the order of ~10^{-10} cm^2s^{-1} at temperatures below the T_M of 24 °C.[19] Since the FRAP measurements were taken at 20 °C, the Bicellogel lipid bilayer should be in the gel phase and the lipid population having a diffusion coefficient of (4.3 ± 2.2) x 10^{-10} cm^2s^{-1} would appear to conform to this expectation. However, the overwhelming majority of the lipids displayed a lateral diffusion coefficient slower by an order of magnitude. Some SLBs exhibit two roughly equal lipid populations with differing lateral diffusion properties and this is generally attributed to friction between the inner bilayer leaflet and the underlying support that is absent from the outer leaflet.[20,21] Even if the bilayer is separated from the support by spacer groups, these immobile anchors can introduce a "picket fence"-type frictional barrier within the inner leaflet.[7,22] In Bicellogels, the anchoring is via electrostatic interactions, which may or may not produce less frictional drag than an immobile covalently-attached anchor. However, since the majority of the Bicellogel lipid

population exhibits this slow lateral diffusion, an explanation involving both the inner and outer bilayer leaflets must be sought. If the microgel-bound lipid bilayer is highly corrugated, then the observed lateral diffusion will be an average over multiple undulations and will be much slower than that measured for a corresponding smooth lipid bilayer.

3.3.4 Permeability of Bicellogel Lipid Bilayers

If the Bicellogel lipid bilayer coating is highly corrugated, then the permeability barrier properties of that membrane coating may be compromised. To explore this point, NBD-PE fluorescence quenching by sodium dithionite was examined. In the case of an LUV with an intact lipid bilayer, dithionite ions added externally will not permeate to the interior compartment. Thus, as shown in Figure 3-7A, for the case of LUV composed of 95/5 DMPC/DMTAP addition of sodium dithionite results in roughly 50% reduction in NBD-PE fluorescence. On the other hand, for q=2 discoidal bicelles of composition identical to those employed here for Bicellogel fabrication, added dithionite will have access to both faces of the bicellar disc, resulting in 100% quenching of NBD-PE fluorescence as likewise shown in Figure 3-7A.

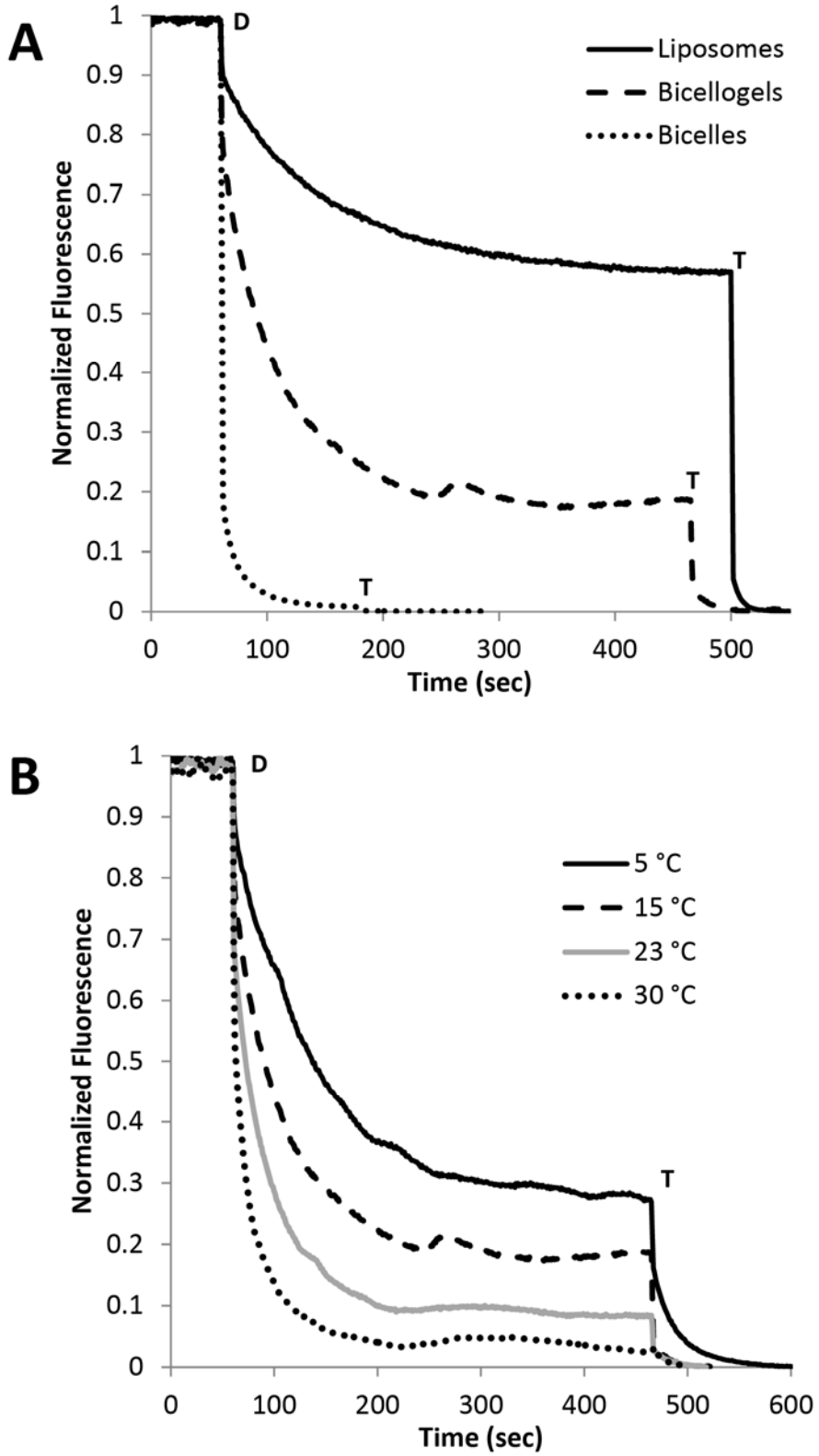

Figure 3-7: Sodium dithionite induced NBD-PE quenching experiments. (A) Dithionite NBD-PE quenching of 95/5 DMPC/DMTAP LUV (solid line), Bicellogels (dashed line) and bicelles (dotted line) at 15 °C. (B) Sodium dithionite induced NBD-PE quenching assay on 95/5 DMPC/DMTAP Bicellogels at different temperatures. D and T denote the times of external addition of dithionite and Triton, respectively.

When Bicellogel permeability was interrogated in the same fashion, dithionite quenching was significantly greater than with corresponding liposomes. As Figure 3-7A shows, NBD-PE fluorescence decreased by ~80% upon dithionite addition, confirming that a significant amount of NBD-PE was accessible to the dithionite ion. Furthermore, as Figure 3-7B shows, dithionite quenching of NBD-PE fluorescence increased markedly with increasing temperature. Bicellogels were least permeable to dithionite at 5 °C and 15 °C, while at temperatures at or above the DMPC T_M, essentially all of the Bicellogel lipids were accessible to dithionite. Interestingly, permeability of DMPC/DMTAP LUV exhibited a similar temperature-dependent increase, although remaining completely impermeable at temperatures below the DMPC T_M. This suggests that the increased permeability of the Bicellogel lipid bilayer is not the result of static, permanent defects, since these would be predicted to persist regardless of the bilayer thermotropic phase. Rather, the temperature dependence of the permeability seems to indicate the presence of dynamic defects smaller than the diffraction limit of our microscope, such as might result from regions of high local curvature. As we have argued above based on lipid binding data (Figure 3-2) and FRAP lateral diffusion measurements (Figure 3-6), the lipid bilayer deposited on these microgels is likely highly corrugated due to the uneven surface of the underlying microgel support. Moreover, the microgel polymer chains are to some considerable degree mobile despite being cross-linked. The regions of high dynamic membrane curvature brought on by all of those factors would surely challenge the permeability barrier properties of the bilayer, similar to the effects of fatty acids and lysolipids.[23] Confirming the presence of such dynamic undulations within the adherent lipid bilayer would require a non-perturbing technique with high spatial and temporal resolution. The nm level resolution provided by Atomic Force Microscopy (AFM) would be one such candidate, but the low scan

rates currently available might not resolve the presumably fast dynamics that are of interest here.[24] However, emerging fast-scan AFM techniques capable of elucidating phenomenon on the sub-100 ms timescale might prove useful in this regard.[24,25]

Increased permeability is a general concern with SLBs. Perturbations by the underlying supporting surface are often implicated in the bilayer's increased permeability. Nollert et al.[26] found that an intact POPC lipid bilayer deposited on a hard glass surface (planar or spherical) was freely permeable to dithionite ions, an effect attributed to surface roughness. Ng et al.[22] found that coating soft hydrophobically-modified dimethacrylamide beads with eggPC resulted in a continuous bilayer that was almost completely permeable to cobalt ions, in contrast to the impermeability of eggPC liposomes. It was proposed that the stress experienced by the bilayer when in close proximity to the dynamic, possibly highly corrugated, surface of the bead was the origin of the increased permeability.

3.3.5 Mechanism of Bicellogel Formation

The mechanism of Bicellogel formation via electrostatic attraction of bicelles, as deduced from the experiments described here, is summarized in Figure 3-1. The initial interaction is electrostatic attraction from a distance between cationic bicelles and the anionic microgel surface. At close approach, the mobile cationic amphiphiles can migrate around the bicelle rim from the outer bicelle face to the inner in order to balance the local charge density of immobile polymeric anionic charges. Washing these electrostatic complexes preferentially removes the neutral and highly water-soluble short-chain species DHPC. Elimination of DHPC forces fusion of bicelles into larger, unilamellar structures, as the self-assemblies seek to minimize edge regions formerly occupied by DHPC. Provided a sufficient density of surface-

bound bicelles had been attained initially, and provided the lipids are in the liquid-crystalline state, fusion occurs and begets a continuous unilamellar lipid bilayer surrounding, and closely conforming to, the entire microgel surface. Since that surface is highly convoluted, the resulting bilayer is locally highly curved. The resulting bending energy stress this imposes can compromise the permeability barrier properties of the lipid bilayer.

3.4 Conclusions

A novel method for the deposition of a lipid bilayer onto a soft polymer surface starting from discoidal bicelles has been described. Deposition was mediated by electrostatic attraction between negatively-charged core-shell hydrogel spheres bearing acrylic acid groups in the shell regions and positively-charged DMTAP-doped bicelles. Saturation of bicelle deposition at the microgel surface occurred upon charge balance being achieved. DHPC, the short chain amphiphile necessary to bicelle formation, was absent from the microgel surface-deposited lipids, presumably due to its greater water solubility upon dilution/washing. At a temperature above the gel-to-liquid-crystalline phase transition the remaining DMPC/DMTAP surface-deposited lipids fused into a continuous lipid bilayer entirely encapsulating the microgel sphere. This lipid bilayer was highly permeable to small molecules due, in all likelihood, to curvature stress from adapting to the rough surface of the microgel.

3.5 References

(1) R. Zeineldin, J. A. Last, A. L. Slade, L. K. Ista, P. Bisong, M. J. O'Brien, S. R. J. Brueck, D. Y. Sasaki, and G. P. Lopez, *Langmuir*, 2006, **22**, 8163–8168.

(2) S. R. Tabaei, P. Jönsson, M. Brändén, and F. Höök, *J. Struct. Biol.*, 2009, **168**, 200–206.

(3) K. Morigaki, S. Kimura, K. Okada, T. Kawasaki, and K. Kawasaki, *Langmuir*, 2012, **28**, 9649–9655.

(4) J. Wilschut, N. Duzgunes, D. Hoekstra, and D. Papahadjopoulos, *Biochemistry*, 1985, **24**, 8–14.

(5) G. Csúcs and J. J. Ramsden, *Biochim. Biophys. Acta, Biomembr.*, 1998, **1369**, 61–70.

(6) B. Seantier and B. Kasemo, *Langmuir*, 2009, **25**, 5767–5772.

(7) Q. Saleem, B. Liu, C. C. Gradinaru, and P. M. Macdonald, *Biomacromolecules*, 2011, **12**, 2364–2374.

(8) K. Sugihara, B. Jang, M. Schneider, J. Vörös, and T. Zambelli, *Soft Matter*, 2012, **8**, 5525–5531.

(9) M. Kaufmann, Y. Jia, C. Werner, and T. Pompe, *Langmuir*, 2011, **27**, 513–516.

(10) J. Majewski, J. Y. Wong, C. K. Park, M. Seitz, J. N. Israelachvili, and G. S. Smith, *Biophys. J.*, 1998, **75**, 2363–2367.

(11) I. Reviakine and A. Brisson, *Langmuir*, 2000, **16**, 1806–1815.

(12) B.-B. Lucyanna, R. Gelen, C. Merce, R. Laia, L.-I. Carmen, D. la M. Alfons, and L. Olga, *Pharmaceutics*, 2011, **3**, 636–664.

(13) P. M. Macdonald and R. Soong, *Can. J. Chem.*, 2011, **89**, 1021–1035.

(14) M. Koivusalo, P. Haimi, L. Heikinheimo, R. Kostiainen, and P. Somerharju, *J. Lipid Res.*, 2001, **42**, 663–672.

(15) Q. Yan and A. S. Hoffman, *Polymer*, 1995, **36**, 887–889.

(16) D. Papahadjopoulos, G. Poste, B. E. Schaeffer, and W. J. Vail, *Biochim. Biophys. Acta, Biomembr.*, 1974, **352**, 10–28.

(17) J. H. Prestegard and B. Fellmeth, *Biochemistry*, 1974, **13**, 1122–1126.

(18) M. P. Nieh, V. A. Raghunathan, S. R. Kline, T. A. Harroun, C. Y. Huang, J. Pencer, and J. Katsaras, *Langmuir*, 2005, **21**, 6656–6661.

(19) P. F. Fahey and W. W. Webb, *Biochemistry*, 1978, **17**, 3046–3053.

(20) M. Hetzer, S. Heinz, S. Grage, and T. M. Bayerl, *Langmuir*, 1998, **14**, 982–984.

(21) C. Scomparin, S. Lecuyer, M. Ferreira, T. Charitat, and B. Tinland, *Eur. Phys. J. E*, 2009, **28**, 211–220.

(22) C. C. Ng, Y. Cheng, and P. S. Pennefather, *Biophys. J.*, 2004, **87**, 323–331.

(23) O. G. Mouritsen, *Eur. J. Lipid Sci. Technol.*, 2011, **113**, 1174–1187.

(24) L. Picas, P.-E. Milhiet, and J. Hernández-Borrell, *Chem. Phys. Lipids*, 2012, **165**, 845–860.

(25) T. Uchihashi, N. Kodera, and T. Ando, *Nat. Protocols*, 2012, **7**, 1193–1206.

(26) P. Nollert, H. Kiefer, and F. Jahnig, *Biophys. J.*, 1995, **69**, 1447–1455.

Liposome-Coated Hydrogel Spheres: Delivery Vehicles with Tandem Release from Distinct Compartments

4.1 Introduction

Dual drug delivery systems are of growing interest since combinations of drugs with different therapeutic effects can be advantageous in the treatment of many diseases including diabetes[1], cancer[2], rheumatoid arthritis[3] and a host of others. Dual drug delivery systems guarantee co-localization of the two drugs, which is pivotal to achieving the desired therapeutic enhancement. If injected separately, in contrast, their potentially differing pharmacokinetics and the dilution upon systemic injection reduces the likelihood that the two agents will concentrate equally, both spatially and temporally, at the desired site. The simplest dual drug delivery systems consist of a single phase particle entrapping both agents of interest.[4,5] These are limited, however, to agents which are mutually inert and have fundamentally different properties, e.g., size and/or hydrophobicity, in order to attain different release profiles. Dual compartment delivery systems can eliminate such constraints on cargo choice and release control. A number of different dual compartment systems have been reported. Examples include polypeptide micelles as a hydrophobic reservoir combined with microporous glass[6] or a hydrogel particle[7] as a hydrophilic reservoir, hollow core-shell polymer particles where the core functions as a hydrophilic reservoir and the shell as a hydrophobic reservoir[8], and polymer beads which adsorb one type of drug embedded in a polymer sphere which adsorbs another type of drug[9]. In most such dual delivery systems, simultaneous release is readily achieved, while controlled tandem release of the two drugs is a significant challenge.

Hydrogel-liposome complexes have particular potential as dual-drug delivery vehicles in that they provide co-localized but separate compartments able to accommodate potentially

any combination of cargos. Here we describe the preparation and properties of lipid bilayer vesicle-coated coated pNIPAM hydrogel spheres (VESCOgels) intended to function as a dual drug delivery system. The liposomes are coupled to the microgel via a carbodiimide-mediated reaction between amine-bearing hydrophobes intercalated within the liposomal lipid bilayer and surface carboxyls within the shell region of core-shell pNIPAM microgel particles. We demonstrate that such VESCOgels exhibit dual release kinetics characterised by fast release of microgel-trapped species and slow release of liposome-trapped species. It is envisioned that VESCOgels will be useful, therefore, in applications requiring temporally-controlled drug delivery.

4.2 Materials and Methods

4.2.1 Materials

Jeffamine EDR-148 was a kind gift from Huntsman International (The Woodlands, TX). POPC and NBD-PE were purchased from Avanti Polar Lipids (Alabaster, AL). RhB-PE was purchased from Invitrogen (Carlsbad, CA). All other reagents were purchased from Sigma Aldrich (Oakville, ON). All reagents were used as received, without further purification. Water used in all of the experiments was of MilliQ grade.

4.2.2 Synthesis of pNIPAM/p(NIPAM-co-AA) Core–Shell Microgels

The pNIPAM/p(NIPAM-*co*-AA) core-shell microgels were synthesized as detailed in Chapter 2.

4.2.3 AECHO Synthesis

3-O (2-aminoethoxyethyloxyethyl)carbamyl cholesterol (AECHO) (see Figure 4-1) was synthesized by reacting the *bis*-amine compound (ethylenedioxy)bis(ethylamine), trade name Jeffamine EDR-148, with cholesteryl chloroformate. EDR-148 (5.0147 g) was charged into a 20 ml vial to which cholesteryl chloroformate (1.0086 g), dissolved in 10 ml of chloroform, was added via a syringe pump at a rate of 0.4 ml/minute under stirring. The reaction was allowed to proceed overnight at room temperature. The reaction mixture was taken up in 50 ml of dichloromethane (DCM) and washed five times with 10 ml portions of H_2O to remove unreacted EDR-148. After drying the DCM layer with $MgSO_4$ and removing the solvent by rotary evaporation, 70 ml of boiling methanol was added, causing the immediate precipitation of any *bis*-cholesterol side product. The suspension was then kept at 4°C for one hour before filtration to remove the *bis*-cholesterol precipitate. Methanol was removed via rotoevaporation and the residue was stored under vacuum until finally being lyophilized to yield 0.9 g (71% yield) of AECHO as a gummy paste.

^{1}H NMR (500 MHz, $CDCl_3$) δ 5.30 (d, *J* = 5.2 Hz, 1H), 3.55 (s, 4H), 3.47 (dt, *J* = 20.4, 5.3 Hz, 5H), 3.32 – 3.26 (m, 2H), 2.82 (d, *J* = 5.6 Hz, 2H), 2.29 (dd, *J* = 13.3, 4.7 Hz, 1H), 1.92 (dd, *J* = 23.1, 14.7 Hz, 2H), 1.80 (t, *J* = 16.1 Hz, 3H), 1.52 – 1.16 (m, 17H), 1.12 – 0.77 (m, 28H), 0.61 (s, 3H).

^{13}C NMR (126 MHz, $CDCl_3$) δ 156.05, 139.65, 122.23, 74.01, 73.29, 70.07, 70.02, 69.95, 56.49, 55.95, 49.82, 42.11, 41.56, 40.47, 39.55, 39.33, 38.42, 36.82, 36.36, 36.00, 35.60, 31.71, 31.68, 28.05, 28.01, 27.80, 24.10, 23.65, 22.65, 22.39, 20.86, 19.15, 18.54, 11.68.

HRMS (ESI+) (M+H): Calculated = 561.46, Found = 561.44

4.2.4 Liposome Preparation

AECHO-containing large unilamellar vesicles (AECHO-LUVs), composition 95/5 POPC/AECHO mol/mol, were produced by first co-dissolving appropriate amounts of the respective lipids in chloroform, removing the solvent under nitrogen and storing the resulting lipid film under vacuum to eliminate final solvent traces. When desired, 0.1 mol % NBD-PE or 0.05 mol % RhB-PE was incorporated by adding appropriate aliquots of their respective chloroform stock solutions to the chloroform mixture. The lipid film was hydrated to 10 mg lipid per ml with 10 mM phosphate buffer (PB) (pH 7.4) and subjected to three cycles of freeze-thaw-vortex by cycling between liquid N_2 and a 60°C water bath. The resulting multilamellar vesicles were then extruded 25 times through 0.1 µm polycarbonate membranes using a handheld extruder (Avanti Polar Lipids, Alabaster, AL). The AECHO-LUVs so produced were kept at 4 °C until use. DLS size measurements on the extruded vesicles yielded a mean diameter of 103 nm and narrow polydispersity (PDI =0.048).

4.2.5 AECHO-LUV Tethering to Microgels

Carboxylate groups of pNIPAM/p(NIPAM-*co*-AA) core-shell microgels were pre-activated with NHS as follows. Typically, 24 µL of a 21 mg/ml aqueous solution of microgels was added to a 976 µL solution of 17 mM 1-ethyl-3-(3-dimethylaminopropyl)carbodiimide (EDAC) and 14 mM *N*-hydroxysuccinimide (NHS) in 0.1 M MES buffer (pH 5.5). The contents were stirred for 30 minutes. Due to the high concentration of EDAC/NHS used, NHS activation was considered quantitative and complete in 30 minutes. The NHS-activated microgels were washed three times with the same MES buffer and re-suspended in 10 mM PB or 20 mM HEPES buffer, depending on the experiment. 2 mg of AECHO-LUVs were added and permitted to react

overnight. The resulting VESCOgels were isolated by centrifugation at 6k RPM for 5 minutes and the pellet was re-suspended in phosphate buffered saline (PBS) (100 mM KCl, 10 mM phosphate, pH 7.4). This centrifugation/re-suspension cycle was repeated at least 2 more times.

4.2.6 DLS and zeta potential measurements

A Malvern Zetasizer NanoZS (Malvern Instruments Ltd., Worcestershire, UK) was used to record mean size, polydispersity (PDI) and zeta potential. The solvent parameters for the buffer were generated using the NanoZS software and size calibration beads were used to confirm accuracy. A plastic cuvette was used for all DLS measurements while a disposable folded capillary cell was used to measure zeta potential.

4.2.7 Liposome Binding Assay

Liposome binding as a function of increasing number of liposomes added to a constant number of NHS-activated microgels was quantified from the fluorescence intensity of 0.05 mol % RhB-PE incorporated into the liposomal lipids. Typically, 0.5 mg of NHS-activated microgels were mixed with the desired amount of AECHO-LUVs (0.05, 0.1, 0.25, 0.5, 0.75 and 1.00 mg) to a total volume of 1.0 ml, and incubated for 1 hr, followed by a series of centrifugations / washes with 1.0 ml PBS, each of which was set aside for analysis. Finally, the VESCOgel pellet itself was stripped of bound AECHO-LUVs by addition of 1.0 ml of 0.2 M sodium cholate, with centrifugation to separate the microgel from the solubilised lipids. Fluorescence intensities were recorded using a Tecan Infinite M1000 PRO microplate reader (Männedorf, Switzerland) via a Corning 96 well round bottom transparent microplate. Into each well, a 30 µL aliquot of a given solution was transferred followed by 70 µL of 0.2 M sodium cholate. The wells were

excited at 550 nm and a scan was performed from 560 to 600 nm with the same gain used for all samples. 50 flashes were used at a frequency of 400 Hz, with an integration time of 20 µs. The spectrum of a control well containing 30 µL of PBS and 70 µL of 0.2 M sodium cholate was subtracted from that of each sample well. A calibration curve was created using 0.05, 0.5 and 1.0 mg/ml of AECHO-LUVs to confirm the linearity of the fluorescence response and to permit quantification of the lipid concentration in a given sample.

4.2.8 Lamellarity Assay

An NBD quenching by sodium dithionite lamellarity assay was conducted as described previously in Chapter 2, here using either 0.05 mg of VESCOgels or 0.2 mg of AECHO-LUVs in PBS.

4.2.9 Fluorescence Imaging

Fluorescence imaging was carried out on VESCOgels assembled from AECHO-LUVs with entrapped 0.1 mM RhB and microgels with entrapped FS. Diluted VESCOgel samples were applied to a plasma-cleaned coverslip and allowed to incubate for 10 minutes at 20°C. Fluorescence images were acquired using a custom-built inverted wide-field microscope. Basically, VESCOgel samples were illuminated by two solid state lasers at 473nm (Cobolt Blues, Cobolt, Sweden) and 532nm (Laserglow Technologies, Canada) alternatively controlled by an acousto optic tunable filter (Gooch & Housego, USA). Excitation and emission signals were passed through an identical oil immersion TIRF objective (1.45NA/60X Plan-Apochromat, Olympus, USA). Fluorescence emission was passed through a quad-edge laser-flat dichroic beamsplitter (405/488/532/635 nm, Semrock, USA), and long-pass (BLP01-488 , BLP01-532 ,

Semrock, USA) and band-pass filters (HQ530/50, HQ600/80, Chroma, USA) to remove scattering and cross-talk signal. The dual color fluorescent images were taken by a cooled electron-multiplied charge-coupled device (EMCCD, DU-897BV, Andor, USA) at an exposure rate of 10 Hz.

4.2.10 Fluorescence Recovery After Photobleaching

FRAP experiments were carried out on 0.05 mol % RhB-PE containing VESCOgels absorbed on a plasma-cleaned coverslip using a custom-built inverted confocal microscope described in Chapter 2, with minor differences. Briefly, a 1.4NA/100X Plan-Apochromat microscope oil immersion objective (Carl Zeiss, Canada) was employed to focus the 532 nm laser excitation light (Laserglow Technologies, Canada) onto the sample which was incubated on the plasma-cleaned coverslip for about 10 minutes at 20^{o}C. The coverslip was placed on a three-axis piezo scanner (T225, MadCity Lab, USA) to control the position and focus depth into the liquid sample. The laser scanning procedure was performed under low laser excitation intensity (~1 W/cm^2) to prevent undesired photobleaching of fluorescent lipids. Fluorescence signals were collected by the same objective and passed through a dichroic (D01-532RS, Semrock, USA), long-pass (LP03-532RS, Semrock, USA) and band-pass (HQ60/80, Chroma, USA) optical filters, and a 50 μm pinhole (Thorlabs, USA) to avoid scattering and remove out-of-focus fluorescence signal contributions. The actual fluorescence signals were focused on a single photon avalanche diode (MPD-SPAD, PD5CTC, Optoelectronic Components, Canada), which was connected to one port of a PicoHarp300 single photon counting module (PicoQuant, Germany). Focus was adjusted close to the equator of each VESCOgel in this experiment in order to examine the photobleaching and recovery phenomena clearly. A photobleaching spot on a VESCOgel was chosen arbitrarily and focused by high laser intensity (~ 500 W/cm^2) for about 2

seconds. Fluorescence images of the same VESCOgel were taken immediately and after 10 minutes, both under low laser excitation intensity (~ 1 W/cm^2) to monitor the fluorescence recovery behavior. At least 3 VESCOgels were interrogated in this manner.

4.2.11 Release Assay

Release kinetics of liposomal and microgel matrix contents were measured separately with distinct assays. Liposomal contents release was monitored via the fluorescence of calcein. The non-fluorescent cobalt-calcein complex was entrapped within liposomes and the membrane impermeable cobalt complexer ethylene glycol tetraacetic acid (EGTA) was added to the external solution. Any leakage of cobalt-calcein results in EGTA binding of cobalt and the liberation of the highly fluorescent free calcein species. AECHO-LUVs entrapping cobalt-calcein were prepared by hydrating a lipid film in a solution containing 10 mM cobalt-calcein, 20 mM HEPES (pH 7.2). Subsequent to the liposome preparation protocol described above, the AECHO-LUVs were passed through a Sephadex G-50 column to remove external cobalt-calcein. These AECHO-LUVs with entrapped cobalt-calcein were then coated to NHS-activated microgels as described above.

Cobalt-calcein release as a function of time was measured on 20 µL aliquots of these suspensions diluted with 1980 µL of 100 mM KCl, 20 mM HEPES (pH 8.0). The fluorescence signal was monitored over time using a Quanta Master PTI spectrofluorimeter (Photon Technology International, Lawrenceville, NJ) equipped with an OD 1.0 filter at the excitation monochromator and FelixGX software. Temperature was controlled at 23°C using a Quantum Northwest TC 125 temperature controller (Liberty Lake, WA). Excitation was fixed at 490 nm and emission at 515 nm was monitored over several minutes at the rate of 1 point/sec. Once a

stable fluorescence emission signal was obtained from the VESCOgels, 20 µL of 1 M EGTA, 0.5 M Tris (pH 8.0) was added and the emission signal was further monitored until stability was again attained. Finally, 20 µL of 5 wt% Triton X-100 (Triton) was added to solubilise all lipids and release all cobalt-calcein from the liposomes. The cobalt-calcein released during a specified time period (t) was determined by the following equation:

$$\%\ leaked\ (t) = \left(\frac{Fluorescence\ before\ Triton\ (t)}{Fluorescence\ after\ Triton\ (t)} - \frac{Fluorescence\ before\ Triton(0)}{Fluorescence\ after\ Triton\ (0)}\right) * 100\% \qquad \text{Equation 17}$$

To determine release from the microgel matrix of VESCOgels, sodium fluorescein (FS) was loaded into the microgels by adding 50 µL of 10 mM FS simultaneously with the AECHO-LUVs during the AECHO-LUV coupling step. The simultaneous AECHOL-LUV coupling and FS loading was permitted to continue overnight. Excess LUVs and FS were removed by six cycles of centrifugation / washing as above, each cycle requiring roughly three minutes to complete. At a specified time subsequent to the last wash, an aliquot was removed, centrifuged, and the resulting supernatant was set aside for fluorescence analysis. A 20 µL aliquot of given supernatant was placed in a well of a Corning 96 well round bottom transparent microplate along with 180 µL of 1 M NaOH in order to achieve a high pH and, hence, produce the maximum quantum yield from FS. Fluorescence readings were recorded using a Tecan Infinite M1000 PRO microplate reader (Männedorf, Switzerland). The wells were excited at 470 nm and an emission scan was performed between 500 and 550 nm with the same gain used for all samples. 50 flashes were used at a frequency of 400 Hz, with an integration time of 20 µs and a settle time of 50 ms. The temperature was kept at 24°C. A control spectrum obtained with 20 µl of buffer and 180 uL of 1 M NaOH was subtracted from each experimental spectrum. The

amount of FS released from the VESCOgels at a specified time (t) was determined by the equation:

$$\%\ FS\ released\ (t) = \frac{\sum_0^t Fluorescence\ (t)}{Total\ Fluorescence} * 100\% \qquad \text{Equation 18}$$

where "Total Fluorescence" was obtained from a saved sample at time zero prior to any release kinetic measurements.

4.3 Results and Discussion

4.3.1 Fabrication of VESCOgels

A principal goal of this research was to fabricate liposome-hydrogel complexes "on-demand" using a minimum number of steps in proceeding from separate liposomes and microgels to complexes of the two. The approach chosen was to hydrophobically-anchor one of the mutually reactive chemical species to the liposome surface and to expose such liposomes to microgels bearing the complimentary reactive species at their surfaces. While the general approach is independent of the specific chemistry of interaction, here we employ conventional carbodiimide chemistry to demonstrate the principle for the case of amine-bearing liposomes reacting with carboxyl-bearing microgels.

To prepare liposomal surface-displayed amines, we designed an amine-modified cholesterol moiety, AECHO (see Figure 4-1 with the intention that the hydrophobic cholesterol group would intercalate into the lipid bilayer and anchor the hydrophilic amine substituent at the liposome surface. Cholesterol is an optimal choice as a hydrophobic anchor because it readily intercalates into lipid bilayers and, upon doing so, enhances bilayer stability: hence its

ubiquitous use in liposomal formulations. AECHO was readily synthesized in a single step, under mild conditions, in high yield, from commercially-available precursors and was simple to separate from excess starting material and side products. AECHO contains two flexible, hydrophilic ethylene oxide spacer units separating the surface-exposed primary amine and the rigid, hydrophobic cholesterol ring. The role of these spacers is to alleviate steric constraints encountered when a large liposome approaches the rough microgel surface. Indeed, we observed that LUVs incorporating 5 mol % 1-palmitoyl-2-oleoyl-*sn*-glycero-3-phosphoethanolamine, an amine terminated phospholipid lacking such a spacer, could not be immobilized to the microgel surface, probably due to the aforementioned steric constraints.

The microgel target for liposome binding consisted of core-shell pNIPAM/p(NIPAM-*co*-AA) microgels, prepared such that only the periphery of the microgel spheres contain carboxyl groups. As illustrated in Figure 4-2, the microgel carboxyls were activated with conventional EDAC/NHS carbodiimide chemistry immediately prior to exposure to amine–bearing liposomes in order to avoid hydrolyzation of NHS esters during storage in aqueous solution.[12] Alternately, pNIPAM could have been co-polymerized with NHS-acrylates, as has been reported for non-aqueous solvents,[13,14] but for our purposes this would have required eventual solvent exchange into water, thus re-introducing the NHS hydrolyzation issue.

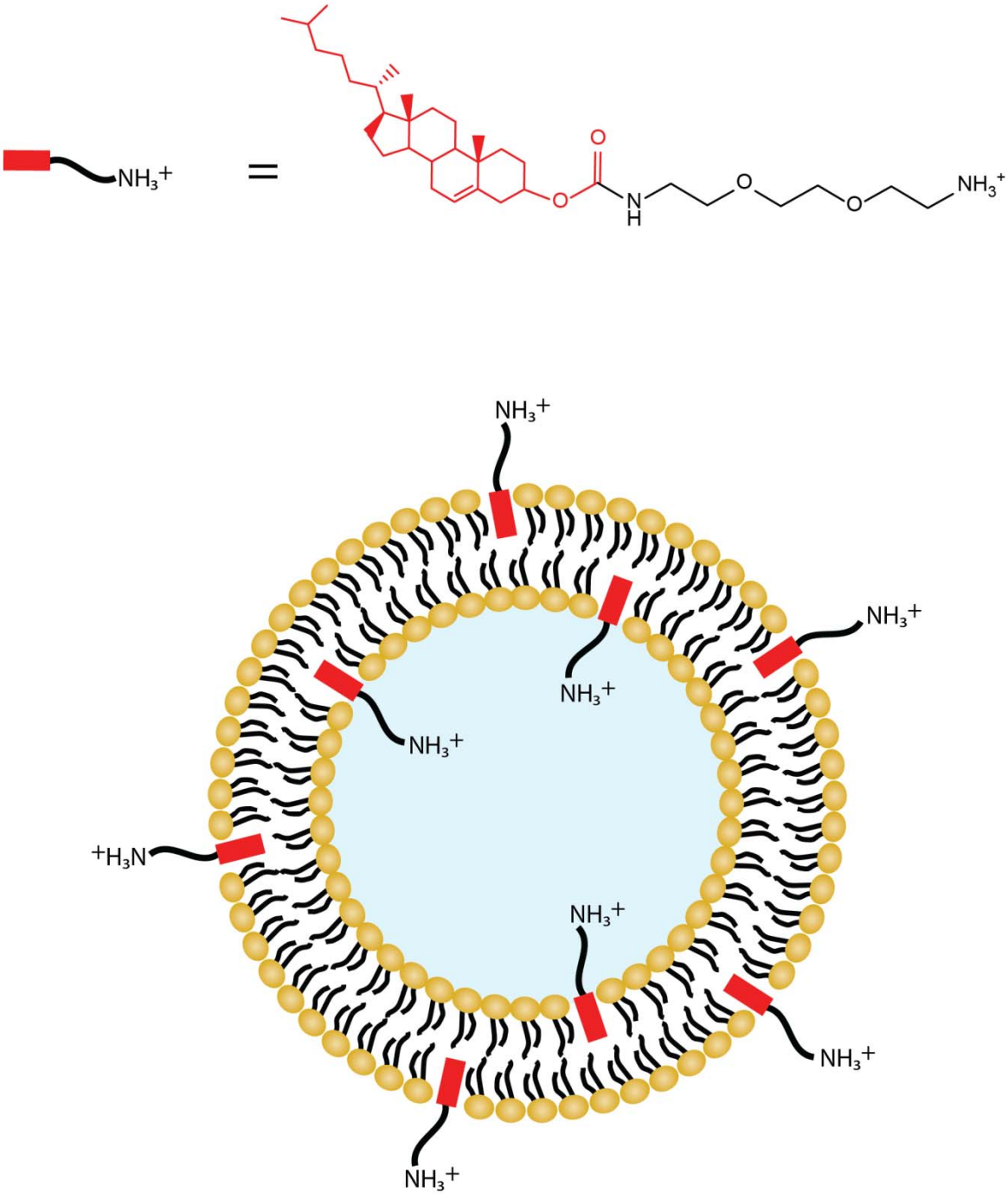

Figure 4-1: 3-O (2-aminoethoxyethyloxyethyl)carbamyl cholesterol (AECHO) and AECHO incorporated into a Large Unilamellar Vesicle (AECHO-LUV) at physiological pH.

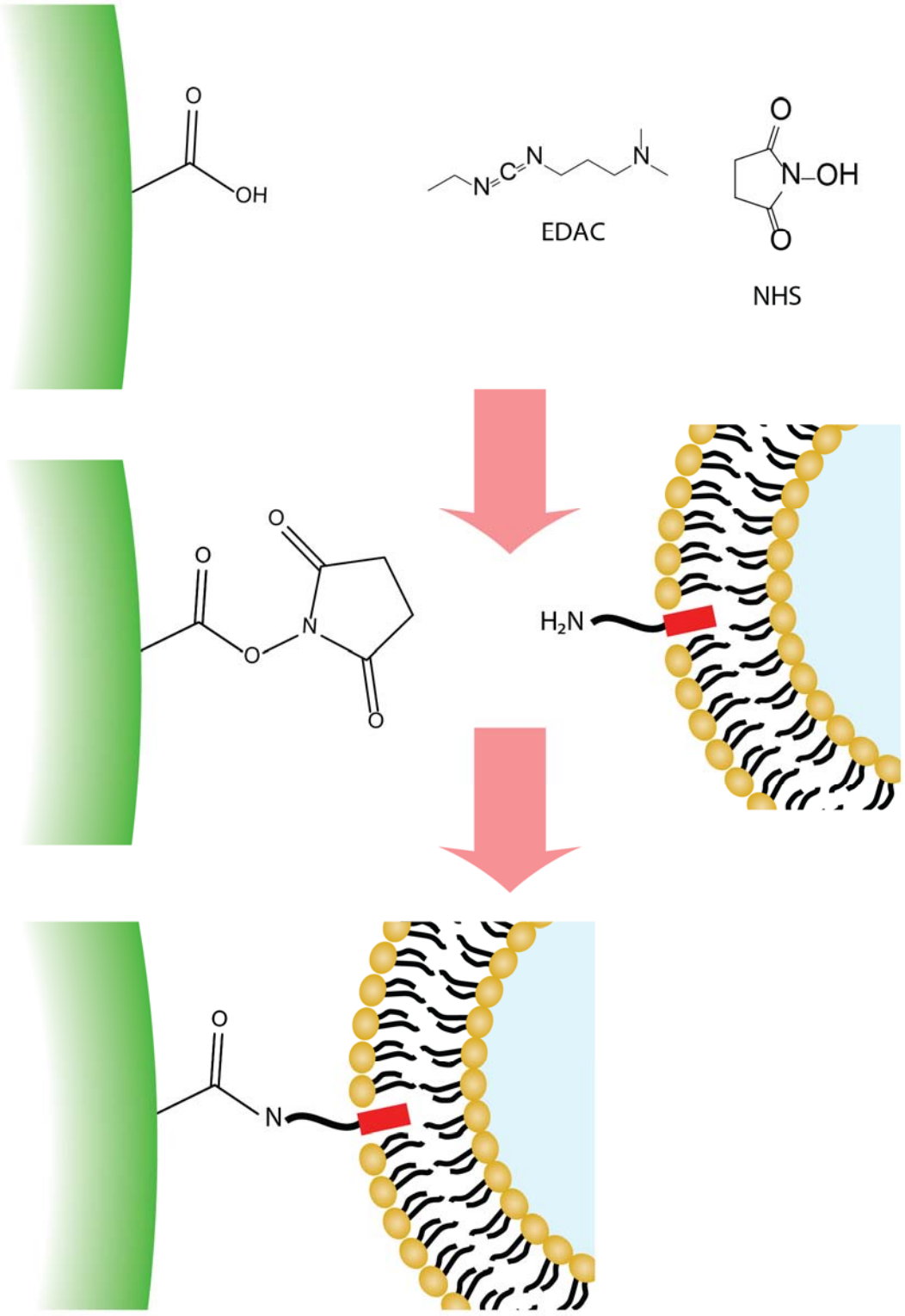

Figure 4-2: VESCOgel fabrication from NHS-activated microgels and AECHO-LUVs.

Note that, due to electrostatic attraction, simply mixing carboxylated microgels with surface amine-decorated liposomes produces extensive binding between the two. AECHO-LUVs will be cationically surface-charged at physiological pH, given that the pKa of EDR-148 amines is 9.4,[15] and would not be expected to change substantially upon modification to AECHO or its subsequent incorporation into LUVs. Zeta potential measurements on such AECHO-LUVs yielded a value of +9.15 ± 2.52 mV. Non-NHS-activated microgels, having surface-localized carboxyls, were negatively charged at physiological pH with a zeta potential of -24.2 ± 0.9 mV. Even upon NHS-activation some surface-localized negative charge is to be expected, since NHS-activation is generally less than complete, while NHS hydrolysis will occur progressively. The issue with purely electrostatic binding is that complexes so formed can be difficult to maintain under physiological salt conditions.

To screen for conditions under which robust binding could be maintained even at higher salt concentrations, qualitative microgel binding assays were undertaken using LUVs containing various amounts of AECHO (1, 5 or 20 mol %) plus 0.05 mol % RhB-PE as a fluorophore. These were mixed first with non-NHS-activated microgels under low-salt conditions (10 mM PB, pH 7.4) and then washed under high-salt conditions (100 mM KCl, 10 mM PB, pH 7.4). Qualitatively, 1 mol % AECHO failed to yield any LUV binding even in a low salt buffer, much less after a high salt wash. AECHO at the 5 mol % level yielded LUV binding in low salt, but this binding was eliminated by the high salt wash. Only at 20 mol % AECHO was there a substantial high salt-resistant LUV binding. When NHS-activated microgels were substituted next, 1 mol % AECHO likewise produced little or no binding before or after washing with a high salt buffer. However, 5 mol % AECHO yielded substantial LUV binding even subsequent to washing with high salt, as did 20 mol % AECHO. Incorporation of cholesterol at high concentrations can lead

to an inhomogeneous distribution in the bilayer[16,17] and can also affect the bilayer phase transition[18], thickness[19] and rigidity[20]. Hence, on the principle that it was desirable to employ the least amount of AECHO necessary to yield salt-resistant binding, further investigations were conducted using LUVs containing 5 mol % AECHO.

Figure 4-3 shows a quantitative liposome-microgel binding assay wherein a fixed quantity of NHS-activated microgel was titrated with progressively increasing quantities of LUVs containing 5 mol % AECHO, plus 0.05 mol % RhB-PE. The LUVs and microgels were allowed to interact overnight in a low salt buffer (10 mM PB, pH 7.4), then washed with a high salt buffer (100 mM KCl, 10 mM PB, pH 7.4). It is presumed that this salt-resistant lipid binding represents LUVs bound to microgels due to nucleophilic attack of AECHO amines on NHS-activated carboxyls with formation of an amide bond covalently linking the lipid bilayer intercalated cholesterol group with the microgel matrix through the two ethylene oxide spacer units. One observes that there are apparently two binding regimes: at lower lipid / microgel weight ratios the proportion of lipid bound / lipid added is roughly 1 / 2, while above approximately a 1 / 1 lipid / microgel weight ratio lipid binding increases further but with decreased avidity.

To put these binding results in perspective, if each microgel bead was encapsulated by a unilamellar lipid bilayer, then lipid binding should saturate at approximately 0.25 mg lipid/mg microgel. This calculation assumes a perfectly smooth microgel bead of radius 650 nm and a polymer density of approximately 72 mg/ml, based on the size and molecular mass data reported by Sorrell and Lyon[21] for analogous core-shell pNIPAM/p(NIPAM-*co*-AA) microgels. The surface area per POPC is assumed to be 70 $Å^2$. Hence, the binding data in Figure 4-3 are inconsistent with the presence of a single lipid bilayer encapsulated microgel, with the proviso in mind that microgels are certainly not perfectly smooth and that any roughness would

increase the effective surface area to be encapsulated. Alternately, if each microgel bead was completely coated by closely-packed LUVs of mean diameter of 103 nm, then lipid binding should saturate at approximately 0.9 mg lipid/mg microgel. For this scenario, the binding data in Figure 4-3 indicate that the microgels are only approximately 50% saturated. Overall, such binding data do not provide, therefore, a definitive answer to the single bilayer versus LUV coating question.

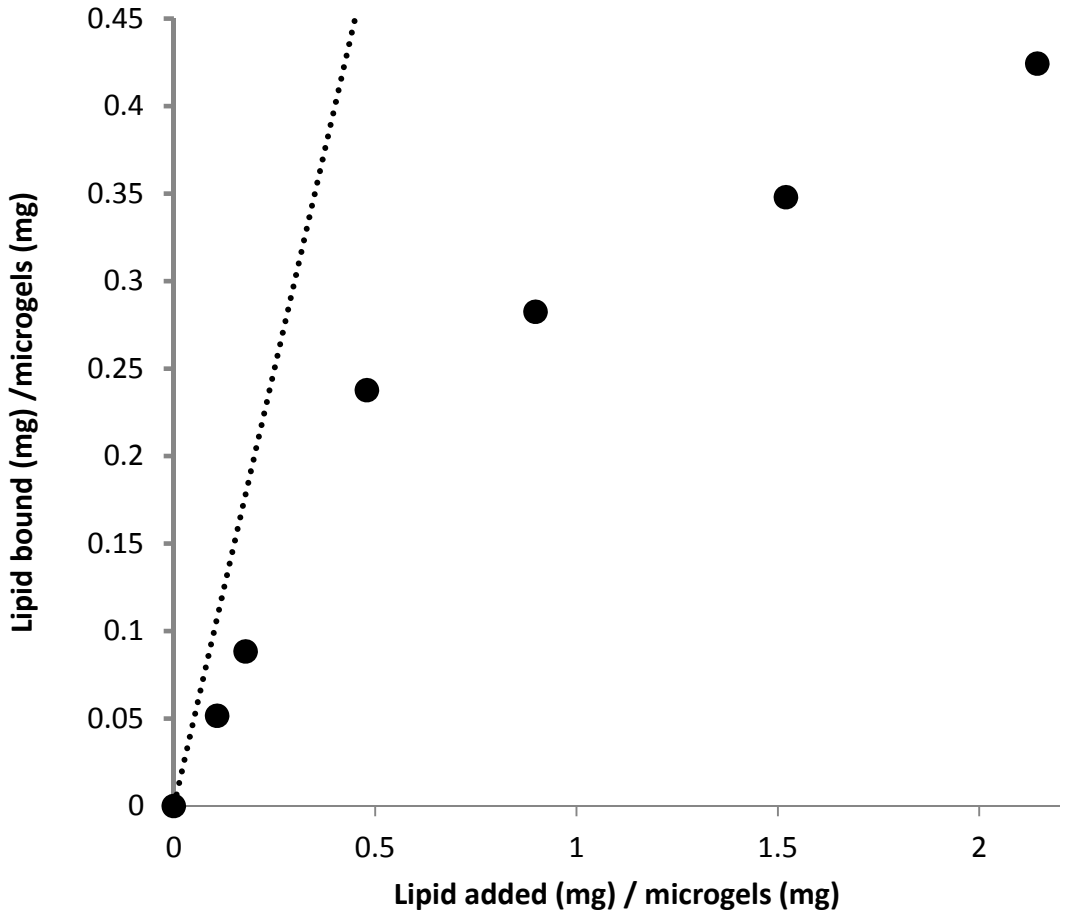

Figure 4-3: Fluorescence-based LUV-microgel binding assay, conducted via titration of NHS-activated core-shell pNIPAM / p(NIPAM-*co*-AA) microgels with increasing amounts of 5% AECHO-LUV containing 0.05 mol % RhB-PE, all in PB (10 mM phosphate, pH 7.4). Data points correspond to mg of lipid bound / mg microgel after washing with PBS (100 mM KCl, 10 mM phosphate, pH 7.4), demonstrating salt-stable binding. The dotted line represents quantitative binding.

4.3.2 Fluorescence recovery after photobleaching

The question of whether or not binding of AECHO-LUVs to microgels results in their fusion into a continuous lipid bilayer encapsulating the microgel bead can be addressed via FRAP experiments. As evident in Figure 4-4A, the confocal fluorescence microscopy image of a typical VESCOgel assembled with 5 mol % AECHO-LUVs, containing 0.05 mol % RhB-PE for fluorescence imaging purposes, exhibits fluorescence intensity localized to, and homogenously distributed within, the shell region of a micrometer sized particle. The diffraction-limited spatial resolution does not permit differentiation between discrete LUVs completely coating the surface versus a continuous bilayer arrangement.

Figure 4-4B shows the result of applying a tightly focused high power laser beam on a portion of the same VESCOgel particle. The region consequently bleached of fluorescence is about three to four times larger than the diameter of an individual AECHO-LUV. If fusion of individual LUVs into a continuous lipid bilayer had occurred, then diffusion of RhB-PE from non-bleached regions back into the bleached region would result in recovery of the fluorescence in that region. As evident in Figure 4-4C, even 10 minutes after photobleaching no significant recovery of fluorescence has taken place. Since 10 minutes represent many multiples of the time normally required for such recovery in a fluid lipid bilayer, it can be concluded that fusion of AECO-LUVs bound to the microgel surface has not taken place. Even when VESCOgels were subjected to several freeze-thaw cycles in the presence of excess lipid, a process known to be helpful in inducing fusion of surface-bound LUVs in other instances,[11,22] FRAP experiments yielded no recovery of fluorescence.

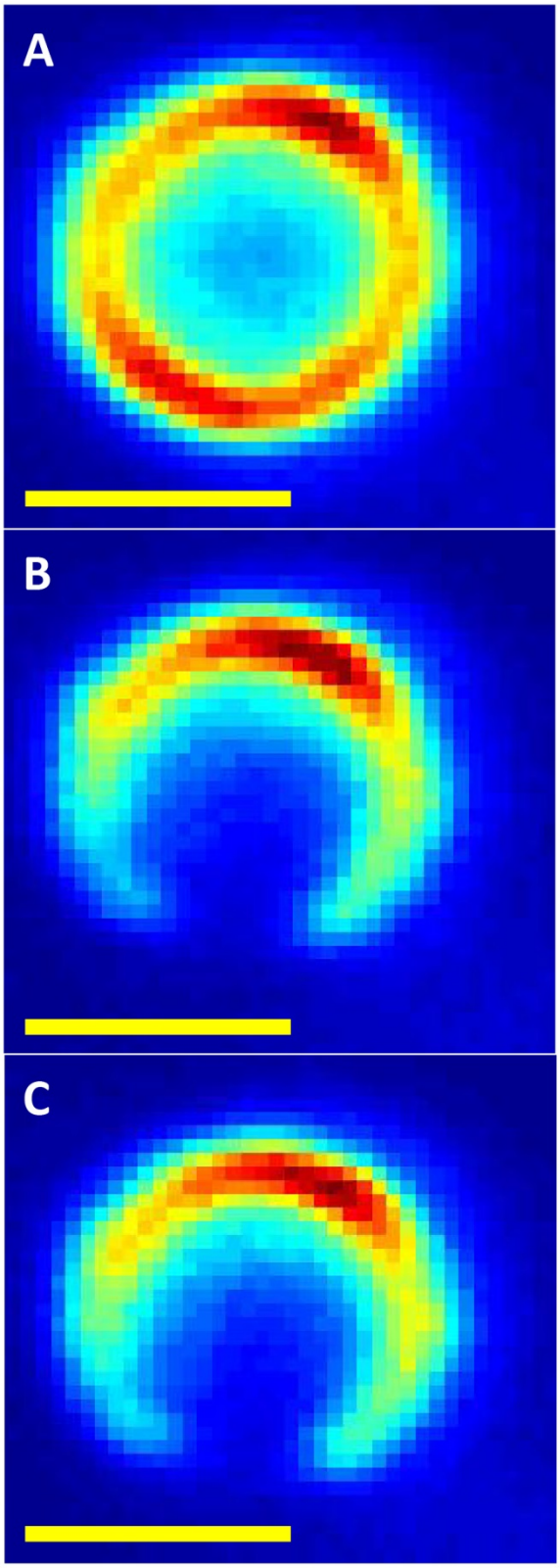

Figure 4-4: FRAP images acquired from a VESCOgel fabricated with AECHO-LUVs containing 0.05% RhB-PE. (A) Before photobleaching. (B) Immediately after photobleaching. (C) 10 minutes after photobleaching. The yellow bar represents 1 µm.

Liposome deposition at high density, followed by fusion, either spontaneous or induced, is one of the most common methods used to coat a surface with a continuous lipid bilayer.[23,24] The LUV binding data in Figure 4-3 indicate that the microgel surface is far from saturated with LUVs, suggesting that the reason fusion has not occurred here is that the critical density required for fusion was not achieved. Vesicle fusion requires close apposition of adjacent bilayer surface, hence the density requirement. Another factor inhibiting fusion is lipid bilayer surface charge, here due to the presence of unreacted AECHO, which introduces an additional energy barrier to two vesicles approaching each other. In fact, LUV surface charge may explain the difficulty in binding AECHO-LUVs to high density, and the biphasic lipid binding behaviour seen in Figure 4-3, since, once a certain number of AECHO-LUVs have bound, the resulting positively-charged microgel will repel positively-charged LUVs and inhibit further binding.

4.3.3 Lamellarity of Microgel-Bound AECHO-LUVs

Previous work on LUVs bound to microgels via hydrophobic anchoring to tetradecyl chains covalently attached to the polymer matrix demonstrated that the permeability barrier properties of the lipid bilayers were greatly compromised as a consequence of their interaction with the microgel.[25] To explore this question for case of AECHO-LUVs in VESCOgels, a lamellarity assay was conducted in which sodium dithionite quenching of NBD-PE incorporated into the lipid bilayers was examined, as shown in Figure 4-5. For an impermeable, large unilamellar lipid bilayer vesicle, 50% of the NBD-PE fluorescence will be quenched upon addition of sodium dithionite to the external solution, since this quencher should not permeate an intact lipid bilayer. Indeed, this is seen to be the case for AECHO-LUVs free in solution. When the barrier properties are compromised, as they are upon addition of the detergent

Triton which solubilises the lipids, 100% of the NBD-PE fluorescence is quenched by sodium dithionite. Essentially identical results are obtained for AECHO-LUVs bound to the microgel, indicating that they remain unilamellar and that their permeability barrier properties remain intact. As will be related below, this is useful for controlled release applications.

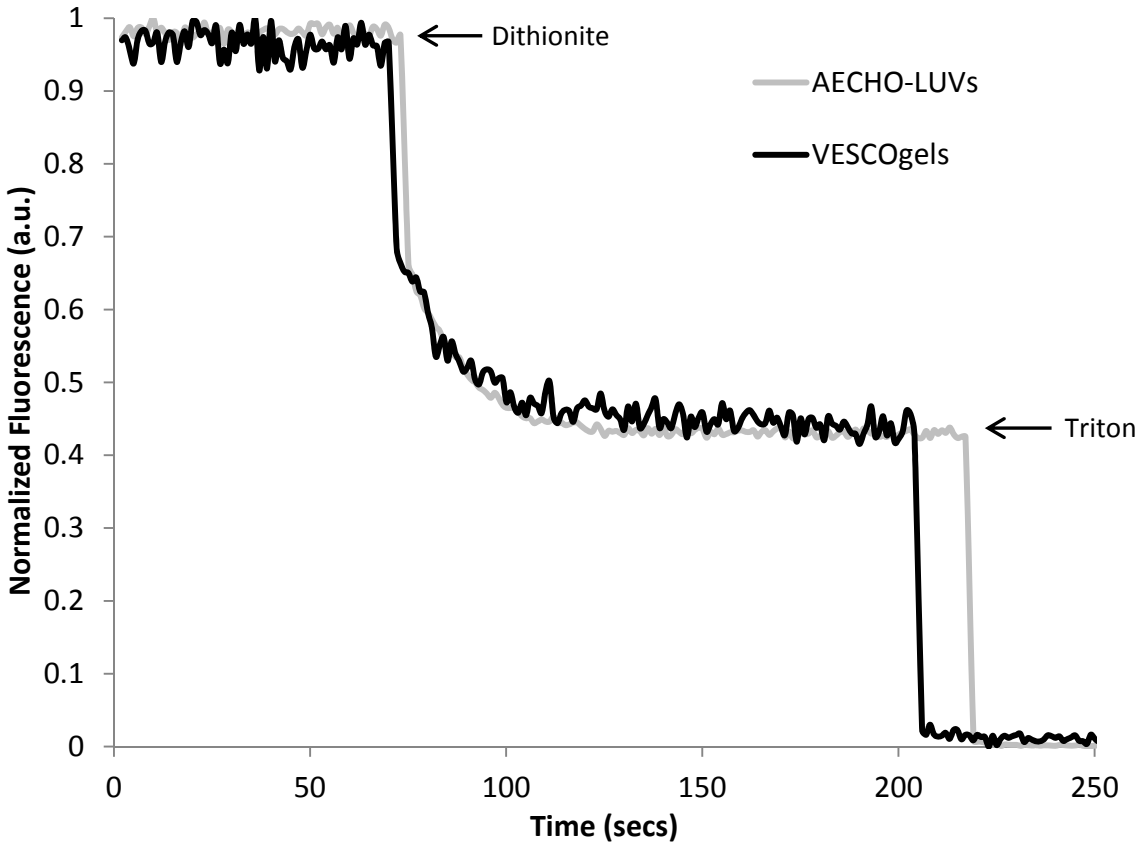

Figure 4-5: Sodium dithionite lamellarity assay performed on free AECHO-LUVs (grey) and VESCOgels (black). Only 50% of the lipids in both were accessible to the dithionite quencher, showing properly impermeable bilayers. This indicates that AECHO-LUV binding to microgels does not make them leaky. Triton was added to disassemble the bilayer.

4.3.4 Dual Carrier and Release Characteristics of VESCOgels

An attractive feature of VESCOgels is that they consist of two distinct compartments – the lipid bilayer vesicle interior and the microgel interior – each capable of carrying separate

molecular cargos. To demonstrate such compartmentalization of molecular cargos in VESCOgels, two distinguishable fluorophores were encapsulated simultaneously: RhB within the AECHO-LUVs and FS within the microgel matrix. Figure 4-6 shows fluorescence images of such VESCOgels, wherein RhB and FS were excited alternatively and, with use of appropriate bandpass filters, separate RhB and FS fluorescence images acquired independently without signal interference. Figure 4-6A shows the RhB image and Figure 4-6B shows the FS image, demonstrating their co-localization with the VESCOgels. Figure 4-6C shows the fluorescence intensity profile along one VESCOgel, demonstrating that the RhB signal is concentrated at the periphery where the AECHO-LUVs would be situated, while the FS signal is diffusely distributed across the entirety of the microgel.

Having established that distinct cargos can be entrapped within the separate AECHO-LUV and microgel interior compartments of VESCOgels, their release profiles were characterized independently. For the microgel interior compartment, FS was again entrapped and its release into the aqueous external environment was monitored. For monitoring release from the AECHO-LUV interior, cobalt-calcein was entrapped, the vesicles were bound to the microgel and leakage was assessed by addition of the cobalt chelator EGTA. This method is routinely used to measure membrane integrity[11,26–29] and does not require separation of the leaked contents from the LUVs for assessment. In our experiments, the chelator is added to the exterior of the cobalt-calcein entrapping liposomes and any fluorescence enhancement from liberated calcein is measured. Then, Triton is added to permeate the bilayer to measure the total fluorescence possible when EGTA chelates with all cobalt-calcein available, leaving behind only fluorescent calcein.

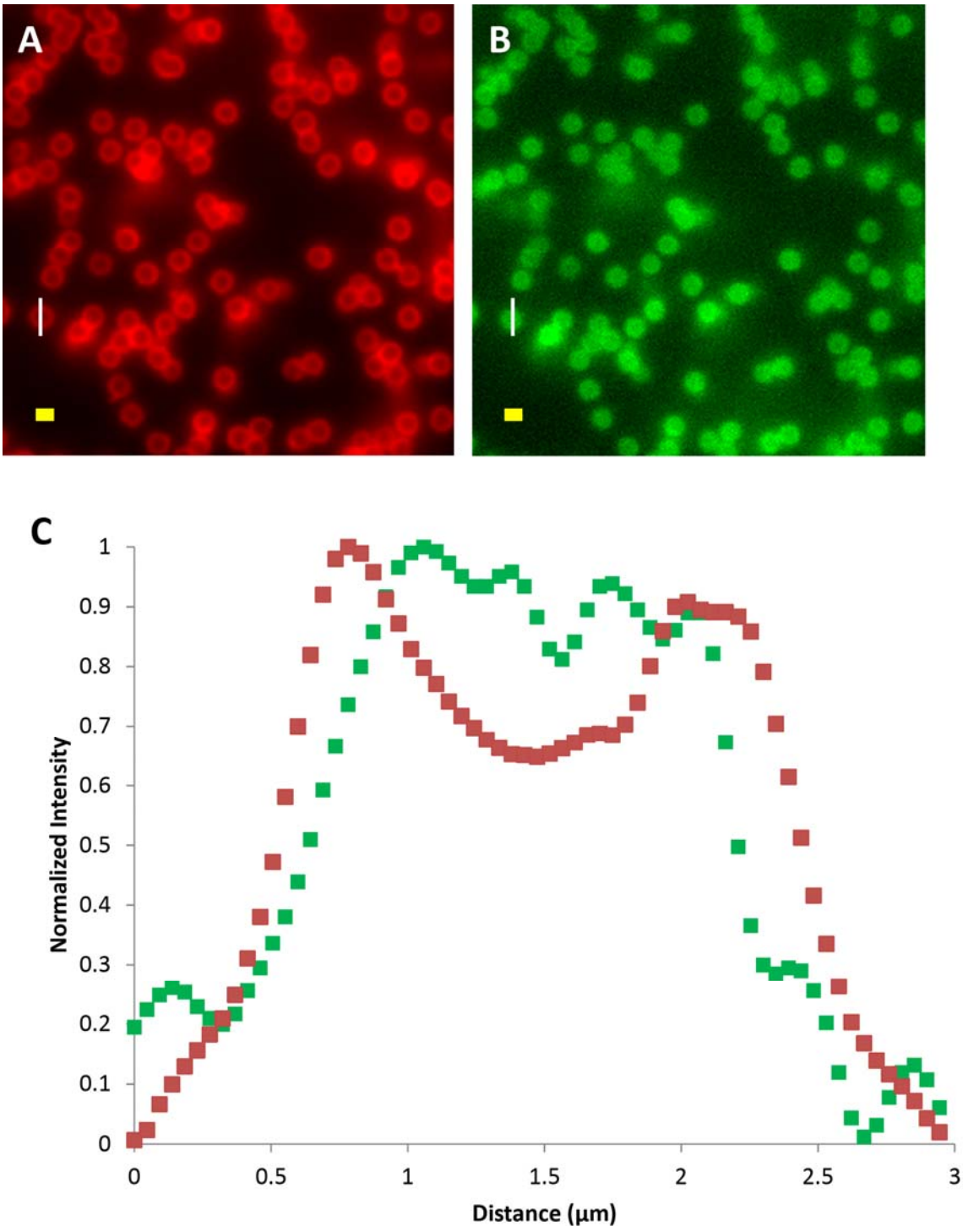

Figure 4-6: Fluorescence microscopy images demonstrating the dual carrier capacity of VESCOgels. RhB was encapsulated within AECHO-LUVs and FS was trapped within NHS-activated microgels prior to complexation between the two to form VESCOgels. (A) RhB emission. (B) FS emission. (C) Fluorescence profiles traversing a single VESCOgel (as indicated by the white line in A and B) for images of RhB (■) and sodium fluorescein (■).The yellow bar represents 1 µm.

As shown in Figure 4-7, the cobalt-calcein cargo borne by the AECHO-LUVs bound to the microgels remained essentially completely entrapped within the AECHO-LUV interior over the course of a number of days, regardless of whether stored at room temperature or at 37 ^{o}C. Co-calcein release from AECHO-LUVs prior to microgel binding and from simple POPC LUVs was also measured and did not yield a significantly different release profile relative to AECHO-LUV bound to microgels, regardless of temperature. Hence, the slow release observed cannot be attributed to preferential binding of co-calcein to AECHO or to some interaction with the microgel support.

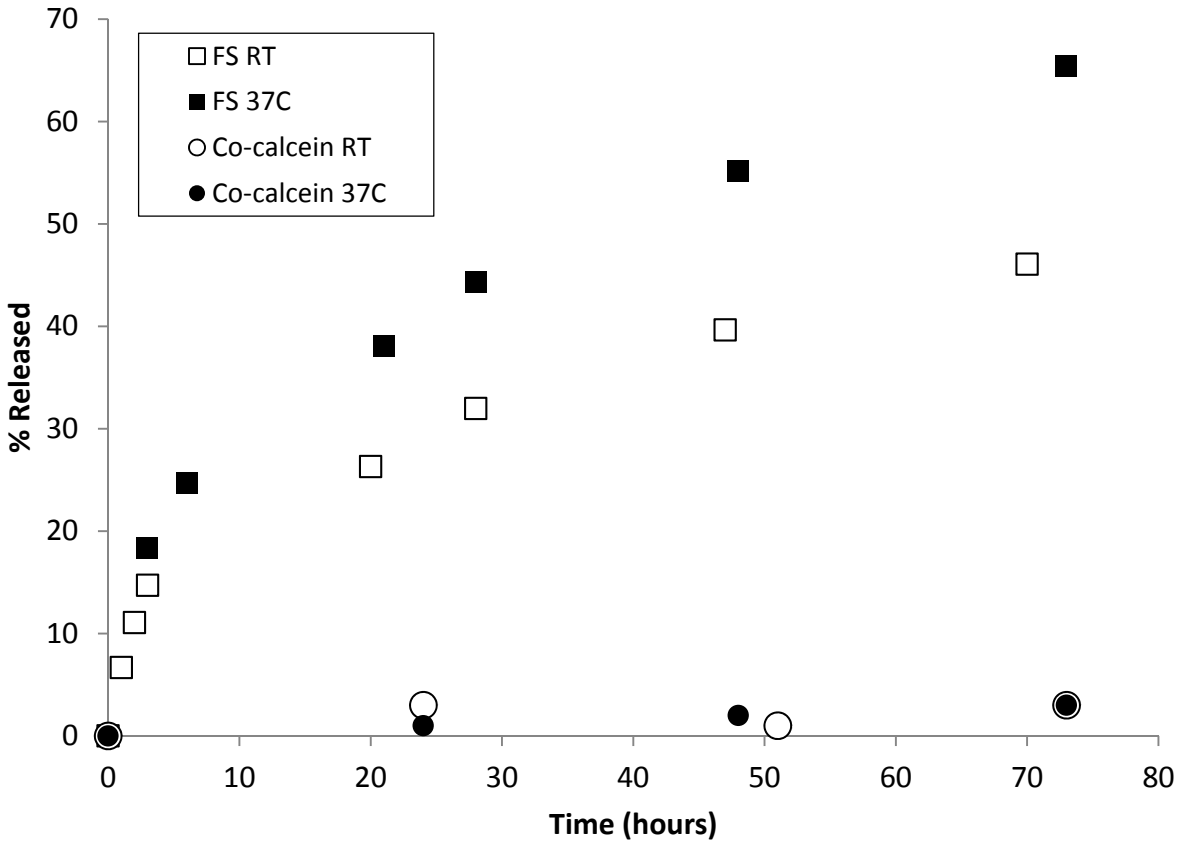

Figure 4-7: Release kinetics from VESCOgels assembled with either microgel-encapsulated FS (squares) or AECHO-LUV-encapsulated cobalt-calcein (circles). Data were acquired at either room temperature (open symbols) or at 37°C (closed symbols).

Note that this slow release behaviour is in contrast to earlier findings that liposomes bound to microgels which had been hydrophobically-modified with tetradecyl alkyl chains tended to exhibit greater instability above the VPT temperature.[25] That system and the current system differ in two significant features. First, tetradecyl chains tend to destabilize, while cholesterol tends to stabilize, lipid bilayers. Second, the current system incorporates hydrophilic ethylene oxide spacer groups between the LUV and microgel surfaces, which will tend to decouple their interactions.

In contrast to the slow release of AECHO-LUV-entrapped cargo, the FS cargo borne within the microgel polymer matrix achieved 50% release in a matter of 24 – 48 hours. Raising the temperature to 37 ^{o}C increased the rate of FS release, but failed to produce a "pulse" of released FS such as might be expected to occur once the temperature exceeded the microgel's volume phase transition at approximately 32 ^{o}C. These results demonstrate that, not only can separate cargoes be entrapped within the distinct VESCOgel compartments, they exhibit distinct rapid versus slow release kinetics.

The release kinetics of both the AECHO-LUVs and the microgel itself were in all essentials virtually identical to those obtained with separate AECHO-LUVs prior to their binding to microgels, and with the microgels themselves prior to their being coated with AECHO-LUVs. While perhaps unsurprising for the AECHO-LUVs, this was not the behaviour anticipated for the microgels. Several explanations are possible. First, the coverage of the microgel surface with bound AECHO-LUVs may not have been sufficiently dense as to significantly curtail FS diffusion out of the microgel interior. While the binding data in Figure 4-3 indicate that AECHO-LUV binding was only roughly half of that expected for a closely-packed surface, the fact that coated and uncoated microgels exhibited virtually identical FS release kinetics suggests that another

explanation should be sought. The observation that raising the temperature above the microgel's VPT produced no pulse of FS release points to a couple of different scenarios.

Firstly, the microgel VPT might not be robust enough to result in a burst release. We have already shown that the VPT temperature of our microgels is 32°C.[11] Additionally, our lab has also previously shown in that when a highly crosslinked charged shell is incorporated on core microgels, similar to the microgels used in this study, the shell does not have much influence on the VPT temperature of the microgel.[25] Jones and Lyon[30] have also observed that low crosslinked charged shells do not alter the VPT temperature by a large degree. However, they point out that in core-shell microgels, the magnitude of collapse is much smaller with a charged shell than with a non-charged shell. That is, the charged shell restricts the extent of microgel collapse. In Mackinnon et al[25], the VPT behaviour of core-shell microgel was studied using ^{1}H NMR, and it was shown that a residual NIPAM methyl signal was still present at very high temperatures when the shell is charged (indicating partial collapse) as opposed to no residual signal when the shell was neutral (indicating full collapse). This again demonstrated that the extent of microgel collapse was attenuated when a charged shell was present on the microgel. This could explain why the expected burst release does not occur in VESCOgels. That is, even though the microgels are already collapsed at 37°C, the magnitude of the collapse might not have been enough to result in a burst release.

The second reason why a pulse release might not be seen is that FS might not be a passive occupant of the aqueous interior of the microgel matrix, and might actively interact with the pNIPAM matrix. Electrostatics may be one such form of interaction. Specifically, during the FS loading phase it was observed that NHS-activated microgels were able to incorporate FS at a level two orders-of-magnitude greater than found for non-NHS-activated

microgels. Since the latter, like FS, are negatively-charged at physiological pH, electrostatic repulsion is the obvious explanation for the loading difference. Once FS is entrapped, over time NHS ester (which have a half-life of 4-5 hours at 0°C[12]) hydrolysis would create an electrostatic barrier in the shell region through which FS would have to pass in order to escape the microgel interior. Since FS release kinetics for AECHO-LUV-coated and non-coated microgels were virtually identical, FS interactions with the LUVs do not appear to be a factor. Alternately, FS can hydrogen bond extensively,[31] a property favouring interactions with the amide moieties of NIPAM. Indeed, some VESCOgels in Figure 4-6B do show a somewhat higher concentration of FS in the highly dense pNIPAM shell region, but signal to noise limitations prevent a more quantitative analysis. Such interactions would tend to retard its diffusion out of the microgel matrix, even at temperatures above the VPT. Whether electrostatics or hydrogen bonding, or some combination thereof, play a role, it is evident in Figure 4-7 that FS release from the microgel appears to be biphasic, with a fast efflux of roughly 15% of contents at room temperature, and 30% at 37 ^{o}C, followed by a slower release phase. Such behaviour suggests some combination of weaker and stronger interactions between FS and the microgel polymer matrix.

4.3.5 Conclusions

We have fabricated VESCOgels consisting of lipid bilayer vesicles coating the surface of core-shell pNIPAM/p(NIPAM-*co*-AA) microgels. Coating was achieved through carbodiimide chemistry between NHS-activated AA carboxyls located at the microgel periphery and AECHO-containing LUVs having surface displayed amines. The microgel-bound AECHO-LUVs remained impermeable upon coupling and did not fuse with one another. VESCOgels provided two

distinct aqueous compartments for entrapping molecular cargo: the LUV interior and the microgel matrix. Each displayed separate and characteristic cargo release kinetics, indicating the possibility of combining fast and slow release kinetics in a single carrier assembly. This is not limited to water-soluble cargos, but could include hydrophobic species, since pNIPAM microgels above the VPT temperature are known to absorb hydrophobic drugs.[32] Liposomes, of course, have long been used for such purposes and their compositions can be manipulated to tailor cargo release kinetics,[33,34] with the choice of drug being an important factor.

4.4 References

(1) Inzucchi, S. E. Oral Antihyperglycemic Therapy for Type 2 Diabetes: Scientific Review. *JAMA, J. Am. Med. Assoc.* **2002**, *287*, 360–372.

(2) Kerbel, R. S. Tumor Angiogenesis: Past, Present and the Near Future. *Carcinogenesis* **2000**, *21*, 505–515.

(3) Lee, D. M.; Weinblatt, M. E. Rheumatoid Arthritis. *Lancet* **2001**, *358*, 903–911.

(4) Song, X.; Zhao, Y.; Hou, S.; Xu, F.; Zhao, R.; He, J.; Cai, Z.; Li, Y.; Chen, Q. Dual Agents Loaded PLGA Nanoparticles: Systematic Study of Particle Size and Drug Entrapment Efficiency. *Eur. J. Pharm. Biopharm.* **2008**, *69*, 445–453.

(5) Castro, E.; Mosquera, V.; Katime, I. Dual Drug Release of Triamterene and Aminophylline from Poly (N-Isopropylacrylamide) Hydrogels. *Nanomater. Nanotechnol.* **2012**, *2*, 1–9.

(6) Xia, W.; Chang, J.; Lin, J.; Zhu, J. The pH-controlled Dual-drug Release from Mesoporous Bioactive Glass/polypeptide Graft Copolymer Nanomicelle Composites. *Eur. J. Pharm. Biopharm.* **2008**, *69*, 546–552.

(7) Wei, L.; Cai, C.; Lin, J.; Chen, T. Dual-drug Delivery System Based on Hydrogel/micelle Composites. *Biomaterials* **2009**, *30*, 2606–2613.

(8) Manna, U.; Patil, S. Dual Drug Delivery Microcapsules via Layer-by-Layer Self-Assembly. *Langmuir* **2009**, *25*, 10515–10522.

(9) Zhong, D.; Liu, Z.; Xie, S.; Zhang, W.; Zhang, Y.; Xue, W. Study on poly(D,L-lactic) Microspheres Embedded in Calcium Alginate Hydrogel Beads as Dual Drug Delivery Systems. *J. Appl. Polym. Sci.* **2013**, *129*, 767–772.

(10) Liu, B.; Mazouchi, A.; Gradinaru, C. C. Trapping Single Molecules in Liposomes: Surface Interactions and Freeze−thaw Effects. *J. Phys. Chem. B* **2010**, *114*, 15191–15198.

(11) Saleem, Q.; Liu, B.; Gradinaru, C. C.; Macdonald, P. M. Lipogels: Single-lipid-bilayer-enclosed Hydrogel Spheres. *Biomacromolecules* **2011**, *12*, 2364–2374.

(12) Hermanson, G. T. Chapter 2 - The Chemistry of Reactive Groups. In *Bioconjugate Techniques (Second Edition)*; Academic Press: New York, 2008; pp. 169–212.

(13) Savariar, E. N.; Thayumanavan, S. Controlled Polymerization of N-isopropylacrylamide with an Activated Methacrylic Ester. *J. Polym. Sci., Part A: Polym. Chem.* **2004**, *42*, 6340–6345.

(14) Kaihara, S.; Narikawa, M.; Fujimoto, K. Preparation of Thermosensitive Polymer Nanoparticles by Protein-mimetic Cross-linking. *Colloid Polym. Sci.* **2012**, *290*, 1317–1325.

(15) Simons, D. M. Quinidine Conjugates and Their Use in Immunoassays. US Patent 6,140,530, October 2000.

(16) De Kruijff, B.; Cullis, P. R.; Radda, G. K. Outside-inside Distributions and Sizes of Mixed Phosphatidylcholine-cholesterol Vesicles. *Biochim. Biophys. Acta, Biomembr.* **1976**, *436*, 729–740.

(17) Kučerka, N.; Nieh, M.-P.; Katsaras, J. Asymmetric Distribution of Cholesterol in Unilamellar Vesicles of Monounsaturated Phospholipids. *Langmuir* **2009**, *25*, 13522–13527.

(18) Genz, A.; Holzwarth, J. F.; Tsong, T. Y. The Influence of Cholesterol on the Main Phase Transition of Unilamellar Dipalmytoylphosphatidylcholine Vesicles. A Differential Scanning Calorimetry and Iodine Laser T-jump Study. *Biophys. J.* **1986**, *50*, 1043–1051.

(19) Gallová, J.; Uhríková, D.; Kučerka, N.; Teixeira, J.; Balgavý, P. Hydrophobic Thickness, Lipid Surface Area and Polar Region Hydration in Monounsaturated Diacylphosphatidylcholine Bilayers: SANS Study of Effects of Cholesterol and B-sitosterol in Unilamellar Vesicles. *Biochim. Biophys. Acta, Biomembr.* **2008**, *1778*, 2627–2632.

(20) Liu, D.-Z.; Chen, W.-Y.; Tasi, L.-M.; Yang, S.-P. Microcalorimetric and Shear Studies on the Effects of Cholesterol on the Physical Stability of Lipid Vesicles. *Colloids Surf., A* **2000**, *172*, 57–67.

(21) Sorrell, C. D.; Lyon, L. A. Deformation Controlled Assembly of Binary Microgel Thin Films. *Langmuir* **2008**, *24*, 7216–7222.

(22) Sugihara, K.; Jang, B.; Schneider, M.; Vörös, J.; Zambelli, T. A Universal Method for Planar Lipid Bilayer Formation by Freeze and Thaw. *Soft Matter* **2012**, *8*, 5525–5531.

(23) Tanaka, M.; Sackmann, E. Polymer-supported Membranes as Models of the Cell Surface. *Nature* **2005**, *437*, 656–663.

(24) Troutier, A.; Ladavière, C. An Overview of Lipid Membrane Supported by Colloidal Particles. *Adv. Colloid Interface Sci.* **2007**, *133*, 1–21.

(25) MacKinnon, N.; Guérin, G.; Liu, B.; Gradinaru, C. C.; Rubinstein, J. L.; Macdonald, P. M. Triggered Instability of Liposomes Bound to Hydrophobically Modified Core−shell pNIPAM Hydrogel Beads. *Langmuir* **2010**, *26*, 1081–1089.

(26) Oku, N.; Kendall, D. A.; MacDonald, R. C. A Simple Procedure for the Determination of the Trapped Volume of Liposomes. *Biochim. Biophys. Acta, Biomembr.* **1982**, *691*, 332–340.

(27) Kendall, D. A.; MacDonald, R. C. A Fluorescence Assay to Monitor Vesicle Fusion and Lysis. *J. Biol. Chem.* **1982**, *257*, 13892–13895.

(28) Lins, L.; El Kirat, K.; Charloteaux, B.; Flore, C.; Stroobant, V.; Thomas, A.; Dufrene, Y.; Brasseur, R. Lipid-destabilizing Properties of the Hydrophobic Helices H8 and H9 from Colicin E1. *Mol. Membr. Biol.* **2007**, *24*, 419–430.

(29) Shimanouchi, T.; Walde, P.; Gardiner, J.; Mahajan, Y. R.; Seebach, D.; Thomae, A.; Krämer, S. D.; Voser, M.; Kuboi, R. Permeation of a B-heptapeptide Derivative Across Phospholipid Bilayers. *Biochim. Biophys. Acta, Biomembr.* **2007**, *1768*, 2726–2736.

(30) Jones, C. D.; Lyon, L. A. Synthesis and Characterization of Multiresponsive Core−Shell Microgels. *Macromolecules* **2000**, *33*, 8301–8306.

(31) Klonis, N.; Clayton, A. H. A.; Voss, E. W.; Sawyer, W. H. Spectral Properties of Fluorescein in Solvent-Water Mixtures: Applications as a Probe of Hydrogen Bonding Environments in Biological Systems. *Photochem. Photobiol.* **1998**, *67*, 500–510.

(32) Hoare, T.; Pelton, R. Impact of Microgel Morphology on Functionalized Microgel−Drug Interactions. *Langmuir* **2008**, *24*, 1005–1012.

(33) Bally, M. B.; Lim, H.; Cullis, P. R.; Mayer, L. D. Controlling the Drug Delivery Attributes of Lipid-based Drug Formulations. *J. Liposome Res.* **1998**, *8*, 299–335.

(34) Lim, H. J.; Masin, D.; Madden, T. D.; Bally, M. B. Influence of Drug Release Characteristics on the Therapeutic Activity of Liposomal Mitoxantrone. *J. Pharmacol. Exp. Ther.* **1997**, *281*, 566–573.

Lateral Diffusion of Bilayer Lipids Measured via ^{31}P CODEX NMR

5.1 Introduction

Much of the increasingly sophisticated picture of biomembrane organization and functional segregation has arisen thanks to the increasing sophistication of the experimental tools available for examining lateral diffusion.[1–6] Foremost among these are techniques based on fluorescence, such as FRAP (fluorescence recovery after photobleaching)[7–11] and FCS (fluorescence correlation spectroscopy)[12–15], which examine the behaviour of fluorophore-bearing membrane lipids and proteins. The fluorophore is generally synthetic, as opposed to intrinsic to the molecule of interest. FRAP characterizes an ensemble behaviour, while FCS typically involves fewer than 10 fluorophores. More recently, single particle tracking (SPT) techniques, in which the behaviour of an individual molecule is monitored, have revealed details of the time- and space-dependence of the diffusion behaviour otherwise obscured in an ensemble-average.[16–25] In SPT studies, the actual observable signal originates from some typically large, covalently attached moiety such as a quantum dot, or chimeric fluorescent protein.

NMR spectroscopy may be used to measure diffusion via the application of pulsed field gradients (PFG) to render the NMR signals diffusion dependent.[26,27] The PFG NMR diffusion technique has been applied in an impressive variety of circumstances, to great effect, as described in a number of now-classic reviews.[28–31] The inherent advantages of an NMR approach include the absence (generally) of any synthetic, potentially perturbing, probe, and the ability to simultaneously monitor diffusion of multiple molecular species.

In biological membranes, however, PFG NMR diffusion studies encounter the difficulty that molecular motions are generally slow and/or anisotropic, such that orientation-dependent interactions, like the dipolar, or quadrupolar, or anisotropic chemical shift, are, at best, only incompletely averaged. This produces broad NMR resonances which usually do not survive the PFG NMR diffusion pulse sequences. Consequently, NMR diffusion measurements have not enjoyed the same popularity in membranes as they have in solution.

Nevertheless, NMR techniques for lateral diffusion measurement are available. These may be divided, broadly, into those which seek to eliminate the orientation-dependent interactions in order to produce narrow NMR resonances appropriate for PFG NMR diffusion studies, and those which instead seek to exploit the orientation-dependence in order to extract diffusion information via exchange (EXSY) NMR measurements.

As discussed in Chapter 1, orientation-dependent interactions may be eliminated via MAS, thus producing narrow NMR resonances. When pulsed field gradients are applied in a direction co-linear with the spinning axis[32], then diffusion can be measured. Gawrisch and co-workers have used this approach to great effect in their ^{1}H NMR studies of lateral diffusion of a number of small molecules associating with lipid bilayer vesicles[33–37] and to examine domains and phase separations[38,39].

Another means by which to eliminate orientation-dependent NMR interactions is to macroscopically align the lipid bilayer ensemble on a solid support, like glass slides, and to orient the entire assembly at the magic angle of 54.74°. This produces ^{1}H NMR resonance line narrowing, since ^{1}H–^{1}H dipole–dipole interactions, the dominant source of line-broadening in ^{1}H NMR spectra of lipid bilayers, scale to zero under such circumstances. Lindblom and

coworkers have employed this approach with considerable success in their ^{1}H PFG NMR investigations of heterogeneities in lateral organization within lipid bilayers.[40–45]

A third, and related, approach involves the use of bicelles. These form fully hydrated, single-bilayer-thickness assemblies which spontaneously align inside a magnetic field such that the bilayer normal across the entire ensemble is uniformly oriented perpendicular to the magnetic field direction.[46–48] However, dipolar interactions are not scaled to zero, so ^{1}H PFG NMR lateral diffusion measurements in magnetically aligned bicelles rely on the presence of intrinsically mobile molecular segments with intrinsically narrow NMR resonances. For instance, lateral diffusion of PEGylated lipids is readily characterized due to the ease of observing the highly mobile PEG moiety.[49,50]

An entirely different, non-gradient, approach to NMR lateral diffusion measurements is to exploit orientation-dependent interactions, rather than eliminate them, in order to render NMR signals diffusion-dependent. When, for example, a phospholipid diffuses laterally around the radius of curvature of a spherical lipid bilayer vesicle, its orientation relative to the magnetic field changes, as does, in turn, its ^{31}P anisotropic chemical shift. In static, i.e. non-spinning, two-dimensional (2D) EXSY (exchange spectroscopy) ^{31}P NMR, off-diagonal intensity then appears at a frequency dictated by the initial versus final position of the phospholipid as a function of the mixing time during which diffusion was permitted to occur. This has been exploited to measure phospholipid lateral diffusion in lipid bilayers either formulated as multilamellar vesicles (broad distribution of vesicular radii) or supported on glass beads to provide a uniform vesicle radius.[51–53] Similarly, ^{2}H 2D EXSY NMR of deuterated lipids can yield lateral diffusion information via exploitation of the orientation dependence of the residual deuterium quadrupolar interaction.[54]

Such static 2D EXSY NMR measurements require long experiment times and exhibit limited spectral resolution. These issues may be overcome using one-dimensional (1D) versions of EXSY in combination with MAS. Under MAS conditions both signal-to-noise and resolution of isotropic chemical shift differences are enhanced, while 1D spectra require only a fraction of the signal acquisition time of 2D spectra. Examples include EIS (exchange induced sidebands)[55], ODESSA (1D exchange spectroscopy by sideband alternation)[56,57] and CODEX (centre-band only detection of exchange)[58]. EIS, ODESSA (and time-reversed ODESSA) use slow MAS, where the spinning frequency (ω_r) is slower than the residual anisotropic interaction ($\Delta\omega_{aniso}$), to produce an envelope of spinning sidebands (SSB) which are phase and amplitude manipulated with carefully timed radio-frequency (rf) pulses to yield exchange information. CODEX uses fast MAS ($\omega_r > \Delta\omega_{aniso}$), so that only the isotropic, i.e., centre-band, resonance remains, which produces further signal-to-noise improvements since the SSB are eliminated. When combined with rotor-synchronized rf pulses the CODEX resonances are rendered sensitive to exchange. CODEX, and its variants, have been used to measure correlation times of molecular and segmental dynamics, numbers of mobile sites, and reorientation angles in solids and semi-solids, largely focusing on small molecules and polymers.[58–63] However, CODEX has not been used as yet to investigate membrane lateral diffusion.

In this chapter, the use of ^{31}P CODEX NMR to determine lateral diffusion coefficients of phospholipids in unilamellar lipid bilayer vesicles is demonstrated. The LUVs were composed of POPC, alone or mixed with 30 mol % 1-palmitoyl-2-oleoyl-*sn*-glycero-3-phosphoglycerol (POPG) or cholesterol (CHOL). It is shown that, provided the size distribution of the vesicles and the viscosity of the lipid vesicle suspension are known, ^{31}P CODEX NMR yields reliable lateral diffusion coefficients simultaneously for multiple phospholipid species.

5.2 Materials and methods

5.2.1 Materials

POPC, POPG and DMPC were purchased from Avanti Polar Lipids (Alabaster, AL). All other reagents were purchased from Sigma–Aldrich (Oakville, ON, Canada).

5.2.2 Liposome preparation

LUVs were prepared by the extrusion method. The desired amounts of POPC, POPG and CHOL, total weight of lipid equal to 25.2 mg, were dissolved in a minimal volume of chloroform, the chloroform was evaporated using a stream of nitrogen, and the lipid film was left under vacuum overnight to remove remaining traces of solvent. To the lipid film, 1.0 mL of sucrose buffer (200 mM sucrose, 20 mM KCl, 10 mM HEPES, pH 7.4) was added and left unperturbed for one hour, following which it was subjected to 5 cycles of freeze–thaw–vortex, cycling between liquid nitrogen and a 60 °C water bath. The resulting suspension was extruded 25 times through a 0.4 μm polycarbonate membrane installed in a mini-extruder (Avanti Polar Lipids, Alabaster, AL). A fraction of the resulting LUV suspension was concentrated using a Centricon-30 micro-concentrator (Amicon, Oakville, ON) in a centrifuge at 3000 × g. Approximately 100 μL of this concentrated aqueous LUV suspension solution, containing on the order of 10 mg lipid, was transferred to a 5 mm MAS rotor equipped with custom-built end-caps to prevent leakage.

5.2.3 NMR spectroscopy

^{31}P NMR spectra were acquired on a Varian INOVA 500 MHz NMR spectrometer using a VARIAN T3 triple-resonance MAS probe. The magic angle and field homogeneity of the

spectrometer were optimized using KBr and adamantane, respectively, prior to each experiment. All spectra were collected at 10 °C.

^{31}P static NMR spectra were recorded at 202 MHz using a spin echo pulse sequence and TPPM proton decoupling[64]. Typical acquisition parameters were as follows: a 90° pulse length of 6.7 μs, an echo delay of 22.8 μs, a recycle delay of 4.0 s, a spectral width of 100 kHz, and a 1 K data size. On average, 1,000–2,000 transients were collected for each spectrum, and processed with an exponential multiplication equivalent to 100 Hz line broadening prior to Fourier transformation.

^{31}P CODEX MAS NMR spectra were acquired by spinning rotors at 6.5 kHz without proton decoupling. Spectra were obtained in blocks of 128 scans per mixing time to ameliorate spectrometer drift. Typical acquisition parameters were as follows: a 90° pulse length of 6.7 μs, a recycle delay of 4.0 s, a dephasing/rephasing train of three 180° pulses (∼0.3 ms), a spectral width of 16 kHz, and a 2 K data size. Typically, 4096 transients were collected for each spectrum, and processed with an exponential multiplication equivalent to 15 Hz line broadening and 4 K zero-filling prior to Fourier transformation.

Pulsed field gradient (PFG) ^{1}H NMR diffusion spectra were recorded on the same 500 MHz NMR spectrometer as above but using a double resonance liquid probe with gradient coils along the z-direction. Gradient strength was calibrated from the known diffusion coefficient of HOD at 25 °C.[65] The stimulated echo (STE) version of the PFG NMR diffusion experiment[27] was employed with square gradient pulses of constant duration (5 ms) and variable gradient pulse amplitude. Typical acquisition parameters are as follows: a 90° pulse length of 21 μs, a spin echo delay of 20 ms, a stimulated echo delay of 50 ms, a recycle delay of 1 s, a spectral width of

10 kHz and a 32 K data size. Spectra were processed with an exponential multiplication equivalent to 1 Hz line broadening prior to Fourier transformation.

From a comparison of the measured diffusion coefficient of water in the LUV suspensions (D_{LUV}) versus that of bulk water at the corresponding temperature (D_o) an effective viscosity η_{LUV} of the LUV suspension was calculated via the relationship:

$$\boldsymbol{\eta_{LUV} = \eta_o \left(\frac{D_o}{D_{LUV}} \right)} \qquad \text{Equation 19}$$

where η_o is the viscosity of water at 10 °C.

5.2.4 DLS

A Malvern Zetasizer NanoZS (Malvern Instruments Ltd., Worcestershire, UK) was used to record the LUV size, mean size and PDI. The solvent parameters for the sucrose buffer were generated using the NanoZS software and size calibration beads were used to confirm accuracy. A plastic cuvette was used for all measurements at a temperature of 25 °C. The samples were also run at temperatures from 5 to 10 °C to confirm that the liposome size was invariant to temperature.

5.3 Results and discussion

5.3.1 LUV properties relevant to ^{31}P CODEX

The ^{31}P CODEX pulse sequence used in these measurements is shown in Figure 5-1. It is modified relative to the conventional CODEX experiment in that a single 90° direct excitation

pulse is employed rather than ^{1}H cross polarization. The phase tables were modified accordingly as per Wachowicz et al.[66]. Proton decoupling was not employed since little, if any, improvement in the ^{31}P line width was obtained regardless of the decoupling scheme used. This is consistent with the fact that ^{1}H–^{31}P dipolar couplings in liquid-crystalline phosphatidylcholine bilayers range from 1 to 6 kHz[67] and, thus, are already significantly reduced by MAS at 6.5 kHz.

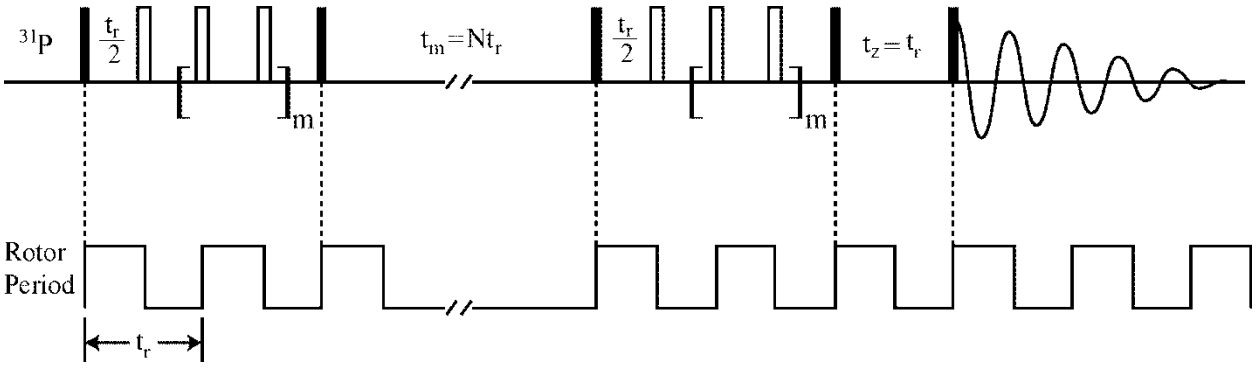

Figure 5-1: The ^{31}P CODEX NMR pulse sequence used in this study. This pulse sequence was adapted from deAzevedo et al.[59] Direct excitation, rather than cross polarization, was employed. No proton decoupling was necessary. The number of 180° pulses applied during a given recoupling period equaled m + 1, where m = 0, 1, 2, etc., each 180° pulse being separated by one half rotor period ($t_r/2$). The mixing time $t_m = Nt_r$ was a multiple (N) of the rotor period (t_r). A z-filter of duration $t_z = t_r$ was inserted prior to acquisition.

In CODEX, the CSA is recoupled during the "dephasing" period through 180° pulses placed at intervals of one-half the rotor period, $t_r/2$. For phospholipids in spherical vesicles, each becomes "labelled" with a phase angle dictated by the ^{31}P chemical shift corresponding to the orientation, β, of that phospholipid's long molecular axis with respect to the principle magnetic field, according to:

$$\upsilon_\beta = \frac{2}{3}(\upsilon_\parallel - \upsilon_\perp)\frac{1}{2}(3\ \cos^2\beta - 1) \qquad \text{Equation 20}$$

where $\Delta\upsilon_{CSA} = (\upsilon_{\parallel} - \upsilon_{\perp}) \approx 45$ ppm is the axially symmetric, residual ^{31}P CSA for phosphatidylcholine in a liquid-crystalline bilayer. During the mixing time, t_m, lateral diffusion around the radius of curvature of the spherical vesicle can alter that orientation. Consequently, during the subsequent "rephasing" period the phase angle developed due to CSA recoupling will not match that acquired during the initial dephasing period, resulting in reduced signal intensity.

In order that CODEX functions properly, the correlation time for the molecular motion, τ_c, must fall within certain limits, specifically: $t_r \ll \tau_c \ll t_m$. Clearly, unless the motional correlation time is shorter than the mixing time, no reorientation will take place during the mixing time and no signal attenuation will be observed. Conversely, unless the motional correlation time is longer than the rotor period, significant molecular reorientation will occur during the recoupling period, thereby degrading the ability to recouple the CSA. Other experimental constraints arise from relaxation considerations, specifically: $t_r \ll T_2$ and $t_m \ll T_1$.

Reorientation of a phospholipid within a spherical lipid bilayer vesicle relative to the magnetic field direction can occur through lateral diffusion around the vesicle's radius of curvature and from overall tumbling of the vesicle in solution. The effective motional correlation time then becomes a function of the correlation times for lateral diffusion, τ_{ld}, and vesicle tumbling, τ_{tm}.[68]

$$\frac{1}{\tau_c} = \frac{1}{\tau_{ld}} + \frac{1}{\tau_{tm}} \qquad \text{Equation 21}$$

These respective correlation times for spherical vesicles are,

$$\tau_{ld} = r^2 / 6D_L \qquad \text{Equation 22}$$

$$\tau_{tm} = 4\pi r^3 \eta_{sol} / 3k_B T \qquad \text{Equation 23}$$

where r is the vesicle radius, D_L is the lipid's lateral diffusion coefficient, η_{sol} is the solution viscosity and $k_B T$ is the Boltzmann temperature. Hence, it is essential to determine the vesicle radius if the lateral diffusion coefficient is to be measured via CODEX.

Figure 5-2 shows the distribution of vesicle radii obtained via DLS for 100% POPC LUVs, while Table 1 summarizes results obtained for all three different LUV compositions of interest here. The extruded LUV mean radius increased in the order POPC:POPG (70:30, mol/mol) < 100% POPC < POPC:CHOL (70:30, mol/mol), but in all cases fell near 100 nm, while the distribution of radii was reasonably monodisperse (PDI < 0.2). This particular vesicle size regime was chosen in order to maximize the surface/volume ratio of LUVs within the sample rotor: larger unilamellar vesicles close packed into the same volume would contain fewer phospholipids. Note that DLS analysis of LUV size yielded identical results before and after concentration by centrifugation and being subject to spinning for a number of hours in the rotor of the MAS probe for CODEX experiments.

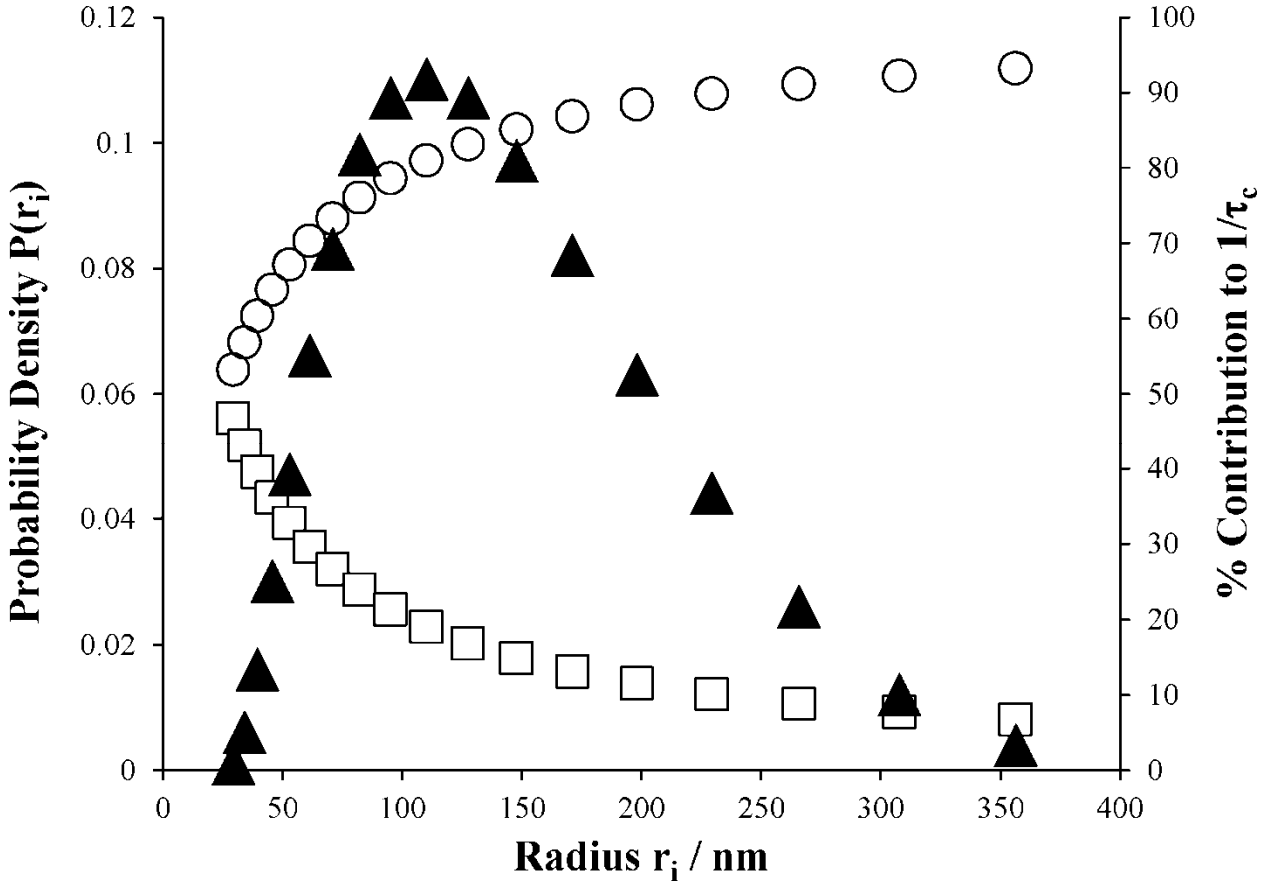

Figure 5-2: LUV size distribution and corresponding phospholipid re-orientation motional rates in 100% POPC vesicles. The normalized probability density $P(r_i)$ (▲), as a function of vesicle radius r_i was obtained via DLS in 200 mM sucrose, 20 mM KCl, 10 mM HEPES, pH 7.4. Identical results were obtained before and after CODEX measurements. The percent contributions at 10 °C to the overall rate of phospholipid re-orientational motion $1/\tau_c$ due to vesicle rotational tumbling $1/\tau_{tm}$ (□) and phospholipid lateral diffusion $1/\tau_{ld}$ (○) were calculated using Equation 21, Equation 22 and Equation 23, assuming a lateral diffusion coefficient $D_L = 3.2 \times 10^{-12}$ m^2 s^{-1} independent of vesicle radius, and an effective viscosity of 1.9 cP (see 5.3.1).

Table 5-1: LUV Properties and Phospholipid Lateral Diffusion Coefficients. The Z-radius and PDI were measured via DLS. The correlation time τ_c was obtained from fitting experimental ^{31}P CODEX decay curves, assuming a single exponential decay function. The lateral diffusion coefficient D_L was extracted from experimental ^{31}P CODEX decay curves, taking into account the distribution of vesicle radii in each individual LUV preparation, as determined via DLS. An effective correlation time for each vesicle size for an assumed D_L was calculated as per Equation 21, Equation 22 and Equation 23, and fitted via Equation 28 to the experimental data via a least squares analysis to obtain the best value of the lateral diffusion coefficient.

Property	LUV Composition (mol:mol)		
	POPC 100	POPC:CHOL 70:30	POPC:POPG 70:30
Z-radius / nm	96.14	117.3	75.89
PDI	0.195	0.198	0.160
τ_c / ms	0.66 ± 0.03	1.09 ± 0.06	0.77 ± 0.02 (0.42)[a]
D_L / 10^{-12} m^2s^{-1}	3.2	2.7	0.9 (2.5)[a]
Decay Limit (b)	0.05	0.10	0.10 (0.20)[a]

[a] Value in parentheses is for POPG and has a large associated error due to signal-to-noise limitations.

This vesicle radius size regime, however, is such that, at room temperature, the combined contributions of vesicle tumbling and lateral diffusion are sufficient to produce significant motional averaging of the residual ^{31}P CSA. Specifically, assuming <r> ≈ 100 nm, with typical room temperature values of $D_L \approx 2.0 \times 10^{-11}$ m^2 s^{-1} and $\eta_{sol} \approx 0.89$ cP, the equations

yield a re-orientation motional correlation time of approximately 76 μs. This is intermediate to the time scale defined by the inverse of the ^{31}P residual CSA for liquid-crystalline phosphatidylcholine: $1/\Delta\upsilon_{CSA}$ ≈ 1/45 ppm = 1/9090 Hz (at 202 MHz) ≈ 110 μs.

The effects of such intermediate time scale motions are evident in the static ^{31}P NMR spectrum in Figure 5-3A, obtained with 100% POPC LUVs at 25 °C. The spectrum consists of a broad line shape centred on the isotropic ^{31}P NMR frequency, exhibiting an overall width somewhat less than 45 ppm, with evident loss of definition at the spectral shoulders. CODEX will function poorly under these circumstances because $t_r \approx \tau_c$ ($t_r = 1/\upsilon_r$ = 1/6500 Hz = 154 μs).

To circumvent this, we prepared the LUVs in 200 mM sucrose and performed measurements at 10 °C. PFG ^{1}H NMR diffusion measurements on the water in such samples yielded an effective viscosity of 1.9 cP (data not shown). An estimate of the effective re-orientation motional correlation time, assuming $D_L \approx 1 \times 10^{-12}$ m^2 s^{-1}, predicts $\tau_c \sim 1$ ms under such conditions of temperature and viscosity, which would be slow on the time scale of the inverse of the residual ^{31}P CSA. Indeed, the static ^{31}P NMR spectrum that results, as shown in Figure 5-3B, exhibits a powder pattern line shape far better defined than that in Figure 5-3A, with the residual CSA ($\Delta\upsilon_{CSA}$ = 45 ppm) expected for liquid-crystalline phospholipids in a bilayer vesicle undergoing overall slow re-orientational motions, i.e., $\tau_c > 1/\Delta\upsilon_{CSA}$. Hence, ^{31}P CODEX should be feasible under these circumstances.

For reference purposes, Figure 5-3C shows a static ^{31}P NMR spectrum of DMPC, formulated as LMVs. The spectrum was acquired at 10 °C, a temperature well below DMPC's gel-to-liquid-crystalline phase transition temperature of 24 °C.[69] The well-defined powder pattern line shape exhibits a residual CSA on the order of 60 ppm. At this gel phase temperature, individual DMPC molecules still undergo rapid rotational motions about their long

axes perpendicular to the bilayer normal, but lateral diffusion slows profoundly due to packing constraints such that $D_L < 1 \times 10^{-14}$ m^2 s^{-1}. Given that the radius of such LMVs will exceed 1 µm, an effective re-orientational motional correlation time on the order of tens of seconds is predicted, a point which will become relevant below.

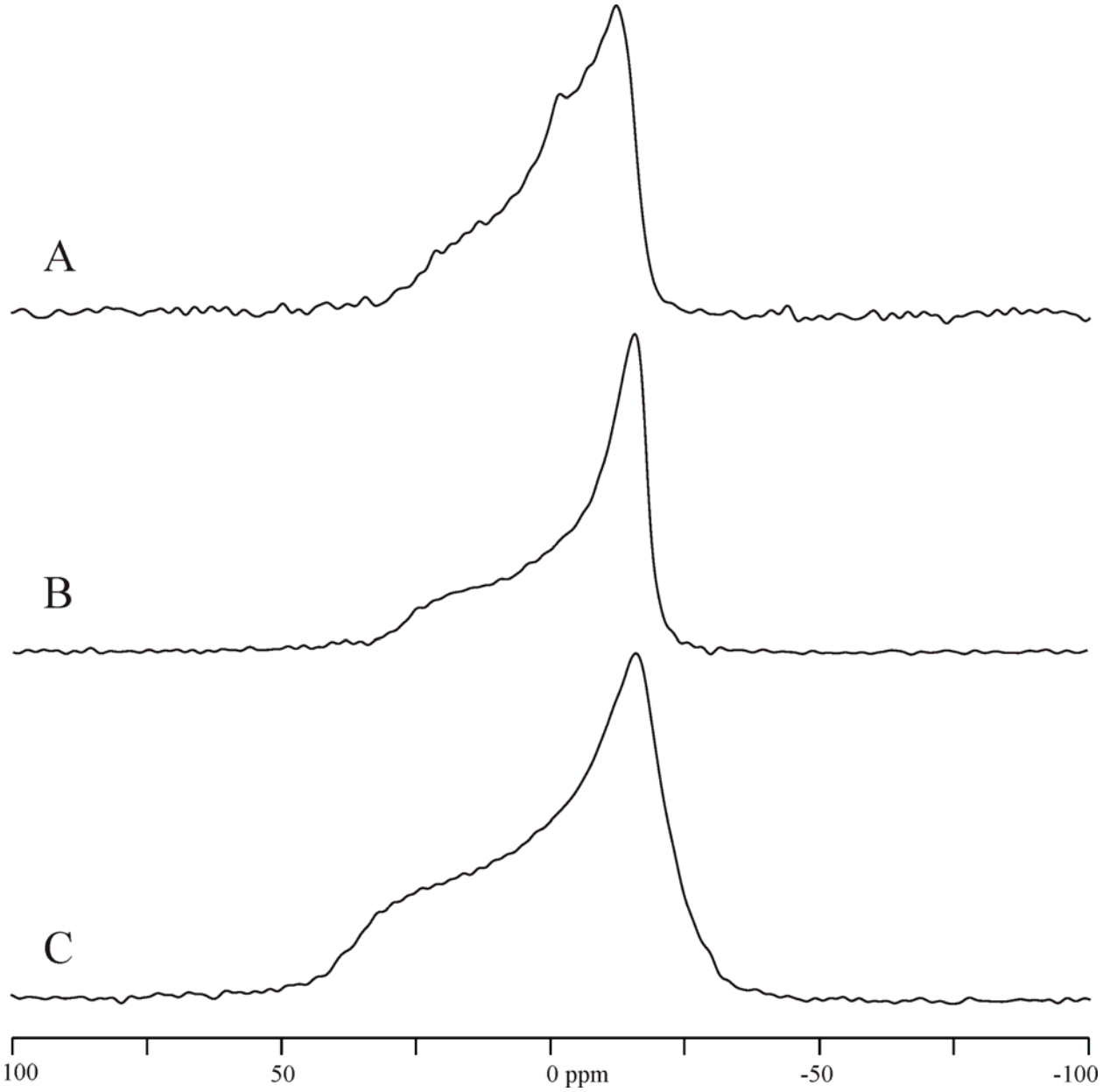

Figure 5-3: Static ^{31}P NMR spectra of various phosphatidylcholine vesicular preparations. (A) 100% POPC LUVs prepared in 20 mM KCl, 10 mM HEPES, pH 7.4 and acquired at 25 °C. (B) 100% POPC LUVs prepared in 200 mM sucrose, 20 mM KCl, 10 mM HEPES, pH 7.4 and acquired at 10 °C. (C) 100% DMPC LMVs prepared in 20 mM KCl, 10 mM HEPES, pH 7.4 and acquired at 10 °C.

5.3.2 ^{31}P CODEX intensity decays for LUV phospholipids

Figure 5-4A shows a series of ^{31}P CODEX spectra, obtained at 10 °C with 100% POPC LUVs prepared in 200 mM sucrose, as a function of increasing mixing time up to several ms. Under MAS at υ_r = 6500 Hz (t_r = 154 μs), only the isotropic resonance, i.e., centre-band, remains since $\upsilon_r > \left(\frac{2}{3}\right) \Delta\upsilon_{CSA}$. The line-width-at-half height (60 Hz) suggests a transverse relaxation time, T_2, on the order of 5.3 ms, so that $t_r \ll T_2$ as required. Inversion recovery measurements of longitudinal relaxation indicate that $T_1 \sim 700$ ms (data not shown), so that the condition $t_m \ll T_1$ applies. Hence, the intensity decay with increasing mixing time evident in Figure 5-4A can be attributed to phospholipid re-orientational motions, including lateral diffusion, in accord with the estimate $\tau_c \sim 1$ ms under such conditions of temperature and viscosity.

Figure 5-4B shows a similar series of ^{31}P CODEX spectra, obtained at 10 °C with POPC:POPG (70:30, mol/mol) LUVs, also prepared in 200 mM sucrose, as a function of increasing mixing time. Here, separate resonances are readily resolved for the POPC and POPG phospholipid species, separated by roughly 1 ppm. Both undergo substantial intensity decay with increasing mixing time, so that their respective lateral diffusion coefficients may be characterized simultaneously and independently.

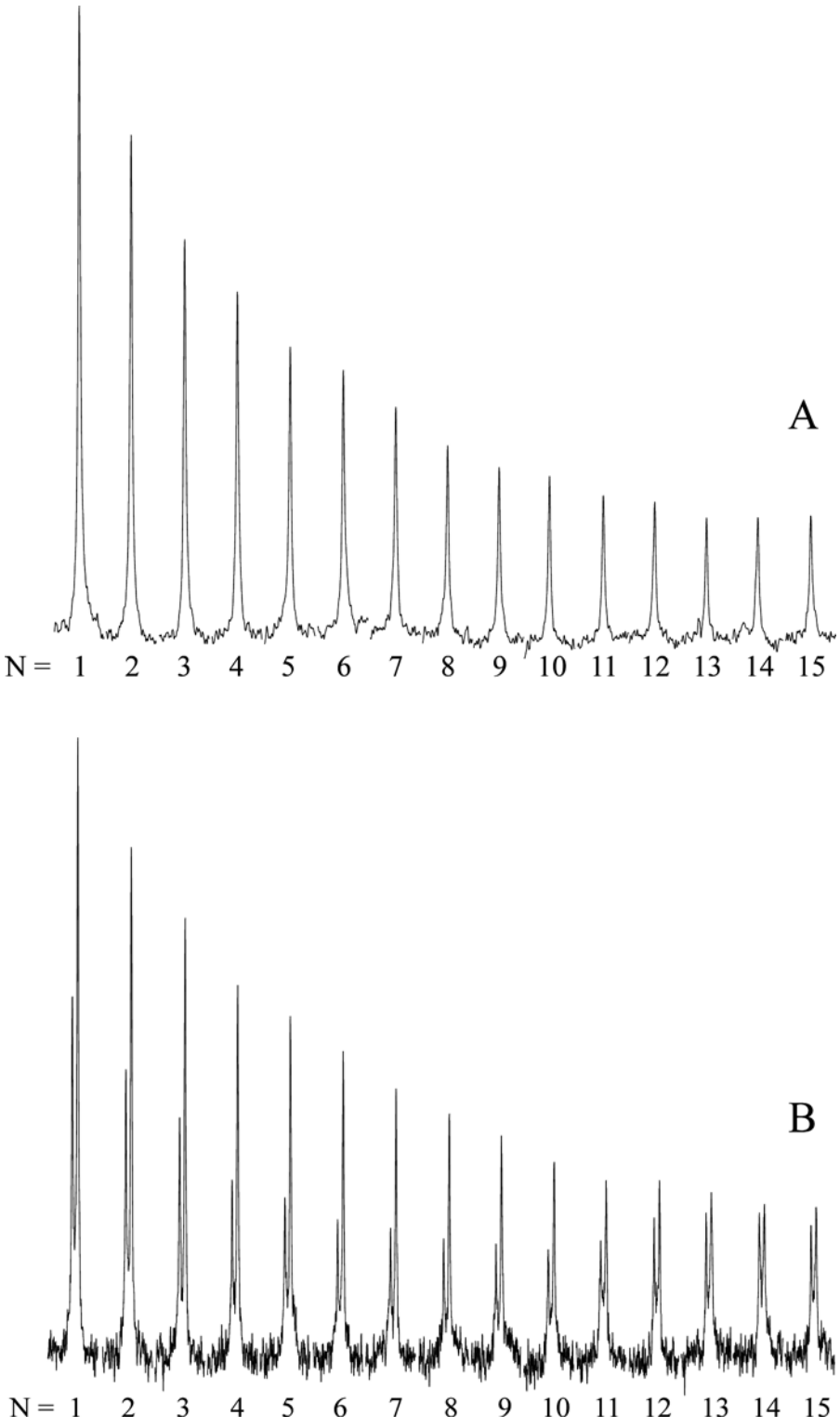

Figure 5-4: ^{31}P CODEX NMR spectra (m = 1) as a function of increasing mixing time tm = Ntr, where t_r = 154 µs is the MAS rotor period at υ_r = 6500 Hz, for (A) 100% POPC LUVs in 200 mM sucrose, 20 mM KCl, 10 mM HEPES, pH 7.4 at 10 °C, and (B) 70:30 POPC:POPG LUVs in 200 mM sucrose, 20 mM KCl, 10 mM HEPES, pH 7.4 at 10 °C. The POPC and POPG isotropic resonances in (B) are separated by 1.0 ppm.

In CODEX, the correlation time of re-orientational motion may be extracted by incrementing the mixing time, t_m, as per the spectra in Figure 5-4, and fitting the resulting intensity decay to an appropriate function. Alternately, CODEX can provide information on the amplitude of that motion by incrementing the length of the CSA recoupling cycles, nt_r, where n = 2(m + 1). As described by Hackel et al.[70], the final signal intensity may be factored as:

$$S(nt_r, t_m) = f^{int} exp\left(-\frac{nt_r}{T_2^{RC}}\right) f^{slow} exp\left(-\frac{t_m}{T_1}\right) \qquad \text{Equation 24}$$

where f^{int} and f^{slow} correspond to the signal decays due to intermediate and slow motions during the recoupling cycles and the mixing time, respectively. To normalize for signal loss during the mixing period due to longitudinal relaxation, a second reference experiment is performed in which the mixing time and the final z-filter (duration $t_z = t_r$) are interchanged, resulting in a signal,

$$S_0(nt_r, t_z) = f^{int}(nt_r) exp\left(-\frac{nt_r}{T_2^{RC}}\right) exp\left(-\frac{t_z}{T_1}\right) \qquad \text{Equation 25}$$

so that the ratio of the two signals contains information concerning only the slow motions.

$$\frac{S(nt_r, t_m)}{S_0(nt_r, t_z)} = f^{slow} \qquad \text{Equation 26}$$

In our measurements, the intensity of all reference spectra were virtually identical, even at the extremes of the range of mixing times examined ($t_m \leq 10$ ms), in accord with the large relative value of the ^{31}P spin-lattice relaxation time of the phospholipids, $T_1 \approx 700$ ms.

Intensity decay during the recoupling cycles can arise from T_2 relaxation effects, combined with errors in pulse timings, durations or phases, as well as the presence of

intermediate time scale motions, f^{int}. As shown in Figure 5-5 for the case of 100% POPC LUVs (200 mM sucrose, 10 °C), there is a rapid and pronounced decrease in the initial intensity $S_0(nt_r, t_z)$ with increasing n. Other phospholipid compositions yielded similar results. To separate out effects due to T_2^{RC} (into which factor are subsumed all effects due to rf errors) from those due to intermediate time scale motions, we performed the same measurement on DMPC LMVs at 10 °C, where lateral diffusion and vesicle tumbling are sufficiently slow as to eliminate intermediate time scale re-orientational motions. As seen in Figure 5-5, the intensity decrease with increasing n is far less steep in this case, indicating the likely presence of intermediate time scale motions in the case of the POPC LUV samples. A comparison of the recoupling times versus the estimated correlation time for re-orientational motion confirms this interpretation. Specifically, the total CSA recoupling time is $nt_r = 2t_r(m + 1)$, equal to 0.308, 0.616 and 0.924 ms for m = 0, 1 and 2, respectively, given υ_r = 6500 Hz. These are clearly increasingly significant fractions of the estimated motional correlation time $\tau_c \approx 1$ ms.

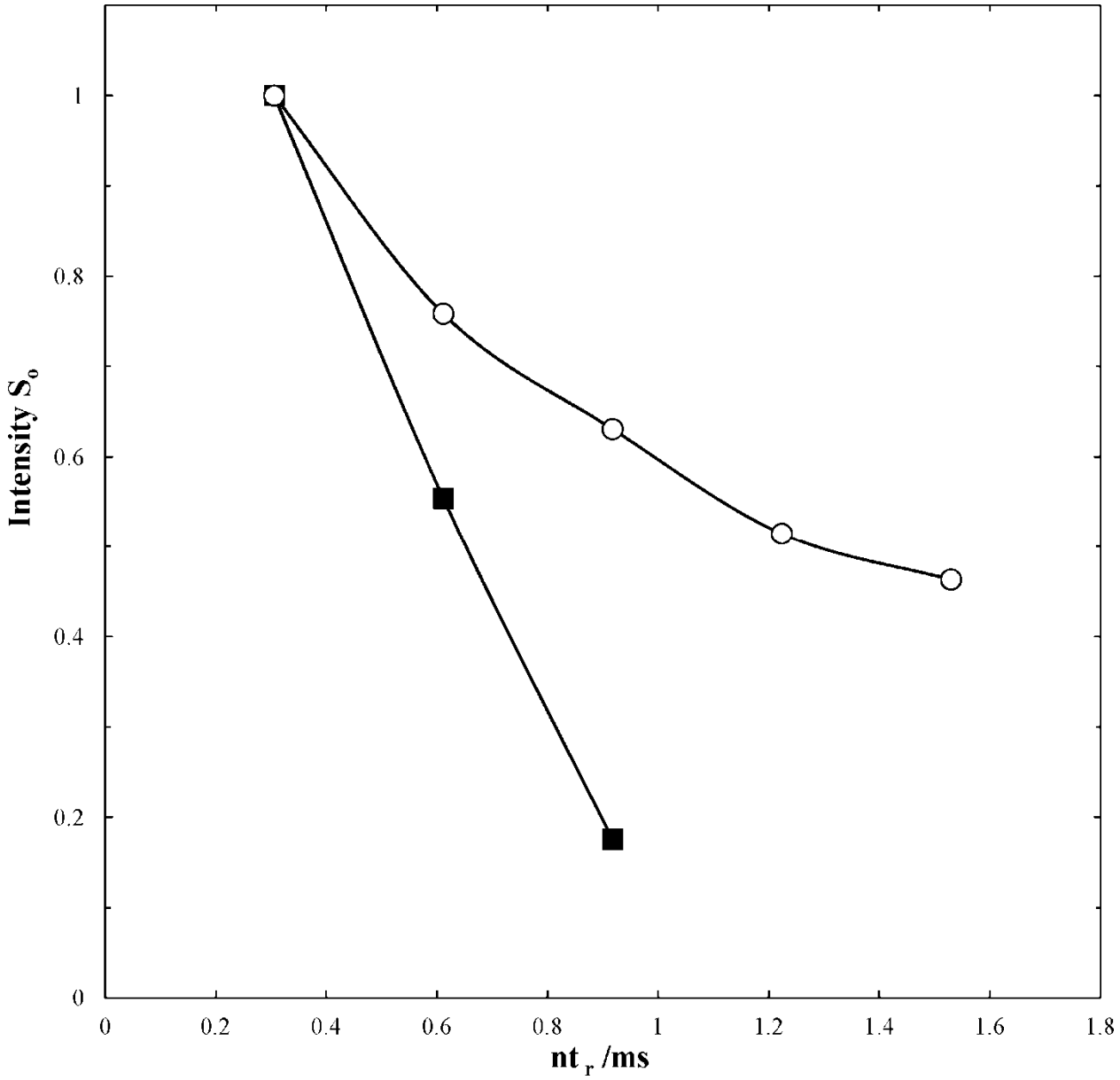

Figure 5-5: ^{31}P CODEX S_0 signal for 100% POPC LUVs in 200 mM sucrose, 20 mM KCl, 10 mM HEPES, pH 7.4 at 10 °C (■) and 100% DMPC MLVs in 20 mM KCl, 10 mM HEPES, pH 7.4 at 10 °C (○). Both as a function of the total CSA recoupling time $nt_r = 2t_r(m + 1)$ with minimal mixing time $t_m = t_r$.

To render CODEX ideally sensitive to the motion under investigation, recoupling of the CSA should be optimized.[59,60] Figure 5-6 compares the normalized intensity S/S_0 versus the mixing time curves for m = 0, 1 and 2, as obtained with 100% POPC LUVs (200 mM sucrose, 10 °C). For the case m = 0, recoupling of the CSA was incomplete, in that the equilibrium intensity

measured at longer mixing times never falls below 60–70% of the initial intensity. For the case m = 1 (corresponding to the spectra shown in Figure 5-4A) the intensity decayed smoothly to an equilibrium value of less than 20% of the initial intensity at a mixing time on the order of 2 ms, indicating strong recoupling of the CSA. Little or no further intensity decrease was attained by extending the mixing time to 10 ms (data not shown). In the case m = 2, no further recoupling efficiency was achieved beyond that for the m = 1 case, while signal-to-noise was sacrificed as per Figure 5-5. Consequently, all subsequent CODEX measurements on LUVs were performed with m = 1.

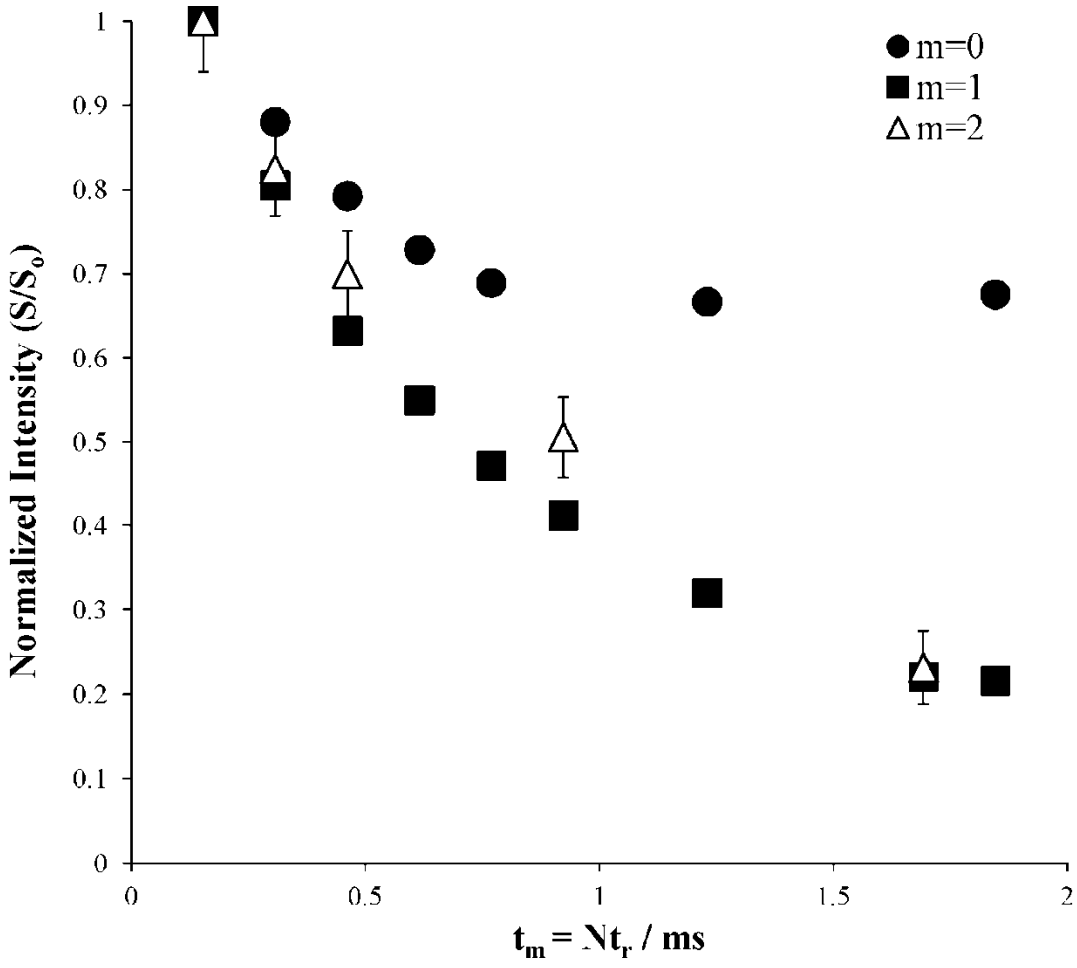

Figure 5-6: Normalized ^{31}P CODEX decay S/S_0 for 100% POPC LUVs in 200 mM sucrose, 20 mM KCl, 10 mM HEPES, pH 7.4 at 10 °C, as a function of the mixing time $t_m = Nt_r$ for different durations of the total CSA recoupling time $2t_r(m + 1)$.

5.3.3 Phospholipid lateral diffusion coefficients from ^{31}P CODEX decays

^{31}P CODEX decays for the different LUV compositions, all using m = 1, are compared in Figure 5-7. All appear to be characterized by a single correlation time and all approach a limiting intensity near, but not equal to, zero at long mixing times. The CODEX intensity at long mixing times, $t_m \rightarrow \infty$, can be related to the number of equivalent orientations M_M and the fraction of mobile sites, f_m, as per[59]:

$$\frac{S_\infty}{S_0} = (1 - f_m) + f_m/M_M \qquad \text{Equation 27}$$

For lateral diffusion of liquid-crystalline phospholipids around the radius of curvature of a bilayer vesicle, all phospholipids should be equally mobile, while the number of equivalent orientations is essentially infinite, predicting an equilibrium CODEX intensity of zero. However, it has been shown that in the presence of motions on the time scale of the recoupling period, CODEX (and other MAS recoupling techniques) will not exhibit the full amplitude of intensity difference between vanishingly short versus long mixing times due to loss of correlation during the recoupling periods.[71] Hence, the observation that the limiting intensity plateaus at a value greater than zero is interpreted as another manifestation of the presence of intermediate time scale motions in these LUV samples.

Since the effective correlation time of re-orientational motion for LUV phospholipids is influenced by both lateral diffusion and vesicle tumbling, each of which depend on the vesicular radius, and since there is a distribution of vesicular radii in such samples, as per Figure 5-2, the CODEX decay is a superposition of contributions from individual vesicles,

$$\frac{S(nt_r, t_m)}{S_0(nt_r, t_z)} = \frac{\sum_i P(r_i)\left[exp\left(-\frac{t_m}{\tau_{c_i}}\right)\right]}{\sum_i P(r_i)\left[exp\left(-\frac{t_z}{\tau_{c_i}}\right)\right]} + b \qquad \text{Equation 28}$$

where $P(r_i)$ is the probability density for a particular vesicle radius as derived from DLS, and τ_{c_i} is the corresponding re-orientational correlation time calculated from Equation 21, Equation 22 and Equation 23, assuming that the lateral diffusion coefficient is independent of vesicular radius. The term *b* accounts for the non-zero equilibrium intensity at long mixing times and is assumed to be independent of vesicle radius to a first approximation. Using a non-linear least squares analysis, the ^{31}P CODEX decays were fit with the lateral diffusion coefficient and the quantity b as the sole fitting parameters. Examples of the quality of such fits are shown in Figure 5-7.

Under rapid MAS the g-forces generated can alter lipid hydration and change vesicle shape. However, at the relatively low speeds employed in this study (6500 Hz), Zhou et al.[72] have shown that the small change in hydration levels that results should bring about no significant change in lipid dynamics or vesicle structure, a conclusion confirmed by Nagle et al.[73]. Consequently, we assume that the DLS results shown in Figure 5-2 and Table 5-1 are applicable.

Lateral diffusion coefficients extracted from the CODEX decays are listed in Table 5-1. For 100% POPC LUVs the lateral diffusion coefficient agrees well with literature values at similar temperatures.[74,75]

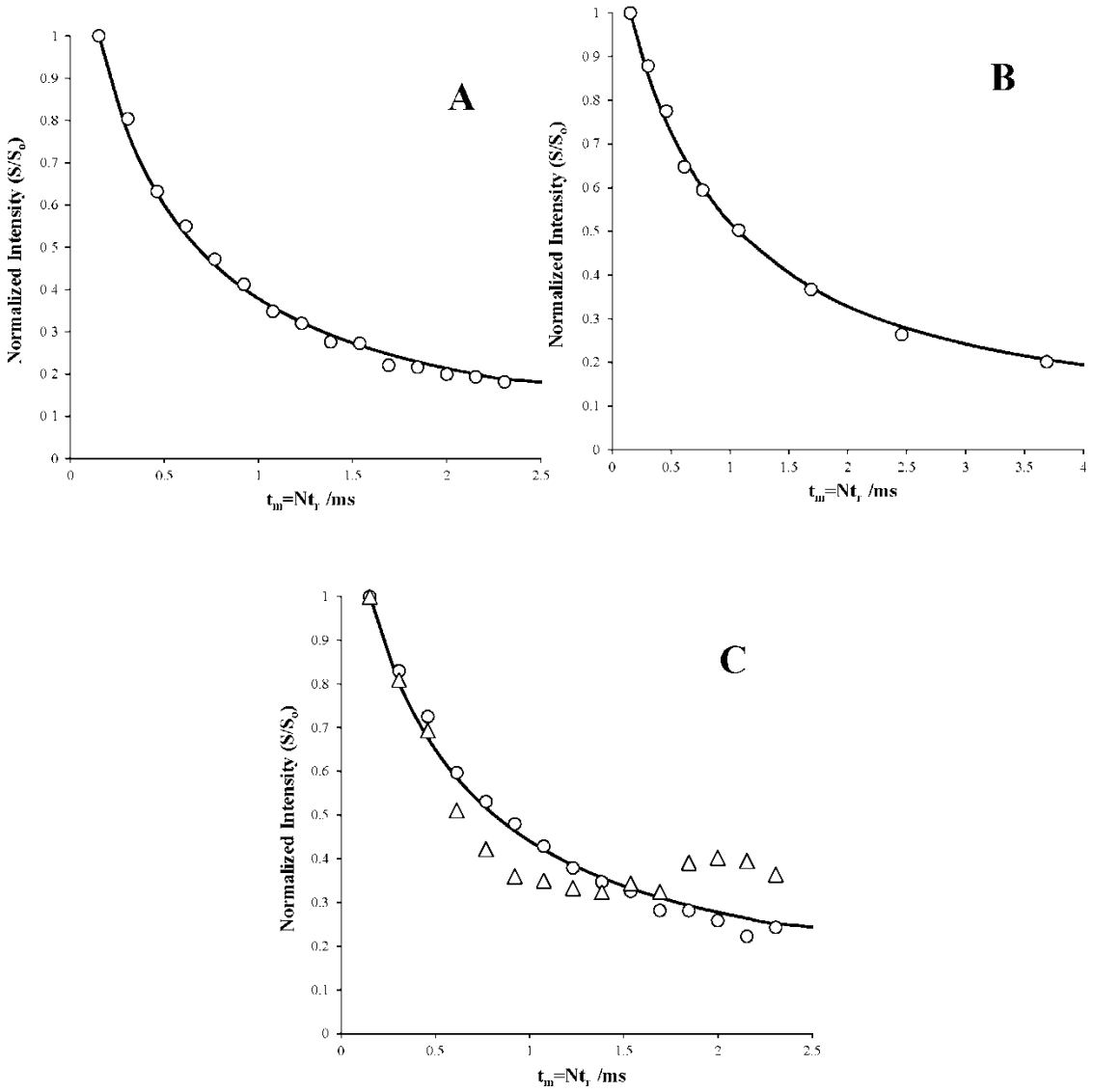

Figure 5-7: Normalized ^{31}P CODEX decay S/S_0 for (A) 100% POPC LUVs, (B) 70:30 POPC:CHOL LUVs, and (C) 70:30 POPC:POPG LUVs (○, POPC; △, POPG). All LUVs were prepared in 200 mM sucrose, 20 mM KCl, 10 mM HEPES, pH 7.4. All data were acquired at 10 °C with m = 1. Lines of best fit were generated as described in the text with parameters listed in Table 5-1.

For POPC mixed with 30 mol % CHOL, one expects slower lateral diffusion than in the absence of CHOL[76], due to the rigidifying effect of the latter, and this expectation is borne out qualitatively by the CODEX data. Addition of CHOL can cause phase separation into so-called liquid-ordered and liquid-disordered phases. For 30 mol % CHOL mixed with DMPC, for example, the liquid-disordered phase exhibits somewhat slower lateral diffusion, while that of

the liquid-ordered phase is profoundly slower[77]. For 30 mol % CHOL mixed with POPC, however, the bilayer lipids remain homogeneously mixed in a liquid-disordered phase, at least at room temperature and above.[76] That the CODEX decay for the 70:30 POPC:CHOL mixture at 10 °C exhibited no evidence of the presence of two phases with different lateral diffusion coefficients indicates that a single phase extends down to this temperature. The differential decrease in lateral diffusion with CHOL diminishes, however, with decreasing temperature[76], which may explain the relatively mild effect of CHOL observed here.

In POPC:POPG LUVs, lateral diffusion of POPC was dramatically slower than in 100% POPC or POPC:CHOL LUVs. Due to signal-to-noise limitations, the POPG CODEX decay exhibited large uncertainties, particularly obvious at longer mixing times, and could not be reliably fit with a single exponential function. At shorter mixing times, where signal-to-noise was less of an issue, the POPG diffusive decay, and the extracted lateral diffusion coefficient, at least approximately mirrored that of POPC in the same mixture.

Slower lateral diffusion in POPC:POPG mixtures has been reported recently.[78] Also, molecular dynamics simulations indicate that the POPG glycerol head group has a strong propensity to form intermolecular hydrogen-bonds both with other POPG molecules[79,80] and with POPC[80]. The resulting reduction in free area per lipid, and the greater effective size of the diffusing unit, would conspire then to decrease rates of lateral diffusion. The presence of sucrose in our LUV preparations is a complicating factor here, since sucrose hydrogen bonds readily and POPG is an excellent candidate for such interactions. It would be essential, therefore, to compare directly the POPC and POPG lateral diffusion coefficients in the presence and absence of sucrose before drawing further conclusions. A further possible factor is the

condensation of cations at the bilayer surface, attracted by the anionic surface charge, which may also slow lateral diffusion by reducing the effective area per lipid.[79,81]

5.3.4 ^{31}P CODEX relative to other NMR lateral diffusion techniques

Relative to 2D EXSY NMR lateral diffusion methods, ^{31}P CODEX compares favourably with respect to resolution, experiment time and ease of extracting the lateral diffusion coefficient. Specifically, the fast MAS employed in CODEX permits ready resolution of different phospholipid species. This is difficult, if not impossible, with static 2D EXSY, since the typical fluid phospholipid ^{31}P residual CSA of ~45 ppm is far larger than the typical difference in isotropic chemical shift (~1–5 ppm) between different phospholipid species.

A CODEX data set can be obtained in a fraction of the experiment time required for static 2D EXSY measurements. In the latter case, for any one mixing time, a two-dimensional powder spectrum is acquired with spectral intensity spread over a wide range of frequencies. In CODEX, for any one mixing time, a one-dimensional spectrum is acquired with all spectral intensity focused under the isotropic resonance, thus accumulating sufficient signal far more rapidly than 2D EXSY.

Extracting the lateral diffusion coefficient from a CODEX data set is a straightforward process of curve fitting. For 2D EXSY spectra, however, the entire 2D spectra must be simulated at each mixing time.

Both approaches require knowledge of the vesicle radius (and distribution thereof) in order to extract diffusion information. (Recent static 2D EXSY ^{31}P NMR and analogous 1D stimulated echo exchange experiments exploited this dependence on vesicle radius to examine the effects of various antimicrobial peptides on bilayer curvature, as many such peptides

compromise bilayer integrity through pore formation and/or bilayer thinning effects.[82–84] In 2D EXSY lateral diffusion measurements, vesicle size was controlled by assembling lipid bilayers on glass beads of known size.[51–53] However, for such glass-bead-supported lipid bilayers, the inner bilayer leaflet has limited hydration, which compromises lateral mobility. The LUVs used in our CODEX measurements suffer no such problem.

Relative to the various gradient-based ^{1}H NMR technique for measuring lateral diffusion, however, ^{31}P CODEX is insensitive, since the magnetogyric ratio of ^{31}P is roughly 40% that of ^{1}H. Further, there are many membrane-associated molecular species of interest that do not contain a phosphorus atom. However, in principle, CODEX spectra could be obtained with other nuclei, such as ^{13}C and ^{15}N. While the same applies to the gradient-based methods, proton decoupling of heteronuclei during gradient pulses can be problematic.[85] CODEX would suffer no such problem.

5.4 Conclusions

The use of ^{31}P CODEX NMR to determine lateral diffusion coefficients of phospholipids in LUVs was demonstrated. The particular advantages of this approach include the avoidance of any need for specific labelling of the species of interest and the ability to resolve and measure lateral diffusion of different phospholipid species simultaneously.

A number of potential improvements to the ^{31}P CODEX lateral diffusion measurement technique as implemented here are apparent. Foremost is that the presence of intermediate time scale motions cause loss of signal intensity during the recoupling periods, necessitating extensive signal-averaging to produce adequate signal-to-noise. Such signal loss can be exacerbated by rf-related imperfections during the recoupling periods. Employing the CONTRA

(Constant Time Recoupling of Anisotropies) variant of CODEX[86], which is significantly less sensitive to rf-imperfections, might mitigate this issue.

A sure means to avoid intermediate time scale motions is to use GUV, where the larger vesicular radius slows the effective correlation time for re-orientational motion to the point that $\tau_c \gg t_r$. For example, at room temperature, assuming a normal aqueous viscosity, for a GUV of radius 1 μm the vesicle tumbling correlation time would be on the order of minutes, while the lateral diffusion correlation time would be on the order of ten milliseconds, or a factor of roughly 50 times greater than the rotor period at 6500 Hz. Experiments to test the efficacy of these potential improvements are currently underway.

While it would be desirable to apply ^{31}P CODEX NMR to measure lateral diffusion in natural membranes, i.e., in whole cells or isolated cellular or sub-cellular membranes, one recognizes that any such attempt would face challenges not present in model membranes of defined composition and geometry. Specifically, in whole cells the NMR signals would be a superposition of signals from different membranes, i.e., plasma, endoplasmic reticulum, mitochondrial, etc., each with a distinctive composition and, often, a decidedly non-spherical geometry. Even isolated membranes present challenges. Red blood cell ghosts, for instance, exist as a mix of smooth and crenated spheres and discs of around 10 μm.[87–89] Since the model used in the analysis of our ^{31}P CODEX NMR data assumes a spherical membrane geometry, substantial modification would be necessary in order to apply the technique in such non-ideal cases.

5.5 References

(1) Glaser, M. *Curr. Opin. Struct. Biol.* **1993**, *3*, 475–481.

(2) Albertsson, P.-A. *Photosynth. Res.* **1995**, *46*, 141–149.

(3) Somerharju, P.; Virtanen, J. A.; Cheng, K. H. *Biochim. Biophys. Acta, Mol. Cell Biol. Lipids* **1999**, *1440*, 32–48.

(4) Vaz, W. L. C.; Melo, E. *J. Fluoresc.* **2001**, *11*, 255–271.

(5) Lommerse, P. H. M.; Spaink, H. P.; Schmidt, T. *Biochim. Biophys. Acta, Biomembr.* **2004**, *1664*, 119–131.

(6) Day, C. A.; Kenworthy, A. K. *Biochim. Biophys. Acta, Biomembr.* **2009**, *1788*, 245–253.

(7) Jacobson, K.; Zhang, F.; Tsay, T. T. *Scanning Microsc.* **1991**, *5*, 357–362.

(8) Reits, E. A. J.; Neefjes, J. J. *Nat. Cell Biol.* **2001**, *3*, E145–E147.

(9) Klonis, N.; Rug, M.; Harper, I.; Wickham, M.; Cowman, A.; Tilley, L. *Eur. Biophys. J.* **2002**, *31*, 36–51.

(10) Mullineaux, C. W. *J. Exp. Bot.* **2004**, *55*, 1207–1211.

(11) Rayan, G.; Guet, J.-E.; Taulier, N.; Pincet, F.; Urbach, W. *Sensors* **2010**, *10*, 5927–5948.

(12) Kahya, N.; Schwille, P. *Mol. Membr. Biol.* **2006**, *23*, 29–39.

(13) Kolin, D.; Wiseman, P. *Cell Biochem. Biophys.* **2007**, *49*, 141–164.

(14) Macháň, R.; Hof, M. *Int. J. Mol. Sci.* **2010**, *11*, 427–457.

(15) He, H.-T.; Marguet, D. *Annu. Rev. Phys. Chem.* **2011**, *62*, 417–436.

(16) Ritchie, K.; Iino, R.; Fujiwara, T.; Murase, K.; Kusumi, A. *Mol. Membr. Biol.* **2003**, *20*, 13–18.

(17) Chen, Y.; Yang, B.; Jacobson, K. *Lipids* **2004**, *39*, 1115–1119.

(18) Kusumi, A.; Nakada, C.; Ritchie, K.; Murase, K.; Suzuki, K.; Murakoshi, H.; Kasai, R. S.; Kondo, J.; Fujiwara, T. *Annu. Rev. Biophys. Biomol. Struct.* **2005**, *34*, 351–378.

(19) Kusumi, A.; Ike, H.; Nakada, C.; Murase, K.; Fujiwara, T. *Semin. Immunol.* **2005**, *17*, 3–21.

(20) Levi, V.; Gratton, E. *Cell Biochem. Biophys.* **2007**, *48*, 1–15.

(21) Kaji, N.; Tokeshi, M.; Baba, Y. *Chem. Rec.* **2007**, *7*, 295–304.

(22) Triller, A.; Choquet, D. *Neuron* **2008**, *59*, 359–374.

(23) Owen, D. M.; Williamson, D.; Rentero, C.; Gaus, K. *Traffic* **2009**, *10*, 962–971.

(24) Alcor, D.; Gouzer, G.; Triller, A. *Eur. J. Neurosci.* **2009**, *30*, 987–997.

(25) Pinaud, F.; Clarke, S.; Sittner, A.; Dahan, M. *Nat. Methods* **2010**, *7*, 275–285.

(26) Stejskal, E. O.; Tanner, J. E. *J. Chem. Phys.* **1965**, *42*, 288.

(27) Tanner, J. E. *J. Chem. Phys.* **1970**, *52*, 2523–2526.

(28) Stilbs, P. *Prog. Nucl. Magn. Reson. Spectrosc.* **1987**, *19*, 1–45.

(29) Kärger, J.; Pfeifer, H.; Heink, W. In *Advances in Magnetic Resonance*; Academic Press, Inc.: New York, 1988; Vol. 12, pp. 1–89.

(30) Price, W. S. *Concepts Magn. Reson.* **1997**, *9*, 299–336.

(31) Price, W. S. *Concepts Magn. Reson.* **1998**, *10*, 197–237.

(32) Maas, W. E.; Laukien, F. H.; Cory, D. G. *J. Am. Chem. Soc.* **1996**, *118*, 13085–13086.

(33) Gaede, H. C.; Gawrisch, K. *Biophys. J.* **2003**, *85*, 1734–1740.

(34) Scheidt, H. A.; Pampel, A.; Nissler, L.; Gebhardt, R.; Huster, D. *Biochim. Biophys. Acta* **2004**, *1663*, 97–107.

(35) Scheidt, H. A.; Huster, D.; Gawrisch, K. *Biophys. J.* **2005**, *89*, 2504–2512.

(36) Gaede, H. C.; Yau, W.-M.; Gawrisch, K. *J. Phys. Chem. B* **2005**, *109*, 13014–13023.

(37) Kimura, T.; Cheng, K.; Rice, K. C.; Gawrisch, K. *Biophys. J.* **2009**, *96*, 4916–4924.

(38) Polozov, I. V.; Gawrisch, K. *Biophys. J.* **2004**, *87*, 1741–1751.

(39) Polozov, I. V.; Bezrukov, L.; Gawrisch, K.; Zimmerberg, J. *Nat. Chem. Biol.* **2008**, *4*, 248–255.

(40) Lindblom, G.; Wennerstrom, H. *Biophys. Chem.* **1977**, *6*, 167–171.

(41) Orädd, G.; Lindblom, G. *Magn. Reson. Chem.* **2004**, *42*, 123–131.

(42) Orädd, G.; Lindblom, G. *Spectroscopy* **2005**, *19*, 191–198.

(43) Lindblom, G.; Gröbner, G. *Curr. Opin. Colloid Interface Sci* **2006**, *11*, 24–29.

(44) Lindblom, G.; Orädd, G. *J. Dispersion Sci. Technol.* **2007**, *28*, 55–61.

(45) Lindblom, G.; Orädd, G. *Biochim. Biophys. Acta, Biomembr.* **2009**, *1788*, 234–244.

(46) Ram, P.; Prestegard, J. H. *Biochim. Biophys. Acta, Biomembr.* **1988**, *940*, 289–294.

(47) Sanders II, C. R.; Prestegard, J. H. *Biophys. J.* **1990**, *58*, 447–460.

(48) Sanders II, C. R.; Schwonek, J. P. *Biochemistry* **1992**, *31*, 8898–8905.

(49) Soong, R.; Macdonald, P. *Biophys. J.* **2005**, *88*, 255–268.

(50) Macdonald, P. M.; Soong, R. *Can. J. Chem.* **2011**, *89*, 1021–1035.

(51) Fenske, D.; Jarrell, H. *Biophys. J.* **1991**, *59*, 55–69.

(52) Fenske, D. B.; Letellier, M.; Roy, R.; Smith, I. C. P.; Jarrell, H. C. *Biochemistry* **1991**, *30*, 10542–10550.

(53) Picard, F.; Paquet, M. J.; Dufourc, E. J.; Auger, M. *Biophys. J.* **1998**, *74*, 857–868.

(54) Dolainsky, C.; Unger, M.; Bloom, M.; Bayerl, T. M. *Phys. Rev. E* **1995**, *51*, 4743.

(55) Yang, Y.; Schuster, M.; Blümich, B.; Spiess, H. W. *Chem. Phys. Lett.* **1987**, *139*, 239–243.

(56) Gérardy-Montouillout, V.; Malveau, C.; Tekely, P.; Olender, Z.; Luz, Z. *J. Magn. Reson., Ser. A* **1996**, *123*, 7–15.

(57) Reichert, D.; Zimmermann, H.; Tekely, P.; Poupko, R.; Luz, Z. *J. Magn. Reson.* **1997**, *125*, 245–258.

(58) deAzevedo, E. R.; Hu, W.-G.; Bonagamba, T. J.; Schmidt-Rohr, K. *J. Am. Chem. Soc.* **1999**, *121*, 8411–8412.

(59) deAzevedo, E. R.; Hu, W.-G.; Bonagamba, T. J.; Schmidt-Rohr, K. *J. Chem. Phys.* **2000**, *112*, 8988–9001.

(60) Luz, Z.; Tekely, P.; Reichert, D. *Prog. Nucl. Mag. Res. Sp.* **2002**, *41*, 83–113.

(61) Reichert, D.; Pascui, O.; Bonagamba, T. J.; deAzevedo, E. R.; Schmidt, A. *Chem. Phys. Lett.* **2003**, *380*, 583–588.

(62) Buffy, J. J.; Waring, A. J.; Hong, M. *J. Am. Chem. Soc.* **2005**, *127*, 4477–4483.

(63) Traer, J. W.; Soo, K. J.; Vijayakumar, M.; Goward, G. R. *J. Phys. Chem. C* **2011**, *115*, 6064–6072.

(64) Bennett, A. E.; Rienstra, C. M.; Auger, M.; Lakshmi, K. V.; Griffin, R. G. *J. Chem. Phys.* **1995**, *103*, 6951.

(65) Mills, R. *J. Phys. Chem.* **1973**, *77*, 685–688.

(66) Wachowicz, M.; Gill, L.; White, J. L. *Macromolecules* **2008**, *42*, 553–555.

(67) Peng, X.; Jonas, J. *Biochemistry* **1992**, *31*, 6383–6390.

(68) Bloom, M.; Burnell, E. E.; Valic, M. I.; Weeks, G. *Chem. Phys. Lipids* **1975**, *14*, 107–112.

(69) Mabrey, S.; Sturtevant, J. M. *Proc. Natl. Acad. Sci. U. S. A.* **1976**, *73*, 3862–3866.

(70) Hackel, C.; Franz, C.; Achilles, A.; Saalwächter, K.; Reichert, D. *Phys. Chem. Chem. Phys.* **2009**, *11*, 7022.

(71) Saalwächter, K.; Fischbach, I. *J. Magn. Reson.* **2002**, *157*, 17–30.

(72) Zhou, Z.; Sayer, B. G.; Hughes, D. W.; Stark, R. E.; Epand, R. M. *Biophys. J.* **1999**, *76*, 387–399.

(73) Nagle, J. F.; Liu, Y.; Tristram-Nagle, S.; Epand, R. M.; Stark, R. E. *Biophys. J.* **1999**, *77*, 2062–2065.

(74) Vaz, W. L. C.; Clegg, R. M.; Hallmann, D. *Biochemistry* **1985**, *24*, 781–786.

(75) Tocanne, J.-F.; Dupou-Cézanne, L.; Lopez, A. *Prog. Lipid Res.* **1994**, *33*, 203–237.

(76) Filippov, A.; Orädd, G.; Lindblom, G. *Biophys. J.* **2003**, *84*, 3079–3086.

(77) Almeida, P. F. F.; Vaz, W. L. C.; Thompson, T. E. *Biochemistry* **1992**, *31*, 6739–6747.

(78) Greiner, A. J.; Pillman, H. A.; Worden, R. M.; Blanchard, G. J.; Ofoli, R. Y. *J. Phys. Chem. B* **2009**, *113*, 13263–13268.

(79) Dickey, A.; Faller, R. *Biophys. J.* **2008**, *95*, 2636–2646.

(80) Janosi, L.; Gorfe, A. A. *J. Chem. Theory Comput.* **2010**, *6*, 3267–3273.

(81) Filippov, A.; Orädd, G.; Lindblom, G. *Chem. Phys. Lipids* **2009**, *159*, 81–87.

(82) Marasinghe, P. A. B.; Buffy, J. J.; Schmidt-Rohr, K.; Hong, M. *J. Phys. Chem. B* **2005**, *109*, 22036–22044.

(83) Wi, S.; Kim, C. *J. Phys. Chem. B* **2008**, *112*, 11402–11414.

(84) Kim, C.; Spano, J.; Park, E.-K.; Wi, S. *Biochim. Biophys. Acta, Biomembr.* **2009**, *1788*, 1482–1496.

(85) Dvinskikh, S. .; Sitnikov, R.; Furó, I. *J. Magn. Reson.* **2000**, *142*, 102–110.

(86) Reichert, D.; Pascui, O.; Bonagamba, T. J.; Belton, P.; Schmidt, A.; deAzevedo, E. R. *J. Magn. Reson.* **2008**, *191*, 141–147.

(87) Ponder, E.; Barreto, D. *Blood* **1957**, *12*, 1016–1027.

(88) Schwoch, G.; Passow, H. *Mol. Cell. Biochem.* **1973**, *2*, 197–218.

(89) Johnson, R. M.; Taylor, G.; Meyer, D. B. *J. Cell Biol.* **1980**, *86*, 371–376.

Conclusions and Future Directions

In this thesis, pNIPAM core-shell microgels were explored as spherical supports for phospholipids. The core-shell microgels used were about a micron in size and synthesized via a two-step, temperature programmed free radical polymerization. It was shown that single lipid bilayers as well as intact liposomes could be immobilized on the microgel surface through different methods.

The deposition of a single impermeable lipid bilayer of POPC was possible on a highly tetradecyl modified microgel using simple POPC liposomes as the source of lipids, followed by freeze-thaw treatment. The basic concepts described should be broadly transferable to other hydrogel chemistries and lipid compositions. Therefore, in addition to their potential as drug delivery vehicles, Lipogels could provide a platform for the study of hybrid lipid/polymer assemblies as well as a model system for new scientific inquiries. For example, it could potentially be used as a model system for single-molecule fluorescence tracking in crowded, restricted environments. Likewise, it would be interesting to investigate protein folding, ligand–protein interactions, or both in a controlled crowded environment. In this regard, microgels possessing different polymer densities (i.e. different crowding capacities) within their matrix would need to be developed. However, another way to achieve control of the crowding capacity would be to take advantage of the VPT behaviour of the microgel, provided that the elevated temperature does not perturb the phenomena under study. Furthermore, the ability to control lipid curvature via the VPT could be enormously useful to study the structure and function of curvature sensing proteins that are implicated in various functions.[1]

With the development of the Bicellogel, the use of bicelles to coat soft polymeric matter was demonstrated, extending the established use of bicelles in coating silicon[2,3] and lipidic[4]

surfaces. Since discoidal bicelles can be made with a variety of saturated and unsaturated phospholipids, various lipid compositions can be used for bilayer coating. Furthermore, the electrostatic deposition used here could be readily replaced with hydrophobic modification or bioconjugation strategies that would produce salt-resistant binding of bicelles. Relative to conditions required for liposome fusion into a continuous lipid bilayer, bicelle fusion is induced simply and spontaneously under mild conditions. This, coupled with the disc-like structure of bicelles, opens up this method to many applications where the spherical "protective" aspect of liposomes is undesirable. An intriguing application of this method would be impart orientation control of ion channels embedded in supported membranes. By using the intrinsic charge of a bicelle embedded channel, its orientation relative to the microgel interior/exterior in the final fused lipid bilayer could be manipulated.

In regards to the VESCOgels, a small bi-functionalized PEG linker was synthesized with an amino and a cholesteryl end group (AECHO). Liposomes with 5 mol % AECHO (AECHO-LUVs) could be tethered to the unmodified acrylic acid bearing pNIPAM microgel covalently through simple carbodiimide chemistry. The immobilized AECHO-LUVs stay intact, which prevents the pre-mature release of their contents. Hence, the microgel and the adhered AECHO-LUVs endow the VECOgels with effectively two separate cargo holders with distinct leakage profiles. The simultaneous but differential release kinetics exhibited by VESCOgels would be attractive in applications where the delivery of two separate drugs in tandem was desired, for example, in combination chemotherapy.[5] Furthermore, VESCOgels could also be embedded in the 3D matrix of larger hydrogels, extending the capability of two-phase composite "plum pudding" systems[6–9] beyond dual release at controlled rates. Finally, the approach used here to fabricate

VESCOgels might be used to engineer microgel surfaces via liposome coating, imparting attributes or providing functional groups that would be difficult to achieve via polymerization.

Finally, ^{31}P CODEX was demonstrated to be capable of measuring the lateral diffusion of multiple phospholipids in LUVs in a label-free fashion. This should prove immensely useful in investigating situations wherein differences in lateral diffusion arise due to, for example, changes in lipid packing densities, or the presence of phase heterogeneities, or specific lipid–protein interactions. To explore the power of CODEX further, the study of artificial domains on LUVs could be an exciting first step. These domains can be formed by exploiting the differential thermotropic properties of a heterogeneous mixture of lipids, or by electrostatic interactions between charged vesicles and large charged macromolecules (e.g. polymers, DNA, proteins). Also, even though ^{31}P was exclusively focused on in the CODEX studies, it is certainly not restricted to that nucleus only. Other lipids and membrane embedded molecules that possess nuclei with groups that exhibit a CSA (e.g. ^{13}C) could also be studied in conjunction with the phospholipids. However, this would most likely require isotopic enrichment to record a CODEX decay in reasonable time. Lastly, since the quality of the ^{31}P CODEX data depend heavily on the size, polydispersity and the amount of the lipid sample, the development of a method to make monodisperse GUVs of ~1 μm diameter in high yield should be a worthy goal. In this regard, elegant microfluidic techniques capable of producing monodisperse GUVs could have enormous potential.[10] On the other hand, the supported bilayers discussed in this thesis also possess the dimensions and lamellarity appropriate for CODEX. One of the improvements that must be made, however, is the elimination of support introduced effects on the free diffusion of adhered lipids, that is seen in the FRAP curves of Lipogels and Bicellogels. These effects could introduce artifacts that could potentially obscure phenomena under study. Hence, supported

membranes would most likely benefit from the synthesis and incorporation of flexible “pillars” that would effectively lift the bilayers off the support. Intermediate molecular weight straight chained PEG molecules would be an excellent candidate for the development of these pillars.

6.1 References

(1) Mouritsen, O. G. *Eur. J. Lipid Sci. Technol.* **2011**, *113*, 1174–1187.

(2) Zeineldin, R.; Last, J. A.; Slade, A. L.; Ista, L. K.; Bisong, P.; O’Brien, M. J.; Brueck, S. R. J.; Sasaki, D. Y.; Lopez, G. P. *Langmuir* **2006**, *22*, 8163–8168.

(3) Morigaki, K.; Kimura, S.; Okada, K.; Kawasaki, T.; Kawasaki, K. *Langmuir* **2012**, *28*, 9649–9655.

(4) Tabaei, S. R.; Jönsson, P.; Brändén, M.; Höök, F. *J. Struct. Biol.* **2009**, *168*, 200–206.

(5) Catarina, A.; Nuno, J.; Simoes, S. In *Current Cancer Treatment - Novel Beyond Conventional Approaches*; Ozdemir, O., Ed.; InTech, 2011.

(6) Lynch, I.; Dawson, K. A. Synthesis and Characterization of an Extremely Versatile Structural Motif Called the “Plum-Pudding” Gel. *J. Phys. Chem. B* **2003**, *107*, 9629–9637.

(7) Lynch, I.; de Gregorio, P.; Dawson, K. A. Simultaneous Release of Hydrophobic and Cationic Solutes from Thin-Film “Plum-Pudding” Gels: A Multifunctional Platform for Surface Drug Delivery? *J. Phys. Chem. B* **2005**, *109*, 6257–6261.

(8) McGillicuddy, F. C.; Lynch, I.; Rochev, Y. A.; Burke, M.; Dawson, K. A.; Gallagher, W. M.; Keenan, A. K. Novel “Plum Pudding” Gels as Potential Drug-Eluting Stent Coatings: Controlled Release of Fluvastatin. *J. Biomed. Mater. Res., Part A* **2006**, *79A*, 923–933.

(9) Baumann, M. D.; Kang, C. E.; Stanwick, J. C.; Wang, Y.; Kim, H.; Lapitsky, Y.; Shoichet, M. S. An Injectable Drug Delivery Platform for Sustained Combination Therapy. *J. Controlled Release* **2009**, *138*, 205–213.

(10) Shum, H. C.; Lee, D.; Yoon, I.; Kodger, T.; Weitz, D. A. *Langmuir* **2008**, *24*, 7651–7653.

Appendix A

A.1 NMR Spectra and Analysis

NMR spectra were acquired by the methods listed in the main paper. Due to well separated tetradecylamine and NIPAM resonances, the ^{13}C NMR spectrum (Figure A-1) was used to assess AA modification. Essentially, since the AAs were modified by tetradecylamine, the mole ratio of AA to NIPAM (pre-modification) could to be compared to the mole ratio of tetradecylamine to NIPAM (post-modification) to determine the extent of modification. To determine the AA to NIPAM mole ratio, the following equation was used:

$$w = M_{NIPAM}m_{NIPAM} + M_{MBA}m_{MBA} + M_{AA}m_{AA} \qquad \text{Equation 29}$$

where w is the weight of the dry polymer determined gravimetrically, and M_x and m_x are molar mass and moles of the monomer, respectively. The contribution of the initiator to the weight of the polymer is deemed negligible. This equation could be rearranged in terms of the mole ratio of AA compared to NIPAM.

$$\frac{m_{AA}}{m_{NIPAM}} = \frac{M_{NIPAM} + M_{MBA}\left(\frac{m_{MBA}}{m_{NIPAM}}\right)}{\frac{w}{m_{AA}} - M_{AA}} \qquad \text{Equation 30}$$

m_{AA} was determined through potentiometric titration and it was assumed that all MBA added to the system was used up in the polymerization (hence, $\frac{m_{MBA}}{m_{NIPAM}} = 0.10$) . In our synthesis, $w = 0.06\ g$ and $m_{AA} = 3.64x10^{-5}\ moles$. Thus, the mole ratio of AA compared to NIPAM was determined to be 0.08.

To determine the mole ratio of tetradecylamine compared to NIPAM from the ^{13}C NMR spectrum, peak A (two NIPAM methyls and a tetradecylamine methylene) and peak 4 (nine tetradecylamine methylenes) were utilized. Both peaks were integrated and normalized to peak A. Hence, the following two equations were used:

Integral of peak A: $m_{C14} + 2\, m_{NIPAM} = 1$ Equation 31

Integral of peak 4: $9\, m_{C14} = 0.34$ Equation 32

where m_{C14} is the moles of tetradecylamine. Solving the equations yielded a mole ratio of tetradecylamine compared to NIPAM $\left(\frac{m_{C14}}{m_{NIPAM}}\right)$ of 0.079. Since, $\frac{m_{C14}}{m_{NIPAM}} \simeq \frac{m_{AA}}{m_{NIPAM}}$, it was deemed that essentially 100% of the AA were hydrophobically modified.

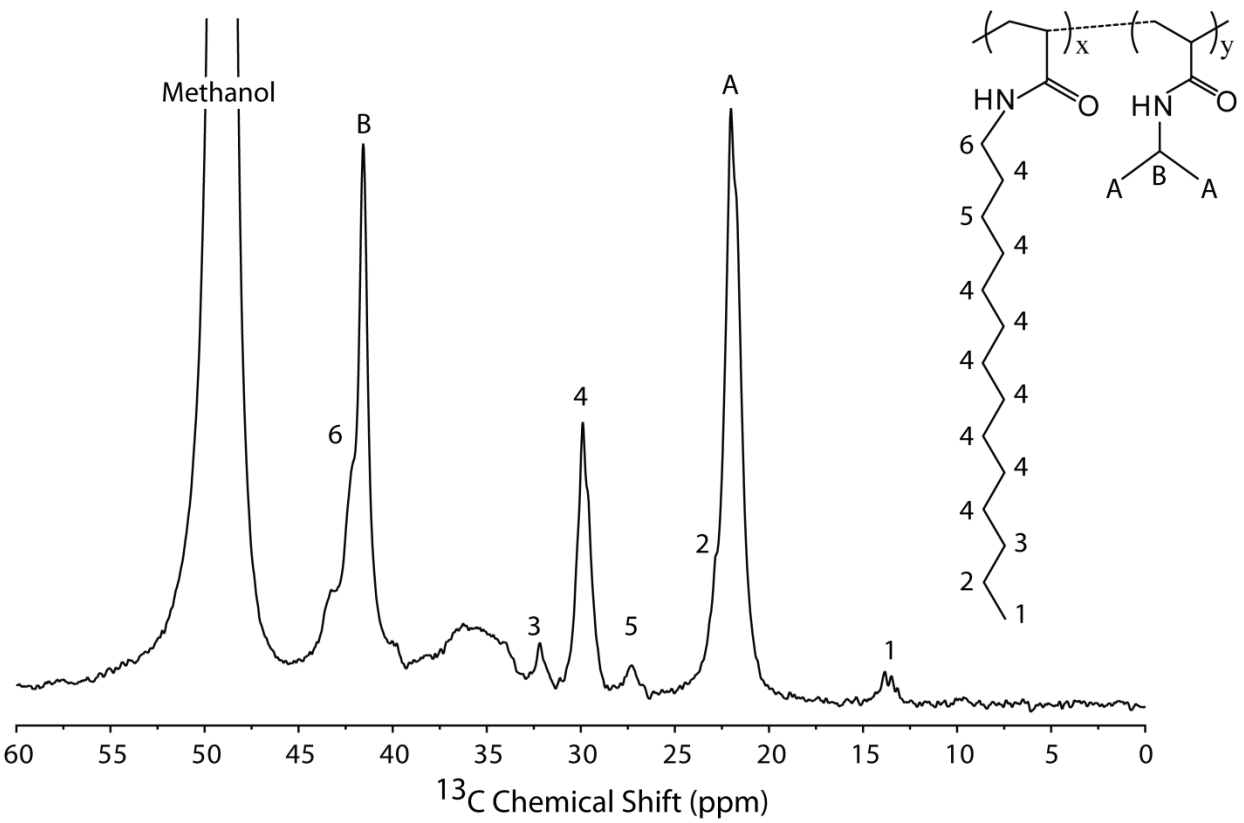

Figure A-1: ^{13}C NMR spectrum of HM microgels in methanol. Only the methyls (A) and methyne (B) from pNIPAM and the methylenes (2-6) and the methyl (1) from tetradecylamine are assigned for a relevant comparison. The two NIPAM methyls (A) and the eight hydrophobe methylenes (4) are well separated and so, their integrals could easily be taken and compared to determine the extent of hydrophobe incorporation. The only carbons missing in the spectrum are that of the carbonyls.

A.2 Fluorescence Recovery After Photobleaching (FRAP) Simulation

The FRAP of the Lipogel was simulated with a custom program written in LabView 8.2 (National instruments). The program accepts multiple input parameters describing all aspects of the Lipogel and our microscope setup. These include: Lipogel radius, number of fluorophores, diffusion coefficients, excitation wavelength, pinhole size, photobleaching position, photobleaching intensity, probing time step, observation window, imaging area size and resolution. A snapshot of the simulation program is shown in Figure A-2.

Typically, the simulations modeled a scenario in which 50,000 fluorophores were uniformly distributed on the surface of a sphere of 650 nm radius. All fluorophores were

assumed to have identical extinction coefficients and molecular brightness. The photobleaching probability depends exclusively on the excitation profile of the laser beam: 1- $c \times f(x, y, z)$, where *c* is a constant depending on the photobleaching intensity and $f(x, y, z)$ is the Gaussian approximation of the excitation profile[1]. A random number between 0 and 1 is generated for each fluorophore on the surface: if the random number is larger than the estimated photobleaching probability, the fluorophore is photobleached and will be invisible in the recovery simulations. The constant *c* was chosen to closely match the simulated image immediately after the photobleaching pulse to its experimental counterpart (Figure 2-6B).

The diffusion of the fluorophores was implemented using a Monte Carlo simulation of a 2-D random walk on the surface of the sphere. The step size of random walk was as assumed constant, $\sqrt{4D\tau}$, where *D* and τ are the user-selected diffusion constant and the sampling time step. The next position of each fluorophore was generated by selecting an arbitrary point on the circle of radius $\sqrt{4D\tau}$ around the current position on the on surface of the sphere. For each fluorophore, the contribution to the detected fluorescence signal is proportional to the apparent detection efficiency $CEF(x, y, z)$ of the objective, which depends on fluorophore position, pinhole size and beam waist[1]. Each time step, after all fluorophores move to a new position, the fluorescence signal is obtained by summing up all their $CEF(x, y, z)$ values. Finally, the FRAP curve was normalized to the estimated signal before photobleaching and it was fitted with a bi-exponential model (Equation 16) in Origin 7.0 (OriginLab Cooperation). Best fit was found when reduced chi-square converged.

At first, FRAP simulations were run assuming only one diffusing component. As shown in Figure A-3, this gives rise to a mono-exponential recovery, in stark disagreement with the biphasic behavior observed in experiments (Figure 2-6D). However, the single-component

diffusing model was used to determine the diffusion constants that closely match the two recovering times found by fitting the experimental curve (Table 2-1). These values were used to simulate the two-component diffusion model, with their fractions chosen to find the best match with the experimental FRAP curve (Figure 2-6E).

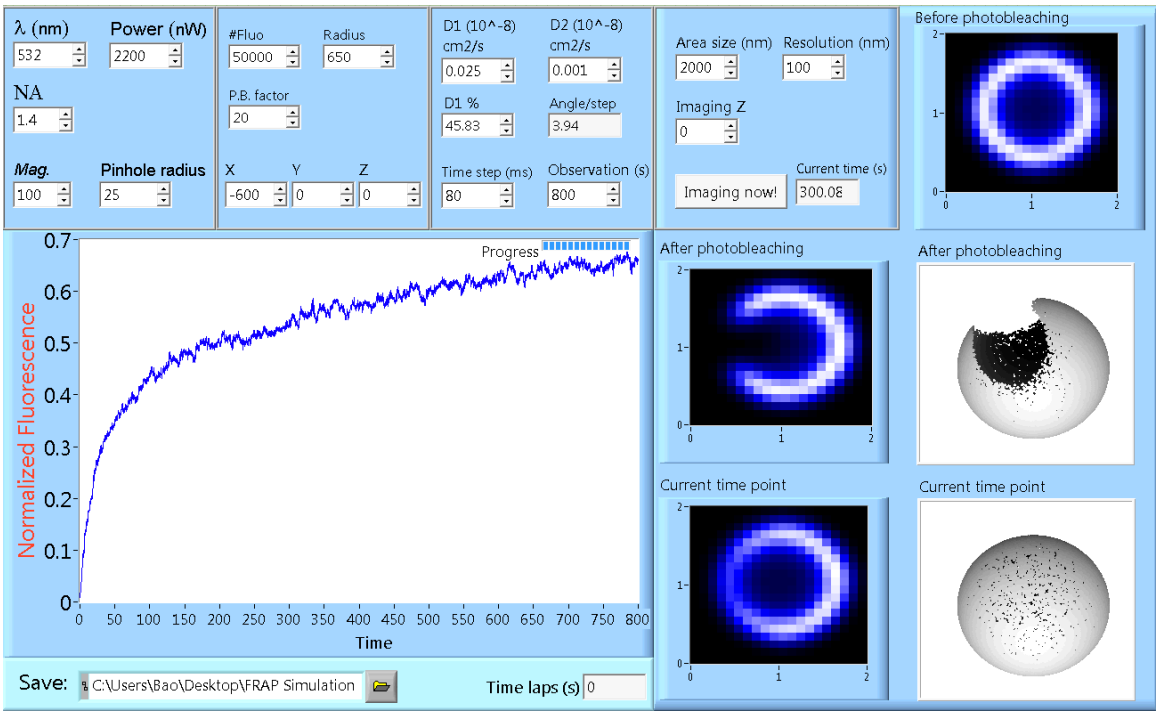

Figure A-2: FRAP simulation for a uniformly labelled sphere. The computed recovery curve is shown, together with three simulated images: before, immediately after and 5 min. after instant photobleaching. The 3D plots show the non-bleached fluorophore distribution immediately after photobleaching and after a 5 min. delay.

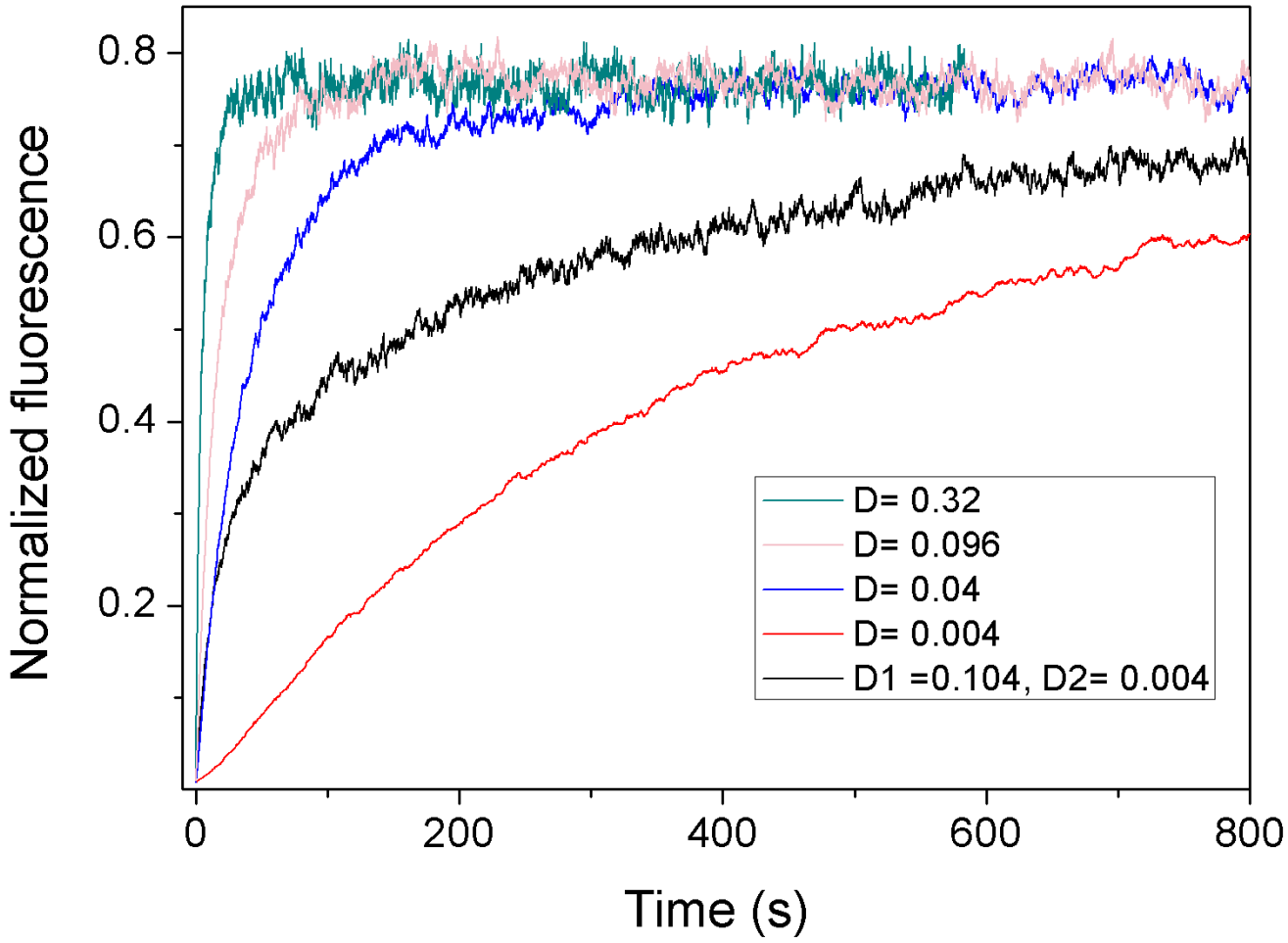

Figure A-3: Simulated FRAP curves, using one-component model (green, magenta, blue and red) and two-component model (black). The diffusion constants for each curve are given in units of 10^{-8} cm^2/s.

A.3 Reference

(1) Wohland, T. *Biophys. J.* **2001**, *80*, 2987-2999.